Broadband IF Circuits for Superconductor Isolator Superconductor (SIS) Mixers for the Heterodyne Instrument for the Far Infrared on the Herschel Space Observatory and for Sideband Separating Mixers

Inaugural-Dissertation

zur
Erlangung des Doktorgrades
der Mathematisch-Naturwissenschaftlichen Fakultät
der Universität zu Köln

vorgelegt von

Matthias Justen

aus Trier

Köln 2007

Abstract

This thesis describes the development and manufacturing of the IF circuits for two different heterodyne receivers used for sub-mm radio astronomy.

The first project is the broadband 4-8 GHz IF circuitry for the mixer units for band 2 of the Heterodyne Instrument for the Far Infrared (HIFI). This instrument will be operating onboard of ESA's Herschel space observatory. The band 2 mixer units for HIFI, built by KOSMA, implement low noise SIS mixers in a very compact, modular design. The complete IF path in the mixer units consist of the mixer block (with the SIS mixer chip) and the bias-T, which is needed to apply a bias voltage to the SIS-junction and to extract the IF signal.

The detailed investigation of the IF performance of the mixer block must consider the geometric capacitances of the SIS-junction and the tuning structure as well as the inductance of the bond wires used to establish the contact between the mixer chip and the SMA output connector. The calculations presented in this thesis show that the design can be used for IF frequencies up to 12 GHz.

The bias-T, which is implemented in the mixer unit, is a dedicated, new development with high performance and high reliability complying with the special requirements for a spaceborne instrument. These include the survival under high mechanical stress such as vibration during the launch and extensive thermal cycling to cryogenic temperatures during the tests of the mixer unit and the instrument. An excellent ($S_{21} > -0.25 \, dB$) IF signal transmission of the bias-T is achieved by special high reliability connections in the signal path. Different coefficients of thermal expansion are compensated by the mechanical flexibility of the connections. These special parts have been developed, manufactured, integrated and tested within this work in a three phase design cycle (Demonstration Model(DM) − Qualification Model (QM) − Flight Model (FM)).

In addition to the high transmission, the bias-T provides filter circuits, which effectively protect the signal path from electromagnetic interference (EMI) entering the mixer unit via the unshielded bias lines.

The mixer units have passed all performance and environmental tests and are presently integrated into the HIFI instrument.

The second project is the development and fabrication of very broadband nonuniform couplers, which can be used as -3 dB 90°-hybrids on the IF side of sideband separating mixers with large IF bandwidth.

By the smooth (e.g., nonuniform, not stepped-uniform) change of the even- and odd-mode impedances along the wave propagation direction, uncontrolled

reflections are avoided, which is indispensable to achieve a large bandwidth. Strong power coupling (-3 dB, e.g., 50%) is achieved with broadside coupled lines in a homogeneous stripline configuration, which ensures TEM mode propagation. This TEM mode propagation and the smooth distribution of the electrical parameters allow to achieve a large bandwidth. The impedances can be calculated by Fourier transformation of the power coupling bandshape.

In order to determine the actual geometry (e.g., stripline width and spacing) from even mode line impedances, a design procedure has been developed, which is presented in this thesis. It includes an appropriate mix of analytic calculations and an interpolation scheme which uses results from a commercial 2D EM-field solver. This procedure has been successfully applied in order to design various couplers, which have been manufactured and tested. By introducing mode launchers in the vicinity of the coupler ports, the TEM mode purity could be improved, which led to an increased coupler bandwidth of 1.9-9.3 GHz.

Contents

Chapter 1

Introduction

1.1   Sub-mm radio astronomy

In the past decades the interest in astronomical observations in the sub-mm wavelength range has steadily grown. This range of the electromagnetic spectrum offers a unique possibility to observe cold mater ($T < 100\,K$), e.g., the interstellar medium (ISM). The mechanisms of star and planet formation in cold gas clouds can be studied. The cooling lines from different species (for instance CO, CI and CII in photon dominated regions (PDRs)) and rotational and vibrational molecular lines (from simple hydrides to complex aromatic molecules) may be used to probe the physics and the chemistry of the gas. With the high spectral resolution of heterodyne receivers, the line profiles of emission lines and (typically narrower) absorption lines can be resolved. The line shape gives access to the kinematics (distribution of temperature, pressure and velocity (redshift) along the line of sight) of the gas. Because of the comparatively long wavelength, the radiation in the sub-mm range experiences only weak scattering by dust in the line of sight. This opens the view to regions which are hidden behind interstellar dust in the visible and near infrared part of the spectrum.

The main difficulties for observations in the sub-mm range are the non-availability of high sensitivity astronomical receivers and the high opacity of the Earth's atmosphere. Ground based observations suffer from absorption of the signal in the Earth's atmosphere mainly due to water vapor. Even at very high and dry sites like the Atacama dessert in Chile the atmospheric transmission allows radio astronomy only in some atmospheric windows. Fig. 1.1 shows the transmission at the site for a precipitable water vapor PWV=1.0 mm. The absorption leads to high system noise temperatures T_{SYS} and thus long observation times τ according to the radiometer equation: $\Delta T_{SYS} = \frac{K\,T_{SYS}}{\sqrt{\Delta f\,\tau}}$ where ΔT_{SYS} is the minimum detectable signal, Δf is the detection bandwidth, e.g., the bandwidth of one spectrometer channel and K is a factor of order unity depending on the observing mode and
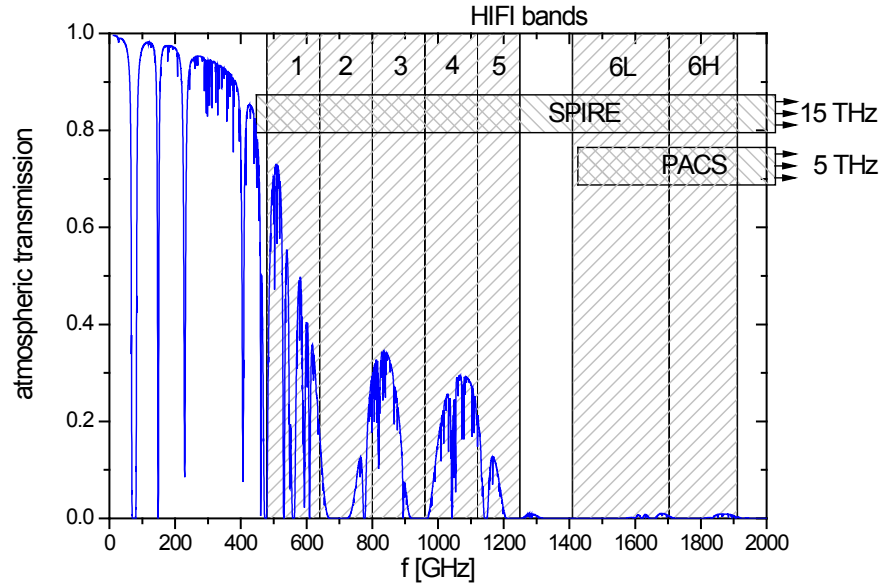
Fig. 1.1: *Atmospheric transmission at the Atacama dessert [1], Chile (altitude ≈ 5100 m) for precipitable water vapor PWV = 1.0 mm (50% quartile: PWV ≤ 1.0 mm over the year [2]). Herschel enables unbiased measurements over a large frequency range which is not accessible with ground based observations.*

the particular receiver used in the measurement. Drifts in the optical path, for example due to fluctuations in the low atmospheric transmission or due to changing temperature gradients in the telescope optics, make an exact subtraction of the background very difficult.

In order to ameliorate the observing conditions, the telescope can be placed onboard of an airplane ($h \approx 13\,km$), a balloon ($h \approx 25\,km$) or a spacecraft. The superior conditions are worth both the high technological effort and the high costs because they allow observations which are not possible from ground based observatories. The first part of this thesis concerns the KOSMA contribution to one of the mixer bands of the Heterodyne Instrument for the Far Infrared (HIFI) aboard of the Herschel space telescope. The space telescope and the heterodyne instrument are described in brief in section 1.2.

Another possibility to reduce the influence of the atmosphere is the use of sideband separating mixers. The atmospheric noise of the unused sideband can be separated (and terminated with a $4.2\,K$ load) which increases the sensitivity, the stability and the calibration accuracy of the receiver. The advantages are described in more detail in section 1.3.

Very sensitive heterodyne mixers with a broad IF bandwidth are necessary to fully exploit the advantages of both observing platforms sketched above. The most sensitive mixers in the sub-mm range are Superconductor Insulator Superconductor (SIS) mixers, which use the strongly nonlinear I(V) characteristic of an SIS contact for the mixing process. A large instantaneous IF bandwidth enables efficient line surveys. With a large IF bandwidth, it is

possible to observe extragalactic lines (e.g., *CII* at high redshift), which are very broad due to the velocity dispersion in the observed objects.

1.2   Herschel / HIFI at a glance

1.2.1   The Herschel spacecraft

dimensions:
4m x 4m x 7.5m,
3.3 tons

protective sunshade,
solar cells

local oscillator
unit

service
module

telescope mirror, d = 3.5 m,
passively cooled to 90 K,
f / 9.8 Cassegrain optics

cryostat with
scientific instruments,
2.5m^3 superfluid He
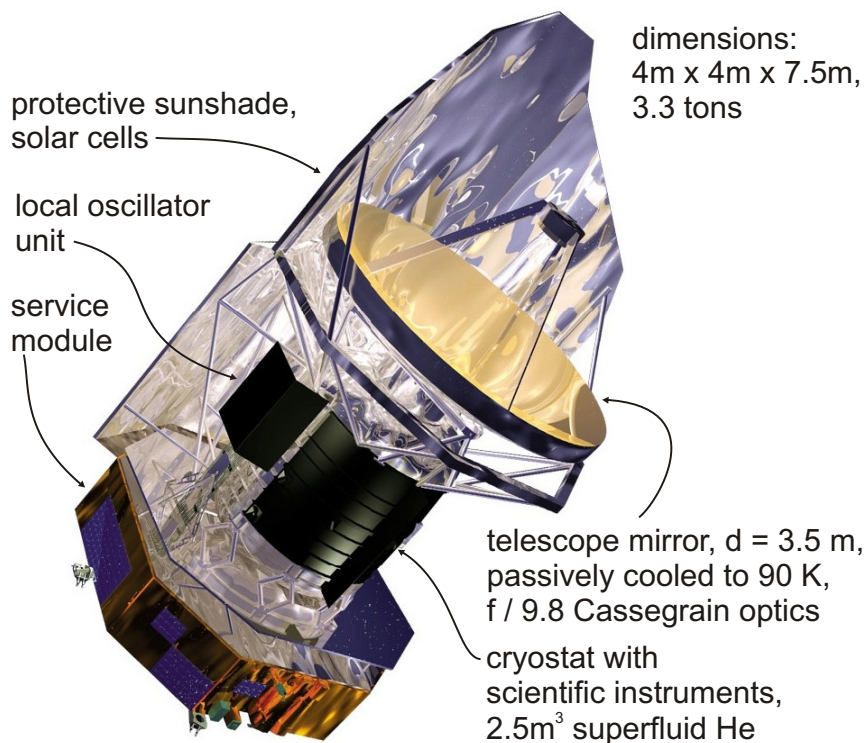
Fig. 1.2: *The Herschel space observatory.*

The Herschel space observatory [3], the fourth "cornerstone mission" of ESA is named after Sir Friedrich Wilhelm Herschel (1738-1822), who discovered infrared radiation in the sunlight. The telescope will perform imaging photometry and spectroscopy in the far infrared and sub-mm part of the spectrum, covering approximately the $60 - 670\,\mu m$ range. It will carry a $d = 3.5\,m$ primary mirror radiatively cooled to $90\,K$ as part of the f/9.8 Cassegrain optics (see Fig. 1.2). During its stay in a large Lissajous orbit about the second Lagrange point (L2) of the Earth-Sun system, it will provide a minimum of 3 years routine observation time (limited by the boil-off of $2.5\,m^3$ superfluid He).

By placing the telescope outside the atmosphere, the whole sub-mm frequency range is accessible and a low and very stable background can be achieved. This is especially important for observations of very remote objects, e.g., *CII* emission at very high redshift. From the remote position in L2 the disturbing

black body radiation of Sun and Earth are seen in the same angular position, which maximizes the observable field on the sky. With protection from sunlight by a sunshade, the whole telescope optics can be cooled to 90 K, which is especially important for the bolometer instruments of Herschel. This optimum conditions for observations in the far infrared range are worth the large technological effort and the high costs for a spaceborne telescope.

1.2.2   Scientific instruments for Herschel

The Herschel observatory features three scientific instruments:

PACS (Photodetector Array Camera and Spectrometer) [4] employs two filled Si bolometer arrays with 32×64 pixels for $\lambda = 60 - 90 \, \mu m$ or $\lambda = 90 - 130 \, \mu m$ and 16×32 pixels for $\lambda = 130 - 210 \, \mu m$. Furthermore, two 25×16 photoconductor arrays with stressed Ge:Ga allow integral-field line spectroscopy over $\lambda = 57 - 210 \, \mu m$ with low to medium resolution ($\approx 175 \, km/s$).

SPIRE (Spectral and Photometric Imaging REceiver) [5] comprises an imaging spectrometer and an Fourier transform spectrometer (FTS). Both spectrometers use a total of five 'spider-web' NTD (neutron transmutation doped) Ge bolometers with feed horns and JFET readout electronics for each pixel.

HIFI (Heterodyne Instrument for the Far Infrared) [6] is a single pixel spectrometer with very high spectral resolution ($0.03 - 300 \, km/s$).

1.2.3   HIFI - the Heterodyne Instrument for Far Infrared

While SPIRE and PACS are best suited for large surveys with low frequency resolution, HIFI is able to resolve spectral lines with very high resolution. This makes it possible to investigate a large number of astronomical key questions including the following [6], [7]:

- HIFI will probe the physics, kinematics and energetics of star forming regions through their cooling lines, including H_2O, the major coolant.

- HIFI will survey the molecular inventory of such diverse regions as shocked molecular clouds, dense Photon Dominated Regions (PDRs), diffuse atomic clouds, Hot Cores and proto-planetary disks around newly formed stars, winds from dying stars and toroids interacting with Active Galactic Nucleus (AGN) engines.

- HIFI is particularly suited to search for low-lying rovibrational transitions of complex species such as Polycyclic Aromatic Hydrocarbons (PAHs) and, thus, to investigate the origin and evolution of the molecular universe.
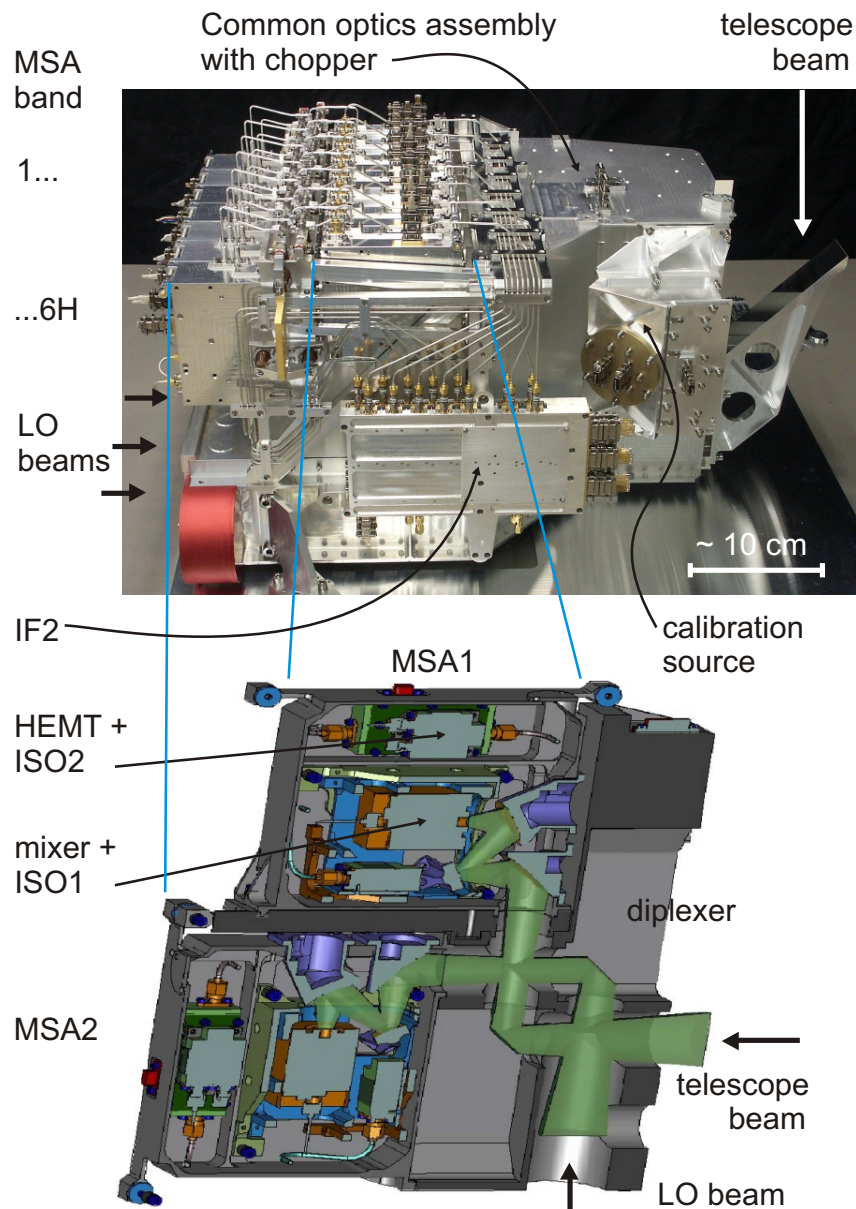
Fig. 1.3: *Above: The focal plane unit (FPU) of the HIFI instrument. The FPU is situated in the Herschel cryostat and fed with the telescope beam and the LO beams from both sides through windows in the cryostat. The complete FPU contains a total of seven RF bands with two mixer subassemblies (MSA) per band.*
Below: The configuration of the two MSAs for vertical and horizontal polarization. Each MSA contains a mixer unit, two isolators and an HEMT amplifier. The optical path of the signal and the LO radiation (green) is combined by a diplexer.

- HIFI can provide the out-gassing rate of comets through H_2O rotational lines and determine the vertical distribution of H_2O in the giant planets.

- HIFI can measure the mass-loss history of stars, which, rather than

nuclear burning, regulates stellar evolution after the main sequence and dominates the gas and dust mass balance of the interstellar medium (ISM).

- HIFI will measure the pressure of the interstellar gas throughout the Milky Way and will resolve the problem of the origin of the intense galactic CII 158 μm emission measured by COBE (Cosmic Background Explorer satellite).

- HIFI can determine the $^{12}C/^{13}C$ and $^{14}N/^{15}N$ isotope ratios as a function of galactic radius in the Milky Way and other galaxies through the hyperfine splitting of atomic fine-structure lines. One can thus constrain the parameters of the Big Bang and explore the nuclear processes that enrich the ISM.

- HIFI will measure the far infrared line spectrum of nearby galaxies as templates for distant, possibly primordial, galaxies.

All these studies require a very high spectral resolution combined with a very broad instantaneous bandwidth in order to resolve the kinematics hidden in the line profiles. Thus, HIFI covers a wide range of 480-1250 GHz and 1400-1910 GHz with a maximum resolution of $\frac{f}{\Delta f} = 3.6\ 10^6 \ldots 1.4\ 10^7$ (corresponding to the minimum channel width of the high resolution spectrometer, $\Delta f = 134\,kHz$).

The very high sensitivity of the mixers ($\approx 5\,hf/k_B$) and a large instantaneous bandwidth of 4-8 GHz, which is achieved for the first time for a heterodyne receiver, allow fast spectral surveys. Lines from extragalactic objects are broadened due to the velocity dispersion in these objects of up to 1000 km/s [8]. With HIFI, it is possible to measure these lines in a single LO frequency setting (e.g., band 2 instantaneous bandwidth: $1.5 - 1.9\ 10^3\,km/s$).

The mixer units for HIFI band 2 have been developed at KOSMA [9], [10], [11]. A total of four PhD projects discuss different topics of the design, the development and the manufacturing of the units: The RF design of the waveguide probe and the RF blocking filters is described in [12], the analysis of the heterodyne measurements and the RF tuning structure design is described in [13] and the fabrication of the SIS-mixer devices in the KOSMA clean room facility is published in [14]. This work contributes to the HIFI instrument with the design and investigation of the 4-8 GHz IF circuits for the mixer units of band 2. It describes the development of a bias-T with extremely low loss over the whole IF range, which is necessary for a good noise performance of the mixer unit. In addition, the bias-T provides outstanding EMI rejection capabilities, which are required to protect the IF signal chain from noise of other satellite instruments.

1.3 -3 dB 90°-hybrids for the IF part of sideband separating mixer units for a 345 GHz array

The second part of this work, although completely independent of the HIFI project, also presents a part of the IF chain of a sideband separating mixer. This type of mixer is well suited for ground based operation because it is capable to separate the atmospheric noise contribution of the unused sideband. Among other advantages (better calibration, unambiguous frequency relation) this can significantly reduce observing time. Even with the excellent atmospheric transmission in the center of the 345 GHz window, as shown in Fig. 1.1, the observing time is 40% less than with a double sideband receiver ($\tau_{SSB} = 0.59\,\tau_{DSB}$) [15]. In order to really achieve this performance, a good sideband separation ratio is needed over a large IF bandwidth. The nonuniform directional couplers presented in chapter 6 can be used as -3 dB 90°-hybrids in sideband separating mixers and provide both an excellent sideband separation and a very large bandwidth.

1.4 Thesis overview

This thesis is divided into two independent parts. The first part (chapter 2 to chapter 5) describes the development, the characterization and the manufacturing of the IF circuits for the mixer units of band 2 for the HIFI instrument.

Chapter 2 begins with a short general description of the mixer unit including the mechanical design and the spatial component allocation within the tight envelope constraints. The performance specifications and the environmental conditions (especially thermal cycling and vibration), which heavily influence the mechanical and electrical design, are summarized in order to point out their importance for the mixer unit design. The chapter continues with the investigation of the IF path in the mixer block. Within this thesis, the influence of the SIS junction area, the RF tuning structure and the bond wires on the IF performance is evaluated with a combination of several software tools, which allow the evaluation of single sections of the signal path on one hand and the appropriate combination of these results on the other hand. The last part of the chapter delves into the design of the 4-8 GHz bias-T and the ESD/EMI filter circuit which both are developed by the author. This includes different specialized interconnecting components (the SMA jack and the SMA cable assembly) which have been developed to achieve high reliability while maximizing performance and minimizing space and weight of the mixer unit.

Chapter 3 describes the procedures for the space qualified, highly repeatable manufacturing of these components and their integration into the bias-T

housing. These procedures have been developed as a part of this thesis because the manufacturing and assembly have for the largest part been accomplished by the manual work of the author.

In chapter 4 the IF performance of the mixer unit is evaluated using different measurement methods. S-parameter measurements and measurements with the variable temperature method showed the very high signal transmission of the bias-T at room temperature and at cryogenic temperatures. With the SIS junction as shot noise source and with heterodyne measurements, the IF performance of the whole mixer unit (including mixer chip) can be characterized. These measurements revealed a flat band over the whole 4-8 GHz IF range. The last part of the chapter presents the electromagnetic interference (EMI) rejection capabilities of the mixers, which have been measured at the test facility of the NLR.

Chapter 5 discusses the environmental conditions for the mixer unit during shipment, handling (e.g., integration into the FPU), testing and launch. Vibration tests performed by the author in cooperation with M. Schultz on the KOSMA vibration test facility and the resulting changes in the mixer design are described.

The qualification test program for the mixer units includes intensive thermal cycling to cryogenic temperatures. The chapter summarizes all special electrical and mechanical connections, which are designed with matched coefficients of thermal expansion or special flexibility in order to achieve high reliability under these conditions.

A special environmental condition is the long and intensive exposure of the spacecraft to solar protons during the observation phase. The SIS mixer chips have been tested for radiation hardness by an experiment carried out by R. Bieber and the author at the AGOR synchrotron at the KVI facility in Groningen, NL. The radiation environment of the satellite and the radiation tests are described in the last part of chapter 5.

The second part of this thesis (chapter 6) is dedicated to the development and fabrication of very broadband nonuniform couplers used as -3 dB 90°-hybrids in sideband separating mixers. The first part of this chapter gives a short description of possible applications of these couplers in sideband separating mixers and balanced amplifiers with special attention to the performance criteria for the couplers in this applications.

The next part of the chapter describes the theory of nonuniform coupled lines, which allows to calculate the impedance distribution along the lines. From this impedance distribution the actual geometry of the coupler is calculated with a special interpolation scheme developed within this thesis, which uses even- and odd-mode impedance results from a commercially available 2D field solver. Based on the results of the calculations a coupler

has been designed and fabricated with similar techniques already used for the fabrication of the HIFI bias-T circuits. The coupler bandwidth could be increased in two design cycles to very high values in very good correspondence with the design calculations.

Acronyms are usually explained when they first appear in the text. For reference all acronyms are explained again in the table in 6.7.3.

Chapter 2

Broadband 4–8 GHz IF design for the mixer units for HIFI band 2

2.1 The mixer units for HIFI band 2

Fig. 2.1 shows a picture of a completely assembled mixer unit (MU) for HIFI band 2, which was designed, fabricated and characterized at the KOSMA facility. The MU has to fit into a small envelope of $32 \times 32 \times 45 \, mm^3$ with a central optical axis defined by the precisely orientated corrugated feed horn. The mechanical interface with the mixer subassembly (MSA) is defined by a footprint consisting of three small mounting planes with M2 screw holes guarantying stability and good thermal contact. The optical axis is aligned to the MSA and the optics of the focal plane unit (FPU) by additional reference planes in the front plane and the foremost part of the lateral plane. (See also the exploded drawing in Fig. 2.2.) The two MDM (Mini Sub-D) connectors for biasing the SIS junction on one hand, and for magnet- and deflux heater-supply on the other hand, have to be arranged together with the SMA connector for the IF signal in the rear plane of the MU. With the horn and thus the mixer block in the central axis and with the magnet and its pole pieces as close as possible to the SIS junction, there is not much space left in the tight envelope, which can be used for the bias circuits. The L-shaped configuration of the bias-T box and the box for ESD (electro static discharge) protection filters optimally uses the remaining space, while giving additional stiffness to the mixer unit.

The bias-T box is connected to the mixer block by a semi rigid SMA cable. This allows easy assembly with the mixer block by means of the SMA connector and gives enough mechanical flexibility between the (Cu) mixer block and the (Al) housing of the bias-T box to compensate for thermal contraction at cryogenic temperatures.

Beside meeting all external constraints (envelope, central optical axis, rear plane connectors), this modular design gives high flexibility in exchanging
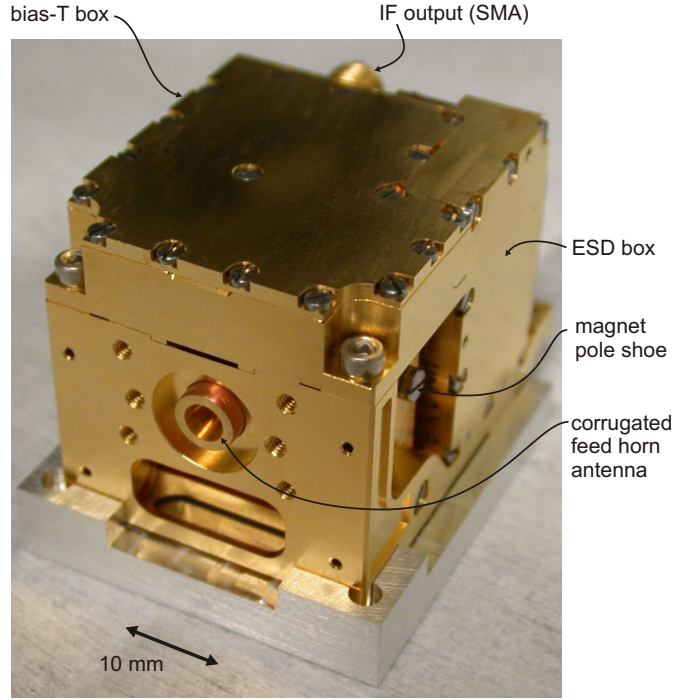
Fig. 2.1: *Completely assembled Quality Model (2ⁿᵈ design iteration) of a mixer unit for HIFI band 2 (636-802 GHz). Dimensions: $32 \times 32 \times 45\ mm^3$*

components and facilitates separate testing of the RF and the IF/DC part of the mixer. In this way, a lot of time could be saved during the development and the extensive test phases.

2.2 Performance specifications for the IF and bias circuits

Very important for the noise temperature of the mixer is a very low signal attenuation (FM: $S_{21} \geq -0.25\ dB$ over 4-8 GHz) before the first amplifier. Much attention has been given to the development of signal path transitions with low reflection coefficients and a good bias voltage injection, in order to avoid standing waves in the IF path.

Besides fulfilling the IF performance requirements, the mixer unit must be equipped with ESD (electrostatic discharge) and EMI (electromagnetic interference) protection, which makes it suitable to operate in the special satellite environment [16]:

A 5-wire bias scheme allows to shunt the junction by a protective, low resistance (47 Ω), while measuring separately bias current and bias voltage of the SIS junction. Further protection against ESD must be provided to protect the junction during the integration of the MU in the FPU. The IF chain
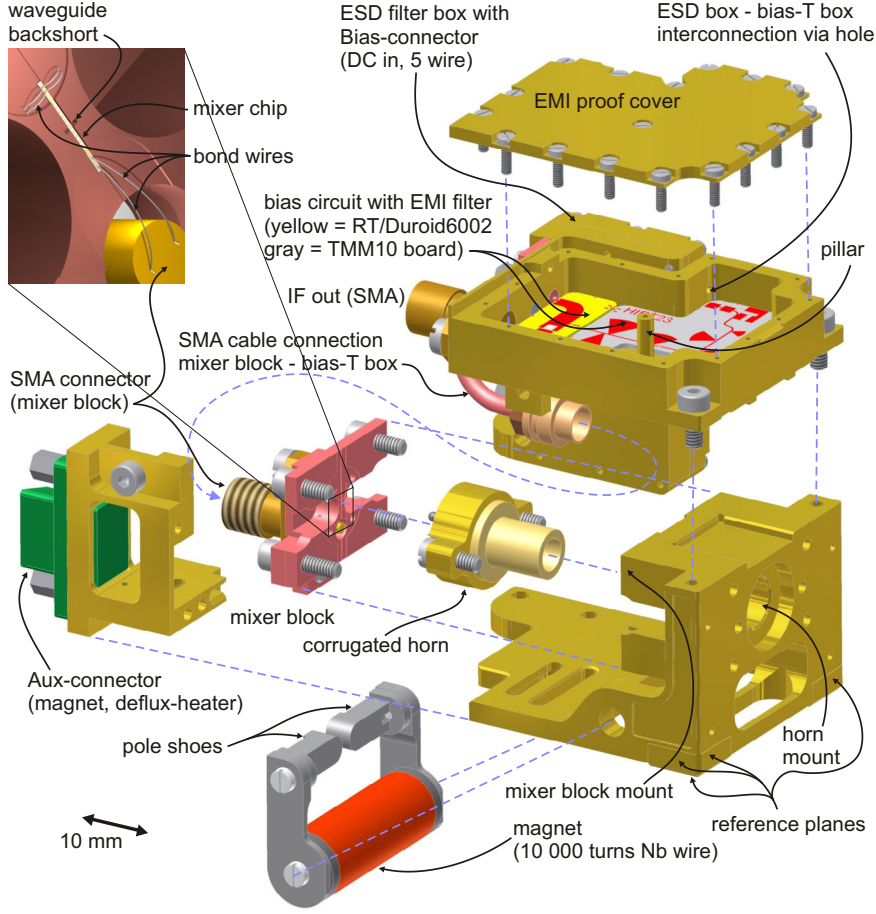
Fig. 2.2: *Explosion drawing of all mixer unit components. The modular design enables fast design iterations and high flexibility in testing and exchanging components.*

must resist EMI, which can enter the circuit via the unshielded bias lines in the cryostat. The EMI levels at the junction must be as low as -155 dBm in the IF band (4–8 GHz) and -93 dBm out of band in order to provide an unperturbed IF output signal [17], [16]. Within the development, it became clear that this high shielding levels can best be achieved with two separate compartments for low frequency (ESD box) and high frequency (bias-T box) filters because such a separation lowers the radiative transmission of EMI within the circuit.

The mixer units have a very low thermal budget because they are operated at the 2.5 K stage of the HIFI cryostat. Due to these restrictions, a tradeoff between good ESD protection with high resistor values and power dissipation (preferably low values for all current carrying resistors) has to be made.

2.3   Test- and space-environment conditions

The large temperature differences between room temperature, operational temperature ($\approx 2.5\,K$) and bakeout temperature ($80°C$) require a careful material choice and a special design at the material interfaces and interconnections. Shipment, integration into the FPU and especially the launch may result in high shock and vibration levels. In the design of the bias-T, these were taken into account in order to assure the survival of the mixers during the mission. Intensive qualification testing (see chapter 5) has proven the stability of the mixer units under these rough environmental conditions.

The IF and bias circuit design maximizes performance (transmission (S_{21}), ESD and EMI protection), while providing the reliability which is necessary for a spaceborne instrument.

2.4   The 4-8 GHz IF chain in the mixer unit

Fig. 2.3 shows an overview of the IF chain of the mixer unit. It consists of three building blocks, the mixer block, the bias-T and the ESD filter, which are also geometrically separated in different boxes.
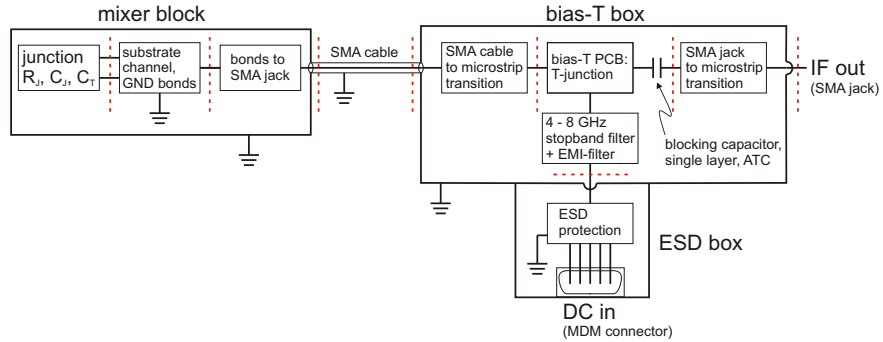
Fig. 2.3: *IF chain of the mixer unit from the SIS-junction to the SMA output connector. Three building blocks are separated in different enclosures: mixer block, bias-T box, ESD box. The red dashed lines indicate reference planes where the circuit can be decomposed in small units for separate investigation.*

The mixer block design is a weight-optimized design of a regular KOSMA mixer block with an SMA connector as IF output port. Within this thesis, the design was investigated for the 4-8 GHz IF band of the HIFI instrument. A tolerance analysis of the influence on the performance of the dimensions of the wedge bonds contacting the mixer chip to ground and to the IF output connector is presented in section 2.6.

The bias-T box and the ESD filter box are a dedicated development for the HIFI mixer units. The complete development, the verification and large parts

of the hardware manufacturing process have all been carried out by the author. A typical development cycle consists of a design verification and optimization phase strongly supported by software (sections 2.5, 2.7), the realization in hardware (with feasibility analysis) (chapter 3) and performance measurements (chapter 4.1) accompanied with environmental tests (chapter 5). Several development cycles resulted in the Demonstration Model (DM), the Qualification Model (QM), with an extensive qualification test program and the final Flight Model (FM).

In order to increase the development speed, it was often necessary to cut corners and to take two stairs at once. Nevertheless, the DM-QM-FM approach proved to be a reasonable schedule to streamline development and to reach design convergence. The systematic description presented here, results from a review of the development for this thesis.

2.5 Software for microwave circuit simulation

In the past years software for the simulation of microwave circuits rapidly evolved to very helpful tools for circuit design and optimization. In the software models, it is easy to change circuit parameters. Efficient code and the constantly growing speed of the computer hardware make it possible to simulate complex circuits in a reasonable time. The software is able to provide important data which is very difficult to measure (e.g., the E-field distribution inside a structure is always disturbed by the probe, which is used to measure the field distribution). These advantages result in a highly increased development speed. For this work, software tools have been extensively used in order to characterize and optimize all IF-components of the HIFI mixer units for band 2.

First calculations for the bias-T Demonstration Model have been carried out with the program "hp Microwave Academy", which evaluates closed form expressions for several standard microstrip structures. Unfortunately, this program is not supported any more and for further development it was necessary to change to the program "Microwave Office" (MWO) from the company "Applied Wave Research" (AWR). This program works similarly to "Microwave Academy" and has better layout export functions.

For further investigation of non-standard components, such as transitions from coaxial to microstrip lines, for control and comparison of simulation predictions, it was very helpful to use a 3D time domain simulation program "Microwave Studio" (MWS) from "Computer Simulation Technologies" (CST).

The models in both programs evolved during the development phase and the adequate combination of both programs resulted in accurate simulation results, circumventing the weak points (such as insufficient accuracy (MWO), low speed (CST),...) of the software.

2.5.1   Closed form models in AWR Microwave Office

The linear simulator in MWO uses the nodal admittance matrix method [18]. For every node of the circuit, the corresponding Kirchhoff current-law equations are formulated with the branch elements represented by their complex admittance values. This system of linear equations is then solved for currents and voltages at every branch and node respectively. This is done for every desired frequency value separately. From there, S-parameters, port input impedances and other values can be derived [19]. The admittance values of the elements are derived from closed form expressions, which describe the element within a certain interval for each model parameter.

In the high frequency stop-band filter in the bias-T, six radial stubs are used in shunt configuration because they provide a very low impedance at a highly localized ($w_S = 0.2\,mm$) foot point, which results in a very broadband RF short at the foot point location. Unfortunately, the shunted radial stub model "MSRSTUB" in MWO, taken from [20] and [21], has a bad accuracy. A better model, "MSRSTUB2", (from [22]) only became available with a newer version of MWO, when the design process of the bias-T was already finished. The investigation of a radial stub in series configuration together with a T-junction resulted in an even worse accuracy. This is because the capacitive coupling of the stub with the line is neglected in this model.
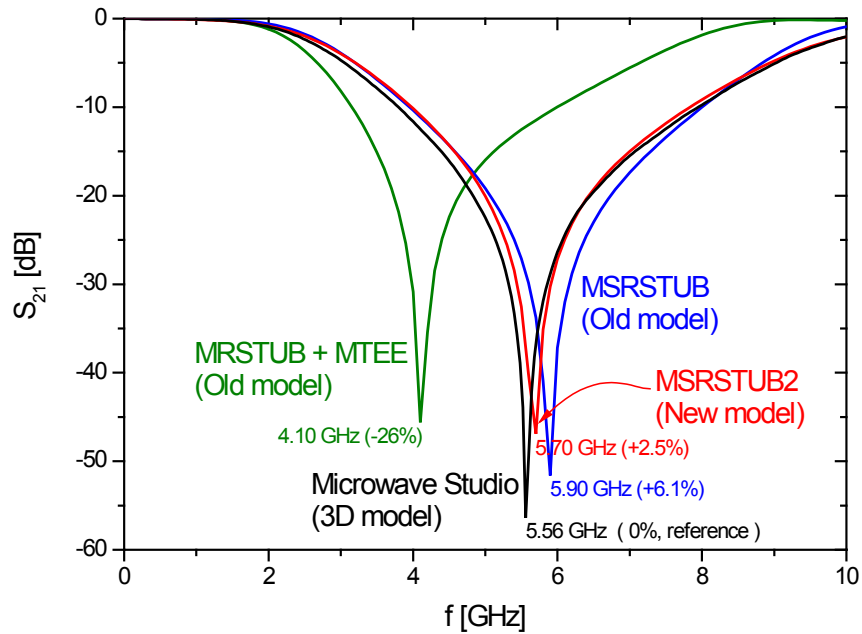
Fig. 2.4: *S-parameters of three different closed form models in AWR MWO in comparison with results from a 3D model shown in Fig. 2.5. The accuracy of the MRSTUB+MTEE and the MSRSTUB models are not sufficient for a straight forward design procedure. Thus, several design cycles have been necessary for the development of the filter section.*

Fig. 2.4 summarizes the different models and their accuracy in comparison

with a time domain simulation of the shunted radial stub model in CST MWS. The values are calculated for the geometry of the second radial stub in the bias-T ($r = 4.2\,mm$, $\theta = 60°$) on a TMM10 substrate with $\varepsilon_r = 9.2$, $h = 0.635\,mm$. The model and a drawing are shown in Fig. 2.5. These results show clearly that the electrical length of the stub is underestimated in the closed form models. This makes an exact design impossible because not only the central notch frequency is shifted, but also the inter-stub resonances, which have to be considered in a broadband design, are calculated inaccurately.
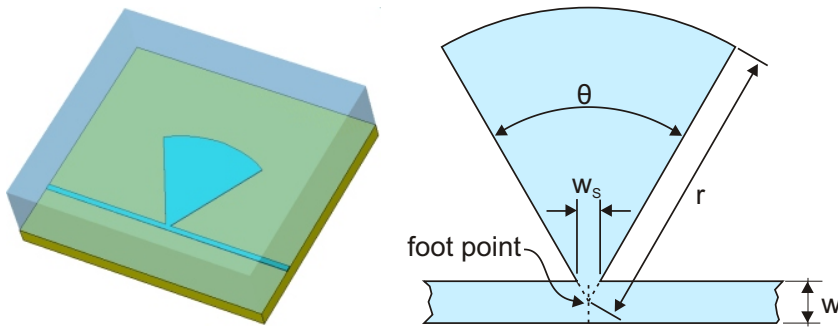
Fig. 2.5: *Left: CST MWS 3D model of a radial stub in shunt configuration. The model is used for the calculation of the transmission (S_{21}) shown in Fig. 2.4.*
Right: Design parameters of the radial stub.

Consequently an iterative design solution consisting in a closed form model in MWO and a subsequent simulation in MWS and a parallel measurement of a real world model had been used. The MWO model has been modified according to the MWS simulation data and network analyzer data until the passband from 4-8 GHz was cleared from any resonant notches resulting from inter-stub resonances. In the end of every design cycle, the circuit was fabricated on a CNC machine, mounted in a box and checked by measurements for performance and any deviations from the simulation results.

2.5.2   3D time domain simulation in CST Microwave Studio

The calculation in the time domain has the advantage of low memory requirements and a short calculation time compared to solutions in the frequency domain. Furthermore, the Fourier transform of the evolution of the signals in time domain directly results in S-parameters over a whole frequency band. This makes the time domain solver of MWS suitable for the investigation and development of the HIFI bias-T.

Model generation

In MWS the model is generated by means of a very accurate and flexible modeler. The structure is build up with bricks, cylinders and other basic geometric bodies, which can be combined with boolean operations (adding, subtracting, intersecting,...) and modified with translations, rotations, scaling and other transformations. More complex structures can be designed in an external CAD program and then imported into the modeler. For example, the metallization of the PC boards of the bias-T with different microstrip lines, curved lines and radial stubs, was designed in MWO, exported into a dxf-file and then integrated into the MWS model. The disadvantage of this way is that the imported pattern can not be parameterized as easy as the structure build up with basic elements.

Mesh generation

The intelligent mesh generator of Microwave Studio creates a cuboidal mesh orthogonal to the global coordinate system of the modeler. The mesh is composed along straight edges, end faces, ellipse bounds and other suitable fixpoints. The user can control the general mesh density by choosing the number of lines per wavelength (for example $10 \ldots 50 \, \text{lines}/\lambda(f_{MAX}, \varepsilon_r)$) and the smallest mesh step. In addition, it is possible to define the mesh density for every single element separately, which can be used to refine critical areas.

The time domain solver

Within the model space, the Maxwell equations are applied to calculate the field distribution. The Finite Integration Technique (FIT), developed by Weiland in 1977 [23], [24], provides a discrete reformulation of Maxwell's equations in their integral form. The FIT is based on a spatial segmentation of the computational domain by a doublet of two computational grids, the primary grid G (in MWS called "mesh") and the dual grid $\tilde{G}$. The electric and magnetic field vectors are integrated over the small edges and faces of the grids G and $\tilde{G}$ respectively. The resulting, so called Maxwell Grid Equations (MGE), can be written in a simple matrix form. They are exact representations of the Maxwell equations with the computational domain bounded to the (possibly arbitrarily shaped) grids. In the Maxwell Grid Equations, energy- and charge-conservation are maintained, which makes them suitable for numerically stable calculations. In Microwave Studio, the spatial representation by means of the FIT is combined with the explicit Finite Difference Time Domain (explicit FDTD) leapfrog time stepping scheme, which preserves these conservation laws [25]. The maximum stable time step is calculated prior to each simulation run. It can be estimated by the Courant criterion [26]

and depends on the dimensions of the smallest grid cell. In the case of a rectangular grid this yields in:

$$\Delta t \leq \frac{1}{c\sqrt{\frac{1}{\Delta x^2} + \frac{1}{\Delta y^2} + \frac{1}{\Delta z^2}}} \tag{2.1}$$

The material constants and the Perfect Boundary Approximation (PBA)

The material properties (permittivity, permeability, conductivity) relate the fields and currents in each grid cell to each other. Resolving curved or very thin conducting surfaces would require a grid with very small mesh cells, which would result in a high simulation time because of 2.1. Therefore, in MWS a proprietary material averaging technique referred to as perfect boundary approximation (PBA) [27] is used, which allows partially filled grid cells. This makes it possible to chose a much lower grid density and thus larger time steps, which drastically improves the calculation time.

Ports and signal excitation

CST Microwave Studio provides two ways to supply an excitation signal (for example a Gaussian shaped energy pulse) to the structure. After being scattered and absorbed in the structure, the remaining energy can also leave the structure via these so called ports.

The first possibility is a waveguide port, which is defined by a surface at the structure boundary (e.g., an end face of a coaxial waveguide). In order to assure a reflection-less energy injection, the stimulation field pattern has to be equal to an eigenmode of the port geometry. The modes are calculated with a 2D field solver from the cross section of the port (in dependence of frequency) and the user can choose which mode should be used for stimulation. (Compare also chapter 6.3.)

The second possibility is a discrete port. This is a power source with an internal impedance, which can be defined by the user (e.g., $Z = 50\,\Omega$). This source (and sink) can be connected between two arbitrary points in the structure (for example between a conductor ending and the ground plane).

For this work, the ports were fed with a Gaussian power pulse shape. This special pulse shape has the advantage that it is rather compact in the time domain resulting in a short excitation phase, which reduces simulation time. The frequency spectrum of a Gaussian pulse has likewise Gaussian shape and hence is nonzero over the whole frequency range of interest. This allows the calculation of the S-parameters over the entire frequency range by Fourier transformation of the input and output port signals. Fig. 2.6 illustrates the calculation of the S-parameters.
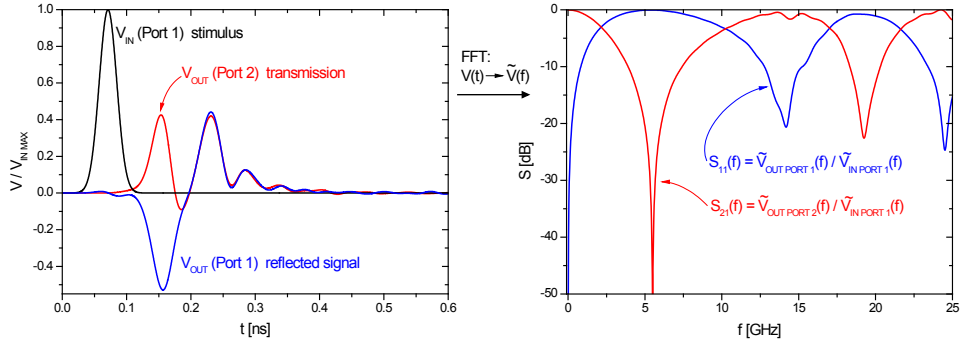
Fig. 2.6: *Calculation of the frequency domain S-parameters by Fourier transformation of the time domain signals. The 3D solver of CST MWS evaluates the propagation of a power signal with Gaussian shape through the model and calculates the reflected and transmitted signals. The signals are taken from the radial stub model shown in Fig. 2.5.*

2.5.3 Deembedding structures through S-parameter renormalization

The IF signal is guided from the SIS-junction to the IF output connector of the MU (compare Fig. 2.3). The signal path consists of several uniform transmission lines (coaxial and microstrip) and transitions in between, which should transform the field modes of the different sections into each other with maximum power transmission (matching).

Each transition section has been investigated separately by means of 3D simulations in CST MWS in order to characterize and optimize the structure and to determine worst case tolerances. The time domain solver calculates S-parameters, which are normalized to the port impedances corresponding to the eigenmode pattern of the ports. (See also chapter 6.3.) Thus, the port impedance depends on the local geometry of the cross section of the transmission line at the port location. In general, this impedance is different from the actual terminating impedance. This means that the S-parameters from the MWS calculations have to be renormalized to the actual terminating impedance in order to characterize the transmission quality of the transition. The renormalization can be done by the following transformation rule, first published in [28]:

$$\mathbf{S}_{new} = \mathbf{A}^{-1} \cdot (\mathbf{S}_{old} - \mathbf{R}) \cdot (\mathbf{I} - \mathbf{R} \cdot \mathbf{S}_{old})^{-1} \cdot \mathbf{A} \qquad (2.2)$$

with

$$
\begin{aligned}
Z_{n,old} &= \text{Old reference impedance of port } n \\
Z_{n,new} &= \text{New reference impedance of port } n
\end{aligned}
$$

$$r_n = \frac{Z_{n,new} - Z_{n,old}}{Z_{n,new} + Z_{n,old}}$$

$$\mathbf{R} = \begin{pmatrix} r_1 & 0 & \ldots & 0 \\ 0 & r_2 & \ldots & 0 \\ \vdots & \vdots & \ddots & \vdots \\ 0 & 0 & \ldots & r_N \end{pmatrix} \quad \text{(reflection coefficient matrix)}$$

$$a_n = \sqrt{\frac{Z_{n,new}}{Z_{n,old}}} \frac{1}{Z_{n,new} + Z_{n,old}}$$

$$\mathbf{A} = \begin{pmatrix} a_1 & 0 & \ldots & 0 \\ 0 & a_2 & \ldots & 0 \\ \vdots & \vdots & \ddots & \vdots \\ 0 & 0 & \ldots & a_N \end{pmatrix}$$

$$\mathbf{I} = \text{Identity matrix}$$

In section 2.6.1 S-parameters of a bond wire connection in the mixer block are quoted as an example to illustrate the effect of the renormalization (Fig. 2.9 (model) and Fig. 2.10 (S-parameters)).

2.6 IF path in the mixer block

Fig. 2.7 shows a look through the microscope to the mixer block. The SIS-junction (not resolved), situated on the microstrip waveguide probe on the quartz substrate, is the IF signal source. The substrate is glued into the substrate channel, which is covered by the horn flange (horn removed for photograph). It's terminals are bonded on one side to the mixer block (IF signal ground) and on the other side to the SMA jack inner conductor, which serves as IF output.

For the characterization and simulation, it makes sense to divide the mixer block into three electrical components, as shown in Fig. 2.8. This way, it is possible to distinguish between the influences of the separate sections to the signal transmission.

The junction is treated as a lumped element with an IF source impedance composed of the differential resistance R_D at the bias point ($\approx 2\,mV$) and the geometric capacitance of the junction C_J and the tuning structure C_T. The two other components are the RF blocking filters together with the bond wires to ground and the bonds to the SMA jack. Because the two parts have very different scales, they are separately modeled in CST MWS,
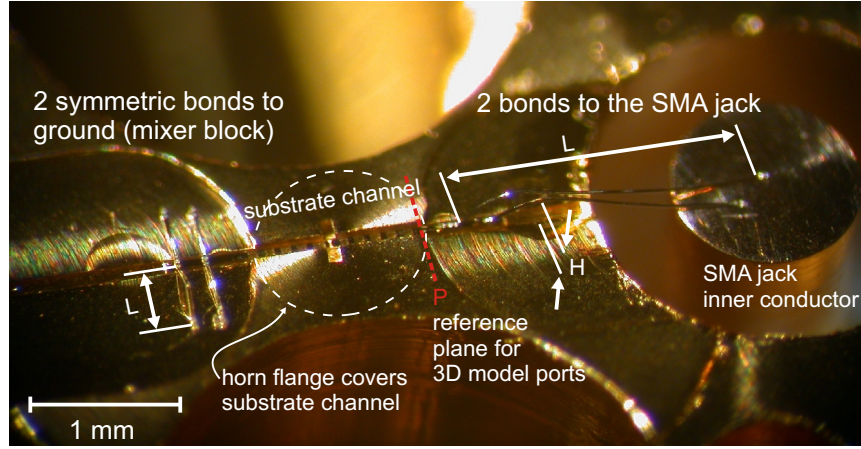
Fig. 2.7: *Magnified view to the bond area of the mixer block. Characteristic parameters of the wire bonds are added. The whole structure is simulated in two separate 3D models, which are connected via ports. Port reference plane location indicated by red dashed line.*
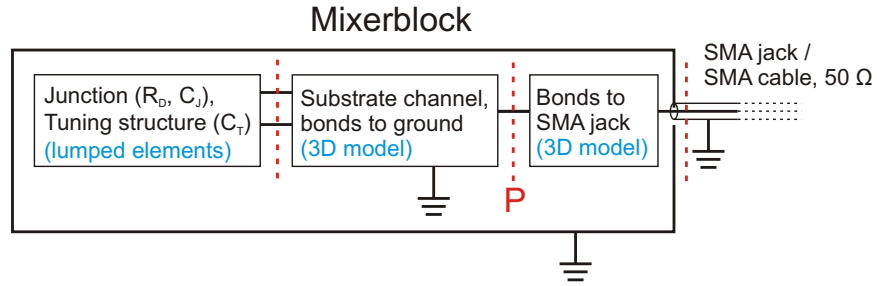
Fig. 2.8: *Schematic of the mixer block. Three building blocks are investigated separately. For the characterization of the entire mixer block, the sections are composed by means of S-parameter files which can be imported to AWR MWO.*

which strongly reduces the memory allocation during the simulation run and saves calculation time in comparison to a model including both structures: The Courant time (equation 2.1) of the small structure is much lower than the Courant time of the large structure because the large structure can be resolved by a coarse mesh. By separating the models, the short courant time has to be used for the simulation of the small structure only.

2.6.1   The bond wires to IF signal ground

Fig. 2.9 shows the model of the mixer chip and the bonds to signal ground. The junction is replaced by a "discrete port" (compare section 2.5.2) with $Z_0 = 50\,\Omega$ impedance. On one side it is connected to IF ground via the RF blocking filter and the bond wires. The blocking filter on the other side serves as IF output. In the simulation, it is terminated by a waveguide port

with an impedance of $(31 \pm 1)\,\Omega$ (results from the 2D solver). The model includes only regions where waves can propagate. The surrounding copper block is considered with perfectly electrically conducting (PEC) boundary conditions.
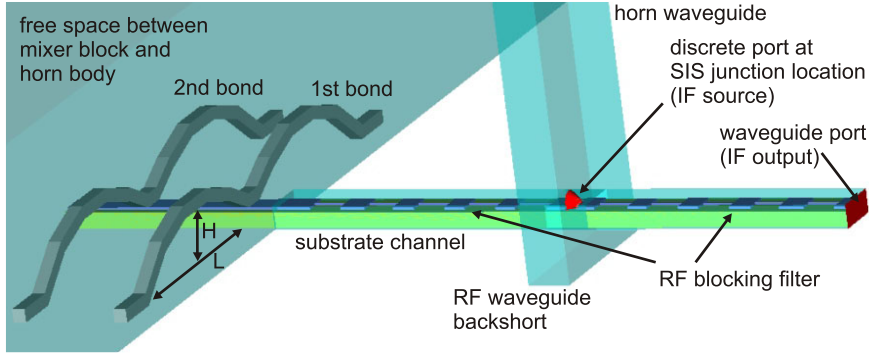
Fig. 2.9: *CST MWS model of the mixer chip including the bonds to the mixer block (IF ground). The symmetric and parallel construction of the bond wires lowers the inductive component (typical 0.25 nH). With a short bond length of 0.5 mm, the design can be used up to very high IF frequencies. The IF signal leaves the structure via the waveguide port on the right.*

The next plot (Fig. 2.10) shows the influence of the length of the bond wires at a fixed height of $H = 0.1\,mm$. Small variations in the grid structure due to small changes in the model (change of L), result in slightly different values for the IF output port impedance (from the 2D solver). Renormalization to $50\,\Omega$ frees the results from the influence of the port impedance and reveals a very high signal transmission even at frequencies far above the HIFI IF band. A more sensitive parameter is the bond height.
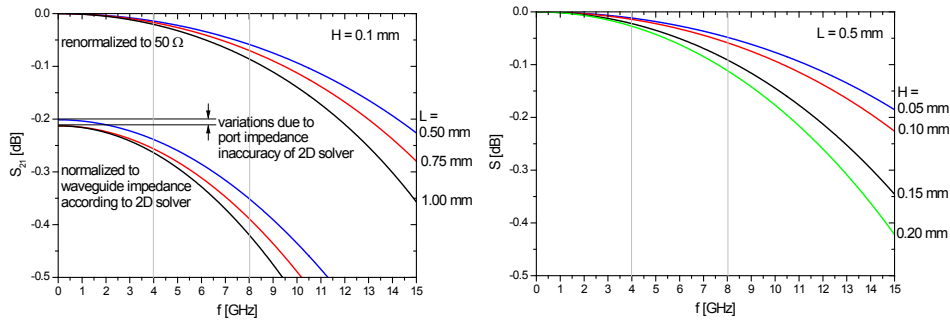
Fig. 2.10: *Left: Variation of the length L of the bonds to IF ground. The S-parameters obtained by CST MWS are renormalized to $50\,\Omega$ in order to obtain the real transmission characteristic. This also eliminates small inaccuracies in the impedance determined by port mode calculations with the 2D solver.*
Right: Renormalized S-parameters for various heights of the wire bonds to IF ground. The height is a critical parameter only for IF frequencies above the HIFI IF band.

A further investigation revealed the effect of damage or absence of one of the two bond wires in the standard configuration (L=0.5 mm, H=0.1 mm). The absence of the first bond elongates the connection from junction to ground and thus increases the inductive component, which makes such a configuration unusable for very high IF frequencies. A damage of the second bond wire is far less critical, as can be seen in Fig. 2.11.
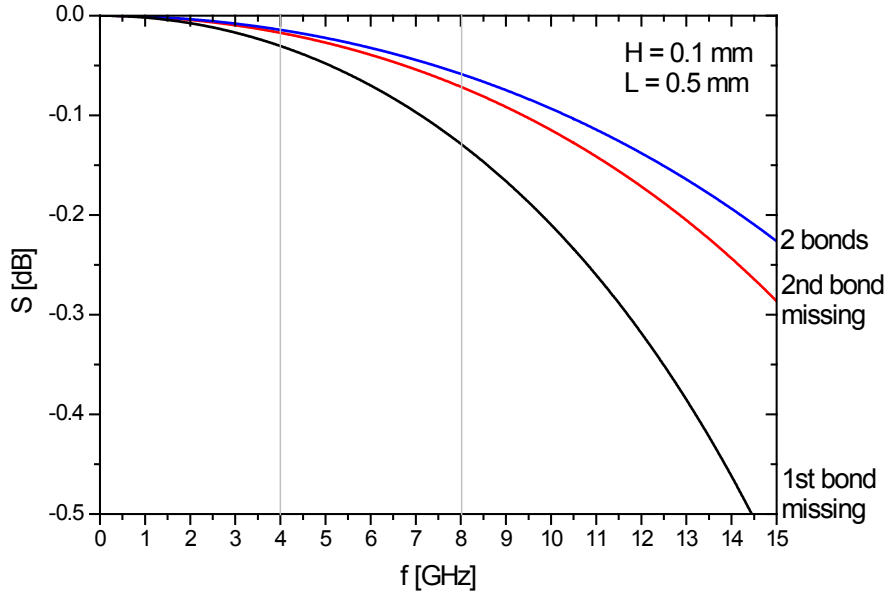
Fig. 2.11: *S-parameters for a missing bond wire for the standard config-uration (L=0.5 mm, H=0.1 mm). The absence of the first bond strongly increases the inductive component of the structure.*

2.6.2   The bond wires to the SMA jack

For the two bond wires, connecting the mixer chip with the SMA inner con-ductor, a similar technique can be applied. A view of the 3D model can be found in Fig. 2.12. In this case, the signal enters the structure at the microstrip waveguide port, which is adjacent to the waveguide port of the structure described in the last section. Hence these ports have the same geometry and impedance. The signal leaves the structure over the coaxial waveguide port formed by the SMA connector (50 Ω).

The effects of variation of the bond height and length have been investigated. The results are shown in form of renormalized S-parameters in Fig. 2.13. The plots show that nor the bond height neither the bond length is a critical parameter in the 4-8 GHz range. If a higher IF bandwidth is needed, the bond length is required to be as short as possible. By placing the SMA jack as close as possible to the mixer chip (L=0.7 mm), bandwidths up to 15 GHz can be achieved. However, if the SMA plug is placed very close to the mixer chip, it

2 bond wires
L = 2.0mm

free space between
mixerblock and horn

substrate
channel,
waveguide port,
Z= 31 Ω

coax, L = 2.5 mm
dielectric: air

SMA jack
inner conductor

coax, L = 5.5 mm
PTFE, ε_r = 2.1
coaxial waveguide
port, Z = 50 Ω
(not shown)

Towards
SIS junction

PORT
P=1
Z=50 Ohm

IND
ID=L1
L=0.4752 nH

TLINP
ID=TL1
Z0=50 Ohm
L=2.456 mm
Eeff=1
Loss=0
F0=0 GHz

COAXP2
ID=CX2
Di=1.3 mm
Do=2.5 mm
L=2.5 mm
K=1
A=0
F=1 GHz

COAXP2
ID=CX1
Di=1.3 mm
Do=4.1 mm
L=5.5 mm
K=2.1
A=0
F=1 GHz

IF output

PORT
P=2
Z=50 Ohm

electrical model for bond wires

Fig. 2.12: *Above: CST MWS model of the bonds to the SMA plug.*
Below: MWO model, discussed in section 2.6.3, used to extract the inductive
component of the wire bond connection.

interferes with the HIFI magnet pole pieces. In this case, a modified way for
the application of the magnetic field to the SIS-junction has to be found.
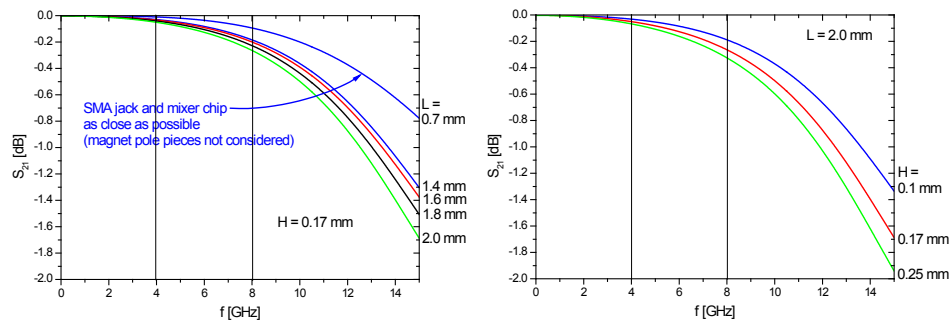
Fig. 2.13: *Left: Variation of the length of the bond wires to the SMA jack.*
Right: Variation of the height.
For a 4-8 GHz IF band, variations of the length and height of the bond wires
are not critical. For higher IF frequencies, the bond wire length has to be
reduced to a minimum.

2.6.3   Complete model of the mixer block

If all S-parameters of a 3D model are determined by a simulation, it is possible to create a "Touchstone" S-parameter file, which contains a list of S-parameters (Real/Imag or Magnitude/Angle) versus frequency. With the import into MWO, this file is converted to an internal admittance matrix and thus can be combined with lumped elements and other analytical models. This way, it is possible to investigate the IF band of the whole mixerblock including both 3D models of the bond wires and the effects of the capacitance of the SIS-junction and the tuning structure.

The junction capacitance is the most critical parameter in RF-design because it suffers most from fabrication tolerances. For the HIFI mixers, the UV-mask provides tuning structures for nominal junction areas of $(0.7 \times 0.7)\,\mu m^2$, $(0.8 \times 0.8)\,\mu m^2$ and $(0.9 \times 0.9)\,\mu m^2$. Fabrication tolerances resulted in areas as high as $(1.1 \times 1.1)\,\mu m^2$. The corresponding junction capacitances computed with a value of $85\,fF/\mu m^2$ [29] are 41 fF, 54 fF, 69 fF and 112fF for the excessively high junction area of $(1.1 \times 1.1)\,\mu m^2$. While these capacitance variations have tremendous effects to the RF band, the IF band is only moderately dependent to the junction capacitance.

Another contribution to the capacitance parallel to the junction source impedance steams from the 3-step microstrip transformer which matches the waveguide probe impedance to the junction at RF frequencies. It can be considered as a lumped element in the IF frequency range because of it's small dimensions. If one accounts for different transformer areas (ranging from $0.74\ 10^3 \mu m^2$ to $1.00\ 10^3 \mu m^2$) and the thickness tolerances of the SiO_2 dielectric ($210\,nm \pm 10\,nm$, $\epsilon_r = 3.8$), one obtains a capacitance of the tuning structure of $0.14\,pF \pm 0.03\,pF$. The values are taken from the UV-lithography mask design "NbTiN3" for the HIFI mixers of band 2. This results in nominal values from $C_{J+T} = 0.17\,pF \ldots 0.23\,pF$ for the overall capacitance of junction and tuning structure. When fabrication tolerances are included, this value may reach $C_{J+T} \leq 0.28\,pF$.

Fig. 2.14 compares the signal transmission for different cases. The inductive part of the bond wire sections partly compensates the junction capacitance. This makes it possible to use this design up to 12 GHz.

The Smith chart in Fig. 2.15 compares S_{21} from the 3D simulation and the analytic model depicted in Fig. 2.12. By means of a least squares fit, it is possible to extract the network parameters of the 3D model. For a bond length of 1.8 mm, the fit results in an inductive part of 0.47 nH. With a similar procedure, the inductive part of the bond wires to ground can be determined to 0.25 nH. The sum inductance (0.72 nH) together with the junction capacitance form a LC low pass with a cut-off frequency (-3 dB) of 13.2 GHz. This is in very good agreement with the plot in Fig. 2.14.

So far all calculations for the mixer block transmission assume an IF source
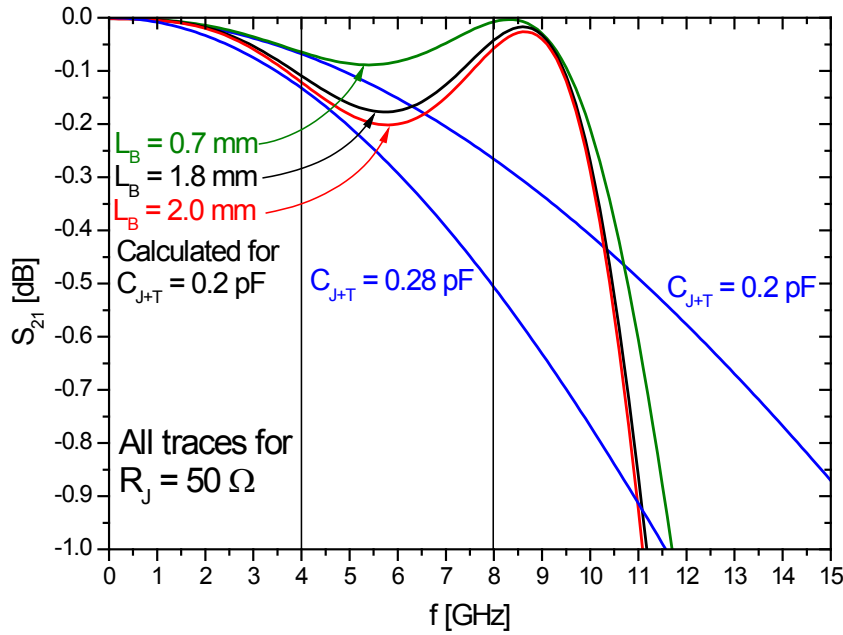
Fig. 2.14: *The influence of the capacitance of SIS-junction and tuning struc-*
ture for a typical value of $C_{J+T} = 0.2\,pF$, calculated for various lengths of
the bond wires to the SMA jack. The influence of the capacitance with-
out bonds is plotted for comparison. For this plot, the junction dynamic
resistance is assumed to be $R_D = 50\,\Omega$.

impedance of $50\,\Omega$. But the source impedance, which is equal to the dif-
ferential resistance R_D at the bias point, depends on many different factors.
These factors may be divided into parameters determined by the mixer chip
itself (critical current, junction quality, tuning structure, RF blocking filter)
influencing the RF bandshape and external parameters such as bias voltage,
LO frequency and LO power. A review of measurements of the flight mix-
ers reveals pumped I(V)-curves with R_D ranging from $60 \ldots 150\,\Omega$. In some
cases, very flat I(V)-curves close to the lower band edge at 636 GHz re-
sult in an $R_D \leq 250\,\Omega$. If the junction source impedance R_D differs from
the load impedance Z_L of the mixer block (which is terminated with a $50\,\Omega$
impedance), a part of the signal is reflected back into the junction. The
matching between R_D and Z_L can be illustrated when Z_L is plotted in a
Smith chart with constant impedance mismatch circles for different values
of R_D (Fig. 2.16). In this case, Z_L contains contributions from both bond
wire sections and a junction capacitance of $0.2\,pF$. For the bond wire config-
uration, most probable values for length and height are assumed (bonds to
ground: L=0.5 mm, H=0.1 mm, bonds to SMA: L=1.8 mm, H=0.17 mm). If
a section of the Z_{IN} trace lies inside a circle, the transmission is better than
the value indicated in the circles label.

The impedance mismatch between R_D and Z_L leads to a degradation of the
signal transmission. The calculations for the same R_D values as in the Smith
chart ($50\,\Omega$, $100\,\Omega$ and $250\,\Omega$). can be seen in Fig. 2.17.
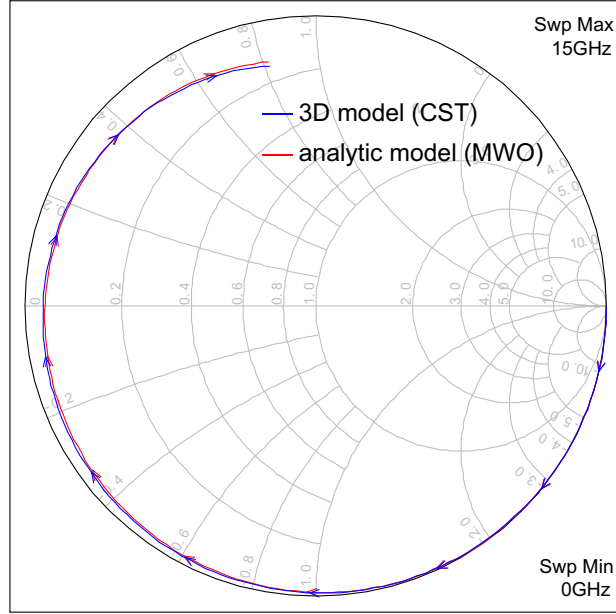
Fig. 2.15: *Smith chart with two S_{21} traces of the wire bond connection to the SMA jack. The inductive part can be extracted by fitting S-parameters of an analytic model (AWR MWO) to the results from the 3D solver (CST MWS). (Both models are shown in Fig. 2.12) The Smith chart shows congruence for an inductance of 0.47 nH for a bond length of 1.8 mm.*

2.6.4   Conclusions for the mixer block design

The investigation of the mixer block design reveals a good IF performance up to 12 GHz. The IF cut-off frequency is determined by the bond wire inductances and the geometric capacitance of junction and tuning structure. A parameter range analysis shows no critical values within the fabrication tolerances of both mixer chip and mixer block. For the most probable case where $R_D \approx 100\,\Omega$ (flight mixer chips from batch "PS8" over a large range of external parameters), the transmission does not degrade more than -1 dB. The results of the analysis are confirmed by noise temperature measurements in the 4-8 GHz range of the HIFI mixer units, which are presented in section 4.1.4 and 4.2.2. All calculations are valid under the assumption of a 50 Ω termination at the SMA connector of the mixer block. This assumption is guaranteed by the high transmission of the bias-T and the proper operation of the isolators, which absorb waves reflected at the poorly matched amplifier input port.
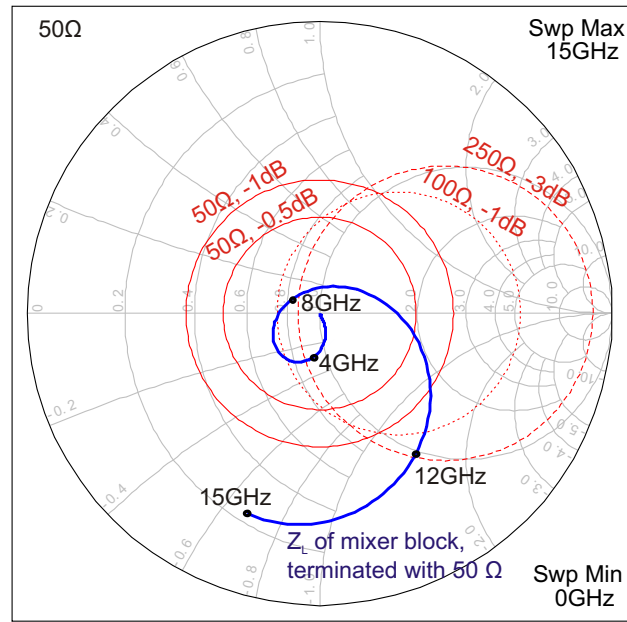
Fig. 2.16: *Smith chart (normalized to $50\,\Omega$) with Z_{IN} trace and constant transmission circles for $R_D = 50\,\Omega$, $100\,\Omega$, $250\,\Omega$ and various transmission values. When the Z_{IN} trace is inside a circle, the transmission to the indicated load value is better than the indicated transmission value. The Z_{IN} trace of the mixer block is calculated for $C_{J+T} = 0.2\,pF$, Bond to IF ground: L=0.5 mm, H=0.1 mm, Bond to SMA: L=1.8 mm, H=0.17 mm.*
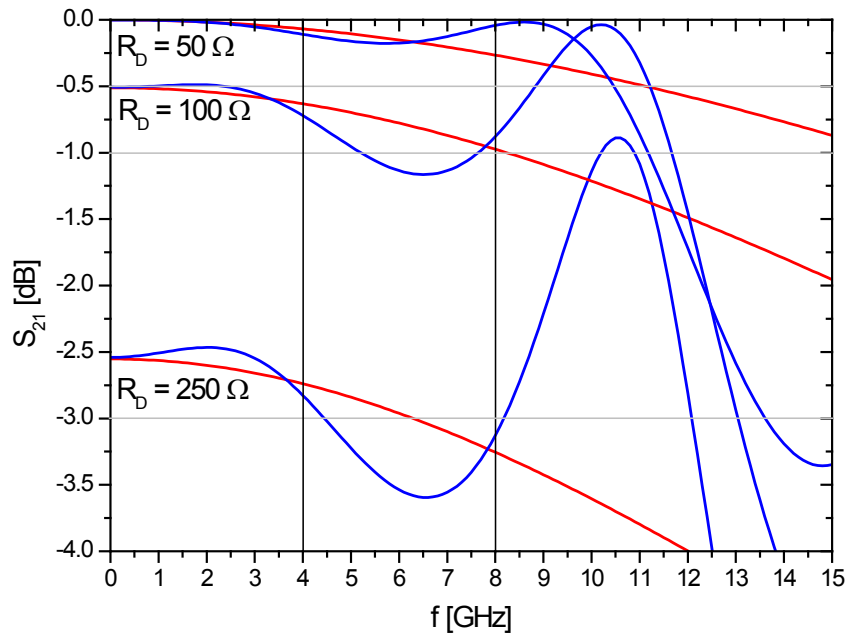
Fig. 2.17: *Transmission (S_{21}) through the mixer block at different source impedances R_D of the junction. For $R_D \leq 100\,\Omega$, the transmission in the 4-8 GHz range is still better $S_{21} > -1\,dB$.*

2.7   Bias-T design

This section presents the design of the bias-T. First the preliminary DM design is presented and then the major changes for the QM/FM models are explained. A detailed analysis of the influence of different components on the signal transmission (S_{21}) follows. The performance of the ESD filter section is analyzed regarding its behavior in the "human body" ESD model and its EMI rejection capabilities.

2.7.1   DM design

The HIFI bias-T and ESD-protection circuits were developed within the approved DM-QM-FM development cycles of the whole mixer unit. But already in the design process for the DM, decisions for most of the fundamental design issues were made:

- Two separate compartments for the ESD-filter (low frequency) on one side and the EMI-filter (high frequency) on the other side are used. This architecture blocks cross coupling from the bias supply connector, which is almost completely transparent for radiation within the IF band to the succeeding microstrip filter compartment.

- These two compartments are arranged in the free space which is not occupied by other MU components which allocate a fixed position in the envelope. (e.g., horn with mixer block in the optical axis, magnet and pole pieces close to the mixer block, connectors in the backplane) The compartment with the bias supply connector is placed on the left side of the MU backplane. The EMI-filter and bias-T circuit is placed on the top of the mixer unit in order to obtain a maximum flat area for the microstrip filters to gain flexibility in circuit design even at a late stage in the development cycle.

- All PCB substrates selected for the mixer unit are materials which already have space heritage. The material of the circuit substrates was chosen as follows:

  ESD filter board: 0.635 mm Alumina. (Although fabricated on 0.635 mm FR4-epoxy for the DM because of the tight schedule.) Alumina was chosen for the ESD-filter board because its coefficient of thermal expansion (CTE) is similar to that of the resistor and capacitor components (ceramic substrates), which are directly soldered to the board.

  EMI-filter board: 0.635 mm TMM10 with 0.0175 mm Cu laminate. TMM10 is suitable due to its high dielectric constant and its very low

thermal coefficient of $\frac{\partial \varepsilon_r}{\partial T} = -38\,ppm/K$) [30]. With $\varepsilon_r = 9.2$, it is possible to produce filter structures which are small enough to fit into the small compartment of the EMI-filter section. (For example, a quarter wavelength of a $50\,\Omega$ line at $4\,GHz$ is $7.4\,mm$.)

- The mixer block and the bias-T are connected with a semi rigid SMA cable [31], which is directly flanged to the bias-T box. The cable ensures a flexible connection between the mixer block (Cu) and the bias-T box (Al) (different coefficients of thermal expansion). The inner conductor is connected via two thin strands to the microstrip line. This construction assures a stable connection for both IF and DC bias voltage under thermal and vibrational stress and saves the space and weight of another (SMA) connector.

- The microstrip line is connected to the SMA jack via a flexible CuBe-foil ($25\,\mu m$, 98% Copper, 2% Beryllium) soldered into a small slit in the jacks inner conductor. This junction has proven high reliability, while maintaining a very low reflection coefficient.

Fig. 2.18 shows the DM mixer before final assembly with open top cover and open ESD box.

2.7.2   QM design

For the Qualification Model, the bias-T and EMI-filter section were completely redesigned in order to transform all structures into a space-qualifiable design and to obtain a better performance. The major changes in comparison to the DM are as follows:

- The TMM10 board was replaced by a combination of RT/Duroid6002 for the signal path and TMM10 for the filter section. With the Duroid substrate, it was possible to obtain a better IF signal transmission of the bias-T. The $50\,\Omega$ transmission line on the Duroid substrate ($\varepsilon_r = 2.94$) has a width of $2.0\,mm$ in comparison to $0.67\,mm$ on TMM10. This makes it more easy to obtain a low reflection transition to the input SMA cable and to the output SMA jack. Furthermore, the single layer blocking capacitor (ATC111 series) with a $1.27 \times 1.27\,mm^2$ footprint fits much better to the broad microstrip line on the Duroid substrate.

  The filter section remains on the TMM10 board because it is more easy to implement a high performance band rejection filter in the small housing on a high-ε_r substrate.

- The filter section was changed to achieve the full 4–8 GHz band.
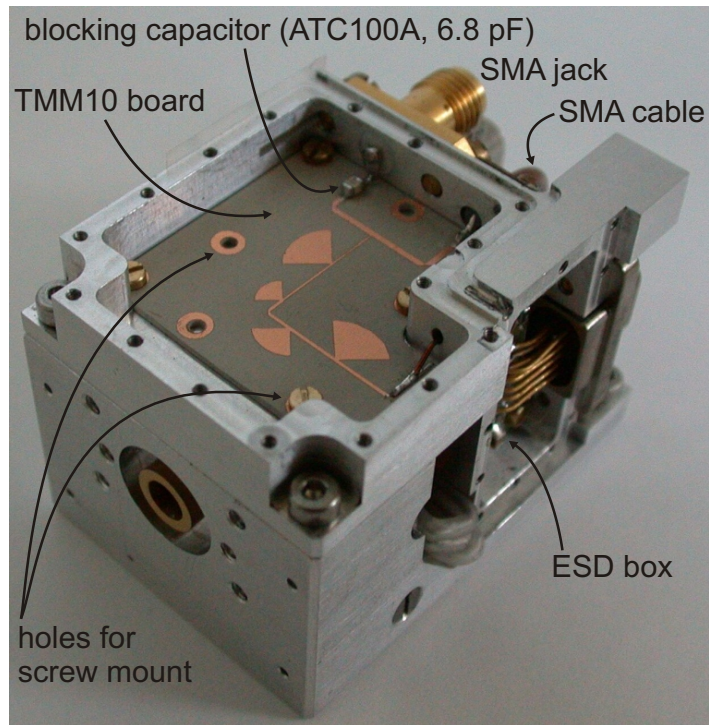
Fig. 2.18: *DM mixer unit with removed covers. This first prototype already implements most of the features of the final design. Although the prototype was not intended to implement a space qualifiable design, this model is still operating in a test set-up at SRON and survived a large number of cool downs to operating temperature.*
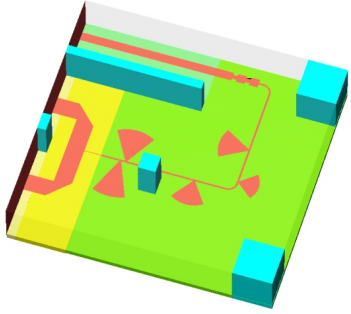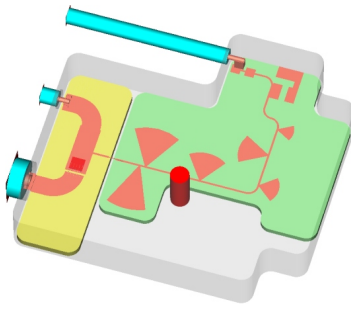
- The test boards for the QM design are milled with a special milling machine. The final substrate batch is manufactured by Printech (GB). The metallization is structured by wet etching and the surface is plated with $1\,\mu m$ gold. The board outline is milled in the same way as for the test boards.

- Instead of using many small screws, the substrates were glued to the gold plated housing with conducting epoxy glue (Ablefilm 5025E).

- A small pillar was introduced joining the top cover of the box with the ground plane. This suppresses a box resonance at 7.9 GHz and increases the overall EMI-rejection capability of the filter.

- The blocking capacitor was changed from a multi layer to a single layer capacitor, which is more reliable. This also increases the transmission of the bias-T.

- The height of the SMA jack over the Duroid substrate was adjusted for optimum performance (lowest reflection). This has the additional benefit of making it easier to fit the geometry into a very late change of definition of the mixer envelope.

2.7.3 FM design

The only change between the FM and the QM is a slight change (0.2 mm) of the height of the SMA cable over the Duroid substrate. By placing the cables inner conductor directly over the microstrip line, the transmission could be slightly improved. This change did not affect the reliability of the junction.

2.7.4 Software models for the bias-T

Parallel to the hardware development evolved the software models used for the simulation of the circuits. Tab. 2.1 summarizes the main differences between an early 3D model used during the QM design phase and the final model.

	Old model	New model
box	CST bricks, approx. dimensions	.dxf file based structure with exact outline
substrate	CST bricks, partly lossy. (in the vicinity of the waveguide ports only lossless structures can be used)	.dxf-file, exact PCB dimensions, with $\tan(\delta)$ according to the substrate datasheets.
ports	microstrip waveguide port on lossless PCB (in CST waveguide ports have to be lossless)	waveguide port with the exact dimensions of the SMA cable and the SMA jack
blocking capacitor	replaced by an inter-connecting piece of Cu microstrip	high-ε_r structure ($\varepsilon_r = 64$) with capacitor dimensions and bond wires
model		

Tab. 2.1: *Comparison of an old 3D model in CST MWS with the final model, where all details are very close to the real dimensions of the circuit.*

Although most of the design concepts were implemented already in the DM, a lot of small design changes and optimized structures in the QM and FM could strongly improve the performance of the circuits. (Performance measurements are presented in section 4.1.) Fig. 2.19 shows a schematic with

all relevant building blocks of the bias-T. All blocks were investigated and optimized separately. Their interactive behavior was investigated in a large CST MWS simulation and in real world measurements.
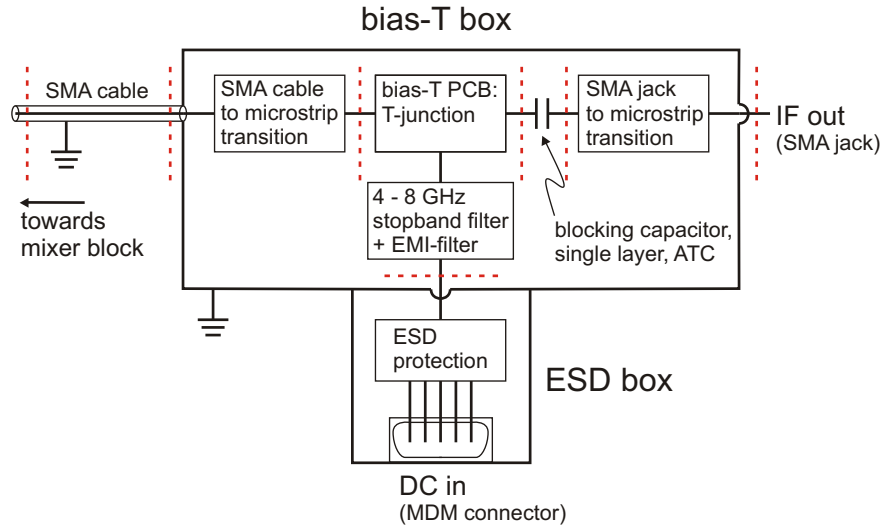
Fig. 2.19: *Schematic of the bias-T circuit with all relevant building blocks. Red lines indicate reference planes where the circuit can be decomposed for characterization in separate models.*

2.7.5 Development of the 4-8 GHz blocking filter and the EMI rejection filter

Fig. 2.20 shows PCB layouts from different design stages. The filter section, situated on the TMM10 board, is made of a very narrow (w=0.2 mm) microstrip line, which results in an high impedance of $Z = 79\,\Omega$. Radial stubs with different radii and angles are arranged along this line.

The first three radial stubs provide the stop band from 4-8 GHz. They generate a very low impedance at their foot point over a broad frequency span around their appropriate center frequency. In the final design, three other radial stubs are used for filtering in the range above 8 GHz. Of cause, such a complex design problem is best solved with software support. However, due to the inaccuracy of the models for the radial stubs in MWO (compare section 2.5.1), the first circuit designs (Fig. 2.20 (a)) showed inter-stub resonances, which appeared to lay within the 4-8 GHz operating range, whereas the MWO model showed a clear band. (Compare Fig. 2.21.) In order to understand the resonances, a CST model was created and H-field monitors were set up to determine the field distribution at the center frequencies of the resonant spikes. The field monitor revealed a resonance at about 4.3 GHz between stub 1 and 2 (fundamental with current-antinode between the stubs) and a resonance at 7.6 GHz between Stub 2 and 3 (1st harmonic with 2
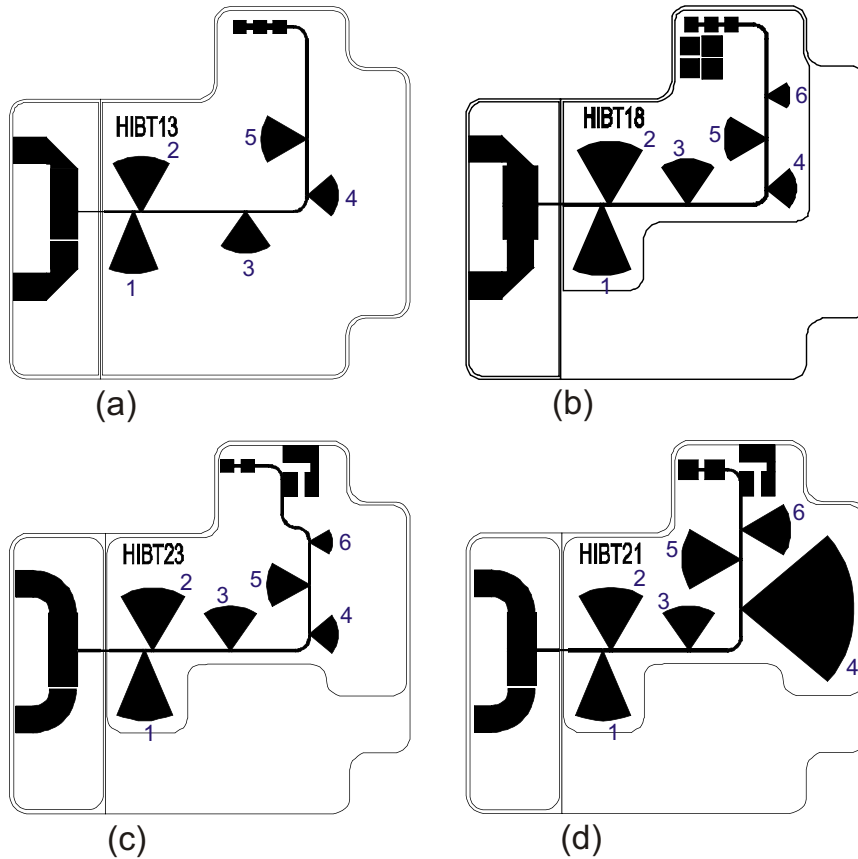
Fig. 2.20: *Four different layouts of the bias-T circuit:*
a): HIBT13, old design with inter-stub resonances within the IF band.
b): HIBT18, new filter design with clear 4-8 GHz band. The T-junction is broadened for compensation of the T-junction inductance.
c): HIBT23, same filter as in b). The T-junction broadening is now distributed over a longer section of the broad line by means of curved lines instead of the mitered bends.
d): HIBT21, new filter design with full 4-8 GHz band and additional EMI rejection in the 1-4 GHz band by means of the large stub and an additional ATC700B, 100pF capacitor.

current-antinodes between the stubs), as can be seen in Fig. 2.22. Once the origin of the spikes became clear, it was possible to chose another configuration with the spikes moved outside the HIFI IF-band and with a similar filter performance (Fig. 2.20 (a)). Fig. 2.23 shows simulation results for the band rejection of the QM/FM, which proved its EMI-rejection performance in an official EMI-test in the NLR test facility (NLR, Noordoostpolder, NL). Measurement results of these tests can be found in section 4.3.
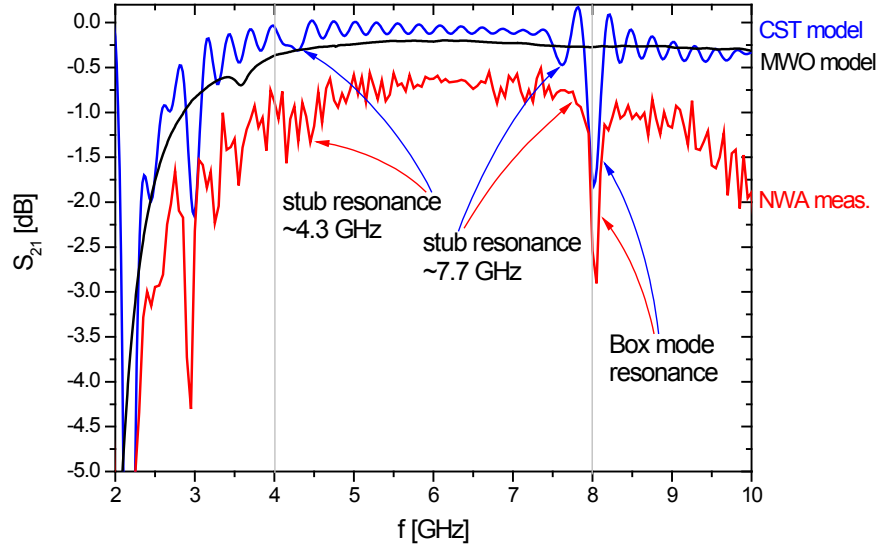
Fig. 2.21: *Transmission (S_{21}) disturbed by inter-stub resonances at 4.3 GHz and 7.8 GHz.*
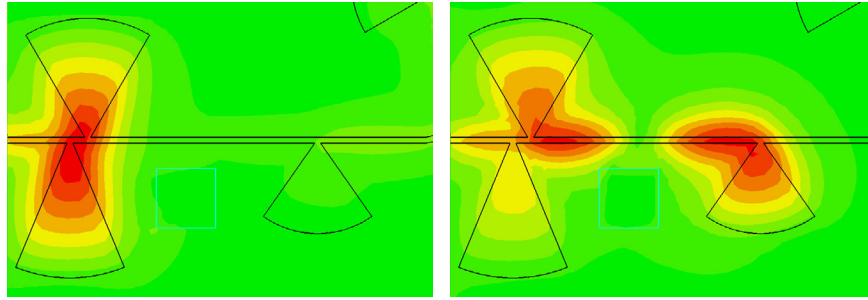
Fig. 2.22: *H-field monitors at a plane slightly above the PCB. Left: Monitor at 4.3 GHz with current antinode between stub 1 and stub 2 Right: Monitor at 7.8 GHz. First harmonic with two current antinodes between stub 2 and stub 3.*

2.7.6   Enhancement of the T-junction

The IF signal path in the first models consists of a simple $50\,\Omega$ microstrip line. The U-shape of the line was achieved by using two 90° mitered bends. The optimized miter assures a very low reflection coefficient of the bends (in this configuration $< -40\,dB$). The T-junction in the signal path was designed as a short stub of 0.2 mm width, which is connected to the filter section via bond wires. A drawing of this structure can be seen in Fig. 2.20 (a). Although the entire signal power entering the filter is reflected back in the 4-8 GHz range, this configuration did not result in an optimum transmission to the IF-output. A part of the signal was reflected back by the T-junction into the input port.

Following [32], the T-junction can be described with the equivalent circuit shown in Fig. 2.24 b). An least squares fit of S-parameters of a simplified
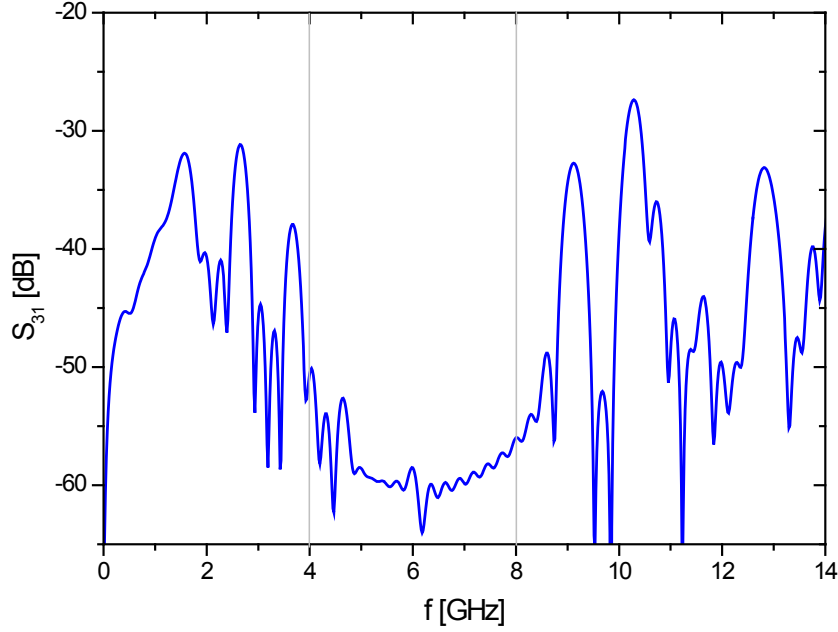
Fig. 2.23: *Simulated EMI rejection performance of the filter section in the bias-T. Within the 4-8 GHz range, the transmission is $S_{31} < -50\,dB$.*
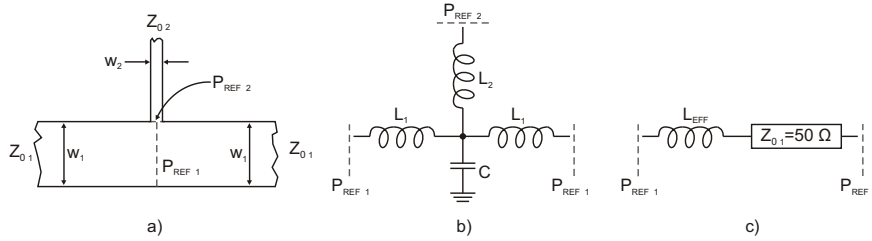
Fig. 2.24: *Equivalent circuit for a microstrip T-junction.*
a) The geometry of the microstrip T-junction including reference planes $P_{REF\,1}$ and $P_{REF\,2}$.
b) Equivalent circuit of the T-junction (from [32]).
c) Simplified equivalent circuit. The influence of the junction capacitance C and a part of the inductance $L_1 + L_1$ is considered with a $50\,\Omega$ line, which just contributes a phase shift in the $50\,\Omega$ system. The remaining part L_{EFF} can be fitted by comparing the simplified model to simulations and measurements.
In the bias-T it was necessary to compensate for L_{EFF} with a broadening of the microstrip line on the RT/Duroid6002 board and the introduction of curved lines instead of mitered bends.

model (Fig. 2.24 c)) to simulations of the T-junction revealed an effective inductance of $L_{EFF} = 0.04\,nH$ in the signal path for microstrip lines with $w_1 = 2.0\,mm$, ($Z_{0\,1} = 50\,\Omega$) and $w_2 = 0.2\,mm$, ($Z_{0\,2} = 134\,\Omega$) on RT/Duroid6002. In order to compensate for this inductive component, the lines on both sides of the T-junction have been broadened to $2.5\,mm$ ($Z_{0\,1} = 42\,\Omega$). This design has been used in bias-T "HMBT3", which was used for the EMC tests. The layout is depicted in Fig. 2.20 (b)).

Simulations and measurements of the bias-T input reflection S_{11} of different configurations of the T-junction revealed that the compensation of the T-junction, together with effects of the filter section, can best be done with a more distributed broad line. In order to achieve a line with the appropriate electrical characteristic and without changing the geometry, the mitered bends were replaced with microstrip curves with a width of 2.0 mm. They have an effective line impedance of $Z_0 = 44\,\Omega$ (which corresponds to w=2.4 mm for a straight microstrip) and add an additional capacitance of 0.2 pF to the circuit. By using the microstrip curves, the width of the broad line is reduced to 2.2 mm.

With this configuration, a reflection coefficient of the T-junction as low as $S_{11} \le -20\,dB$ could be obtained. The final layout of the T-junction, which was used for the QM, FM and FS, is shown in Fig. 2.20 (c) and (d).

2.7.7　Box mode suppression in the EMI filter compartment

S-parameter measurements with a network analyzer during the DM-design phase revealed a sharp dip in the transmission curve at 7.9 GHz (compare Fig. 4.1 in chapter 4.1). This dip could be identified as box mode in the bias-T compartment because it only appeared when the box was closed by its cover. Upon delivery of the DM, there was no other method of box mode damping than with a small piece of "Eccosorb" absorber material, which was clamped into the box. This was not an option for the flight hardware because the absorber material is very brittle, difficult to fix in the housing and may cause problems by outgasing. To gain insight into the nature of the box resonance, the mode frequency was calculated from the box dimensions given in Fig. 2.25. The eigenfrequency f_e of an electromagnetic mode in a cuboidal box can easily derived from the boundary conditions (electrically conducting walls, no tangential E-field:

$$\frac{c}{f_e} = \lambda_{e\,(k,l,m)} = \frac{1}{\frac{k^2}{4a^2} + \frac{l^2}{4b^2} + \frac{m^2}{4c^2}} \tag{2.3}$$

The only reasonable results are obtained from (k,l,m)=(1,1,0), corresponding to a mode with E-field perpendicular to the drawing plain. One obtains with $b = b1$, $f_e = 8.7\,GHz$, with $b = b2$, $f_e = 7.4\,GHz$ and with an intermediate $b = \overline{b}$, $f_e = 7.9\,GHz$ where

$$\overline{b} = \sqrt{\frac{b_1^2 a_1}{a} + \frac{b_2^2 a_2}{a}}$$

The dielectric loading of the box by the Duroid and the TMM10 board does only slightly change the resonance frequency because of the small fill factor ($V_{Dur}/V_{Box} = 3\%$, $V_{TMM}/V_{Box} = 6\%$) and because the boards are situated close to the box wall rather then in the box center.
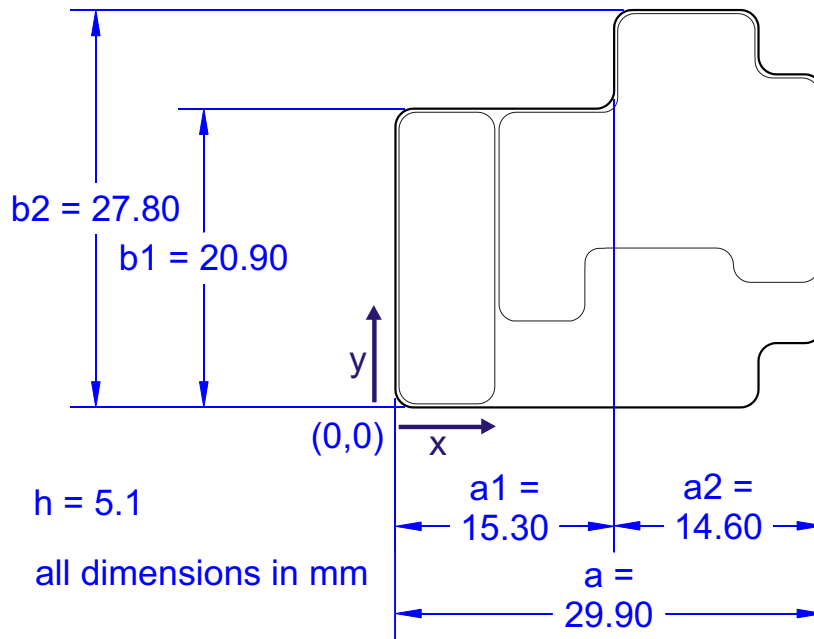
Fig. 2.25: *Bias-T box and PCB outlines for the estimation of the (1,1,0) box mode resonance frequency f_e.*
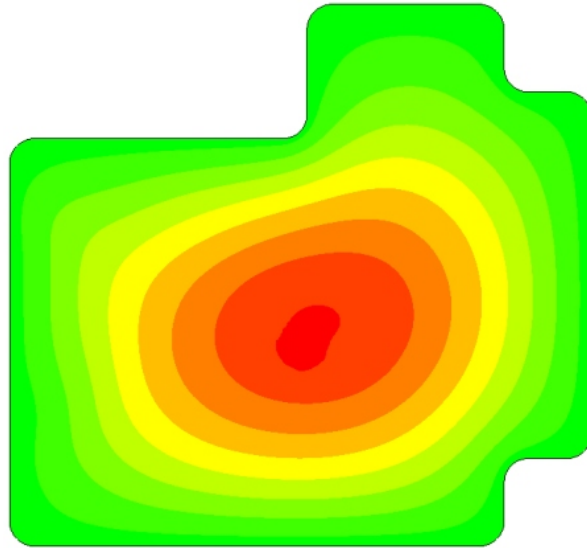
Fig. 2.26: *Box resonance at 7.9 GHz. CST MWS field monitor showing the E_z-field in a cutting plane through the box center.*

Later on, when the 3D-field solver became available, this result has been verified using CST MWS with a field monitor showing the E-field in a cutting plane through the box center. For the final bias-T design with reduced TMM10 board size, the 3D solver evaluates the box mode frequency to 7.9 GHz, which exactly fits to network analyzer measurements.

Because of design and schedule issues, it was not possible to redesign the

geometry of the box. Thus, an other way had to be found to influence the box mode. The simplest way is to change the boundary conditions by means of a metallic pillar located close to the E_z-field maximum of the mode. Thus, the field strength is clamped to zero at the pillar location.

Fig. 2.27 (left) compares the transmission of the bias-T with the pillar, with absorber and with the cover left open. The box resonance is suppressed in all three cases. Furthermore, it is interesting to see that the transmission at higher frequencies is much better with the pillar. With increasing frequency, the signal line and the filter tend to radiate a part of the signal to free space. While this part of the signal is absorbed by the Eccosorb or leaves the box in case of open cover, it is reflected back into the structure by the metallic cover if only the pillar is present.
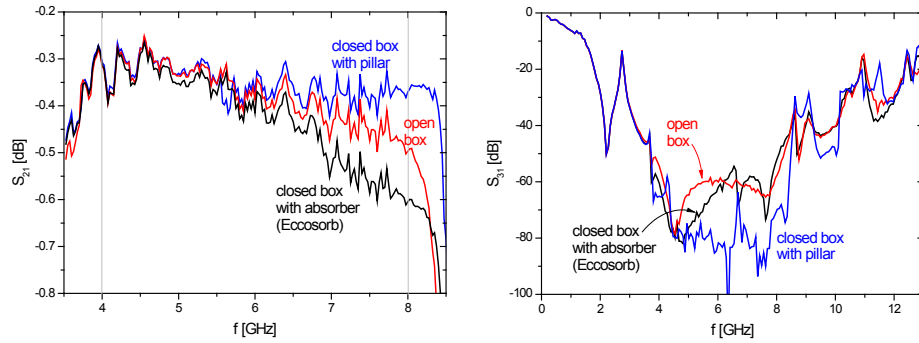
Fig. 2.27: *Left: Measured transmission of the bias-T for different configurations of box mode suppression. Suppression by means of a small metallic pillar in the box center results in the lowest attenuation at high IF frequencies. In the other configurations, a fraction of the incoming power is radiated into free space (absorber or open boundary).*
Right: Improved EMI rejection due to the pillar.

A likewise positive influence of the pillar can be observed regarding the EMI rejection performance of the filter. Fig. 2.27 (right) shows that the pillar prevents the radiation entering the box via the bias wire from bypassing the filter and being coupled to the 50 Ω line (for $f_{IF} > 4\,GHz$).

This measurement was done with a special bias-box with the ESD compartment replaced with an SMA connector. This box was also used to determine the optimum position of the pillar by measuring S-parameters for different pillar positions with closed box cover. While the pillar position did not have any measurable influence to the transmission within the 4–8 GHz band, the EMI-suppression performance is strongly dependant on this parameter. Fig. 2.28 presents a selection of the recorded S_{31} (=EMI rejection) measurements. The optimum position for the pillar turned out to be (x,y)=(16 mm,11 mm) where the y-value is restricted by the TMM10 board outline.
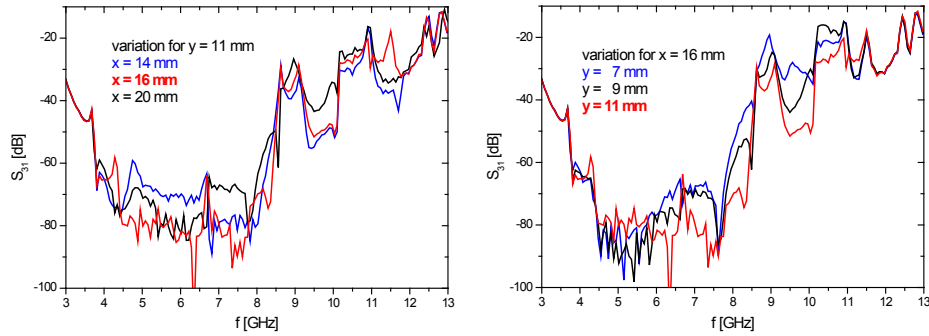
Fig. 2.28: *Selected S_{31} measurements for the investigation of the optimum pillar position (minimum S_{31}).*
Left: Variation in x-direction.
Right: Variation in y-direction.
Optimum pillar position is (x,y)=(16 mm,11 mm).
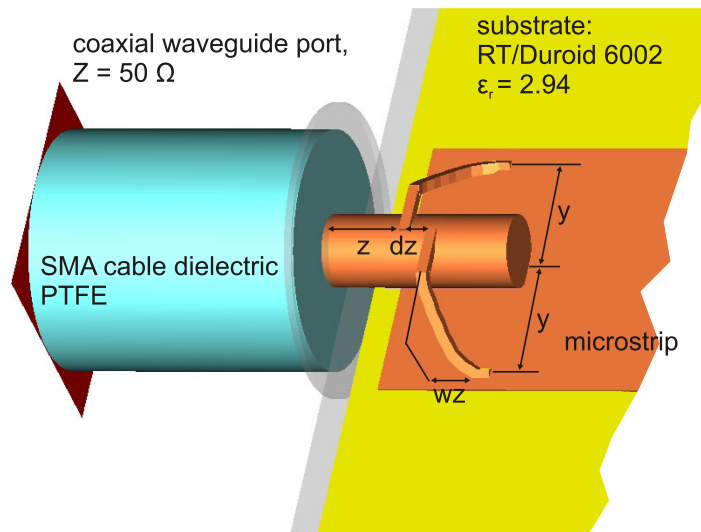
Fig. 2.29: *CST MWS model of the SMA cable to microstrip transition. The topology of the strands is characterized by four parameters. Only y and z have a significant influence on the transmission quality.*

2.7.8   The SMA cable to microstrip transition

The IF signal enters the bias-T compartment via an SMA cable and is guided to the microstrip line by a special transition. It provides a reliable connection for both the 4-8 GHz IF signal and the bias voltage for the SIS-junction. This transition is specially designed for the band 2 mixer unit because no standard connection could be used due to the stringent weight and volume limits for the mixer unit. Because this transition is used first time in space, many efforts have been spent in development and testing. Three different configurations of the tiny ($d \approx 50\,\mu m$) silver plated strands, which assure the DC contact, have been investigated. In this section, a parameter analysis of the final (flight-) version is presented.
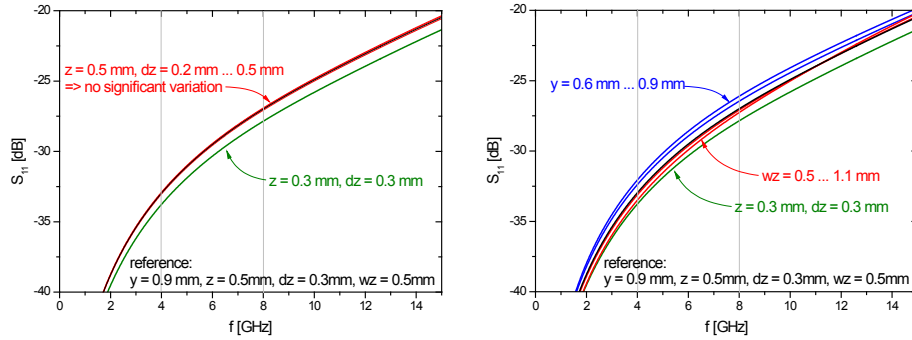
Fig. 2.30: *Power reflection S_{11} at the SMA cable to microstrip transition in dependence of various parameters. Reference is the black line, variations in colored traces. (For the definition of wz, y, z and dz, see Fig. 2.29.)*
Left: z and dz (asymmetry of strands) variation.
Right: wz and y variation.
Only y and z have a significant influence on the transmission quality.

Fig. 2.29 shows a 3D model for simulations in CST MWS. Although the model is slightly simplified, it represents a good electrical equivalent with all relevant parameters. With the simulation, the tolerant parameters and those which are critical in terms of signal transmission, could be identified. The design parameters which can be used to obtain flexibility to avoid thermal stress without losing transmission performance, have been found. Furthermore, the parameter variations could give a first answer on if it is feasible to produce the structure by manual work without exceeding the tolerances.

Fig. 2.30 (left) shows the reflected power (S_{11}) in dependency of the distance between box wall and strand origin, *z* and of the strand asymmetry, *dz*. While the asymmetry *dz* does not have any noticeable effect, the distance to the wall should be kept as small as possible. In the manufacturing process, this is achieved by a special clamping mechanism, which fixes the strand as close as possible to the beginning of the outer conductor, while allowing a free distribution of solder and flux. (Compare Fig. 3.9 in section 3.3.4.)

In Fig. 2.30 (right) it can be seen that the transmission increases with *y*. The reflection is minimized when the wave is launched over the full width of the microstrip line. By using the maximum possible *y*-value, the structure gains flexibility due to the increased slack in the strands. This makes the junction easily resist thermal cycling, although materials with very different coefficients of thermal expansion are used for the connection. Furthermore, the parameter *wz* can be used to increase the slack without degrading the performance.

Beyond the parameter analysis, the 3D-solver results could be used to generate Touchstone S-parameter files, which could be integrated into the AWR MWO closed-form model.

2.7.9   The SMA jack to microstrip transition
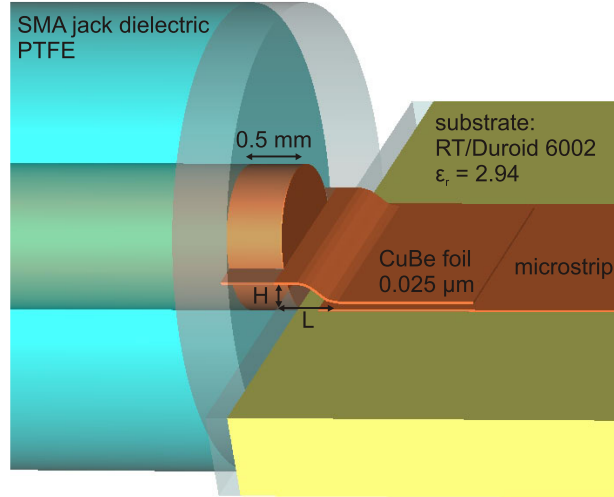
Fig. 2.31: *CST MWS model of the SMA jack to microstrip transition. The thin CuBe foil gives mechanical flexibility to compensate for thermal contraction.*
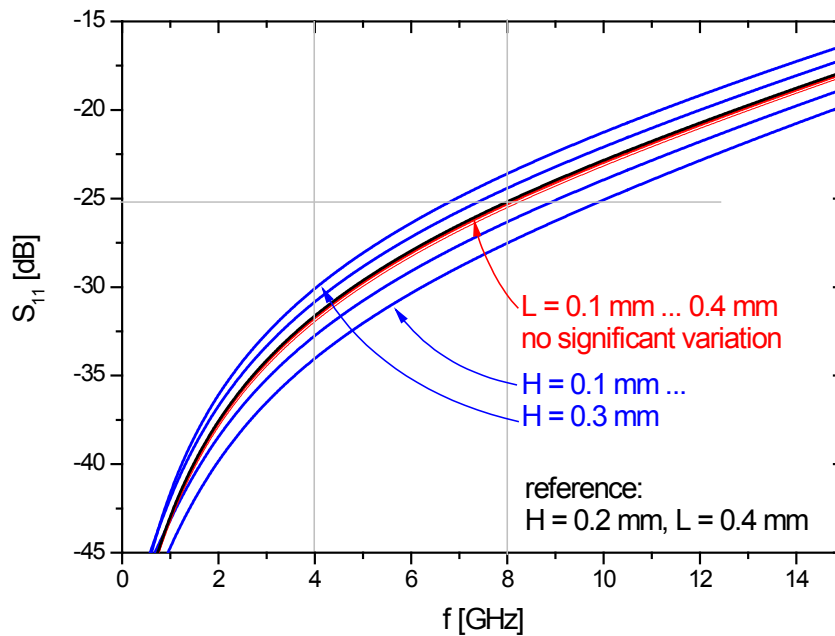
Fig. 2.32: *Reflection (S_{11}) of the SMA jack to microstrip transition in dependency of H and L. Because only H has a significant influence on S_{11}, H is reduced to a minimum of 0.2 mm and L is used to gain flexibility for the structure.*

Similar to the SMA cable to microstrip transition, the connection SMA jack to microstrip is a special design for the mixer units for band 2. In the HEMT amplifier group at the "Centro Astronómico de Yebes", a solution for a transition suitable for cryogenic operation was proposed [33], which did not exactly fit

the needs for the mixer unit. Thus, a new transition had to be designed. The 3D model and the corresponding parameters are shown in Fig. 2.31. The S-parameter plot (Fig. 2.32) shows that the length of the free part of the CuBe-foil is an uncritical parameter, which can be used to gain flexibility. For the height over the microstrip line, h=0.2 mm is chosen, which guarantees flexibility under cryogenic conditions and still results in an excellent low reflection coefficient of less than -25 dB over the whole IF band.

2.7.10   The blocking capacitor

The blocking capacitor is needed to separate the bias voltage from the IF output. Otherwise the bias voltage would induce a current through the first isolators termination resistor, which would induce shot noise and an additional heat load to the 2.8 K stage of the HIFI cryostat. (The IF amplifier likewise has a DC blocking capacitor at its input.) For a transmission of an ideal capacitor in a 50 Ω line, a minimum value of 2.7 pF is required in order to obtain a minimal loss of -0.1 dB at 4 GHz. For the bias-T, a value of 6.8 pF or 7.5 pF is preferred to minimize the influence of the reactance. For these values, the pure reactance can be neglected in comparison to the parasitic losses in the capacitor.
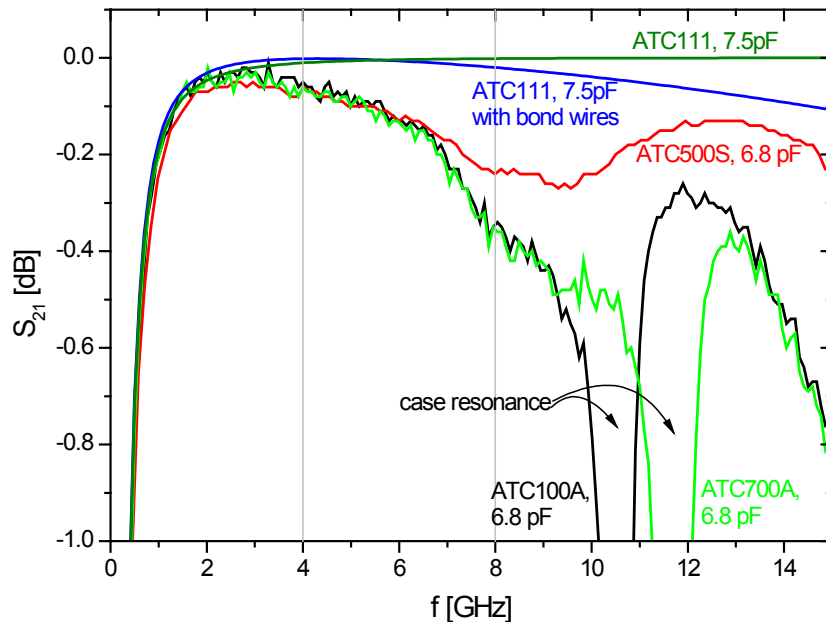
Fig. 2.33: *Signal transmission of various capacitors, which have been tested for the use in the bias-T. The transmission is calculated for the capacitor in a 50 Ω line. Data from ATC Touchstone files and a single layer capacitor model with design values from ATC TechSelect.*

For the DM bias-T, a multi layer capacitor from "American Technical Ceramics" ATC100A, 6.8 pF was used. Because gluing technology was not available

at this time, this capacitor had the big advantage that it could be soldered directly to the TMM10 board. In addition to a lower reliability, the high ohmic losses in the capacitor due to a case-resonance at 10.6 GHz make this multi layer capacitor unattractive for the application in the HIFI bias-T.

During the QM design phase, other capacitors have been tested. Among them another multi layer capacitor from the ATC700A series, which has a slightly better transmission and two single layer capacitors. The first single layer capacitor, ATC500S could be glued or soldered directly to the microstrip line. Unfortunately, this capacitor failed after a few cool downs to 4 K. The ceramic body of the capacitor peeled of from the terminals, which remained at the microstrip. The final solution was an ATC111 single layer capacitor, which has to be glued to the microstrip. The other side of the capacitor has to be bonded with 5 to 7 wedge bond wires (Au, $25\,\mu m$) to the other microstrip contact (compare Fig.3.13 f)). This bonding step is rather elaborate because bonding to the soft RT/Duroid6002 substrate is only possible in a small range of the parameters bond force, bond power, bond time and substrate temperature. The bonding procedure was developed together with Hymec, NL, where the bonds have been applied for all QM-, FM- and FS- bias-T capacitors.

Models for the capacitors have been included in the closed-form model in AWR MWO. For the multi layer capacitors, Touchstone S-parameter files are available. The ATC111 capacitor has been derived from a chip capacitor model with $Q(1MHz) = 660$ and $f_{RES} = 13.76\,GHz$. These data have been taken from ATC Tech-Select [34]. The transmission of various capacitors is shown in Fig. 2.33.

2.7.11 The ESD-filter

The ESD-filter board is located in a second compartment, which is connected to the bias-T circuit by a thin Habia-wire (AWG34), which is guided through a small hole ($d = 0.8\,mm$). This geometry is chosen to avoid electromagnetic coupling between the two filters, which highly improves the overall filter performance. The ESD-filter enables EMI-rejection in the low frequency range. Furthermore, the ESD-filter protects the SIS-junction during the assembly of the FPU and other procedures where the mixer unit may be exposed to a risk of an electrostatic discharge.

The design is similar to the design developed at SRON for the mixer units of band 3 and 4 because the filter is the interface to the bias electronics, which are also developed at SRON. The ESD filter design has been developed in close cooperation with the bias electronics design. Fig. 2.34 presents the schematic of the final ESD-filter design including the mixer chip. A lot of different constraints limited the choice of the optimum circuit design:

- Five wire bias scheme.
  The circuit needs to implement a five wire bias scheme, which allows
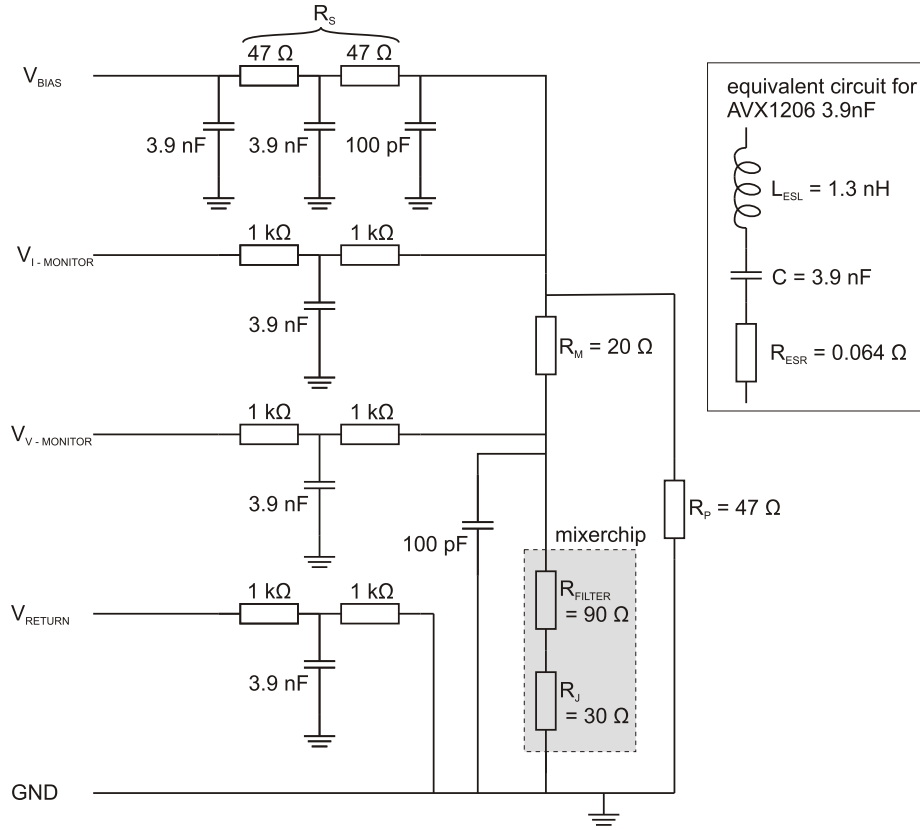
Fig. 2.34: *Schematic of the ESD filter circuit. The box (top right) contains an equivalent circuit for the AVX1206 3.9 nF capacitor, which was used for the EMI rejection calculations. The mixer chip is likewise added with an equivalent circuit. At room temperature, the RF blocking filters provide additional ESD protection of the junction by a resistance of $R_{FILTER} \approx$ 90 Ω.*

to install a protective resistor R_P in parallel to the junction. Despite of the resistor, it is possible to measure junction voltage and current via three sense lines.

- Common mode rejection (bias supply).
  Not only the bias- and the sense-lines need filtering by an RCR T-element but also the sense-return line (V_{RETURN} in the schematic). This is needed to improve the common mode rejection of the bias supply circuit. It would have been better to locate the components on the supply board, which is operated at room temperature, rather than on the ESD-filter board, which has a tight envelope. Each additional component is an additional single point of failure at cryogenic temperatures.

- Thermal budget.
  The values of the current guiding resistors have to be kept low in order to not exceed the thermal budget of the mixer units. Thus, the HIFI bias electronics is adapted to the following values: $R_M = 20\,\Omega$, $R_P = 50\,\Omega$ and $R_S = 100\,\Omega$.

- Capacitor reliability.

  On a common parts procurement meeting the mixer groups and SRON QA/PA agreed on 10 nF capacitors with NP0 dielectric and 1206 case size. ESA refused the use of these capacitors and agreed only with a capacitor with a smaller value (3.9 nF) because of doubts in the reliability of the 10 nF parts. Thus, the final part list only contains values of 10 pF, 100 pF and 3.9 nF.

Considering these constraints, the filter of the bias-line had to be designed for an ESD-performance comparable to that of the sense-lines and a sufficient EMI-rejection in the low frequency range.

For EMI-rejection calculations, one needs exact electric models for the used parts. For the ATC capacitors (10 pF, 100 pF), S-parameter models are available. For the AVX 3.9 nF capacitor, a C-R-L series model could be extracted from values given by the program SpiCap provided by AVX. The equivalent series resistance $R_{ESR} = 0.064\,\Omega$ and the equivalent series inductance $L_{ESL} = 1.3\,nH$ could be obtained, which results in a resonance frequency of 71 MHz.
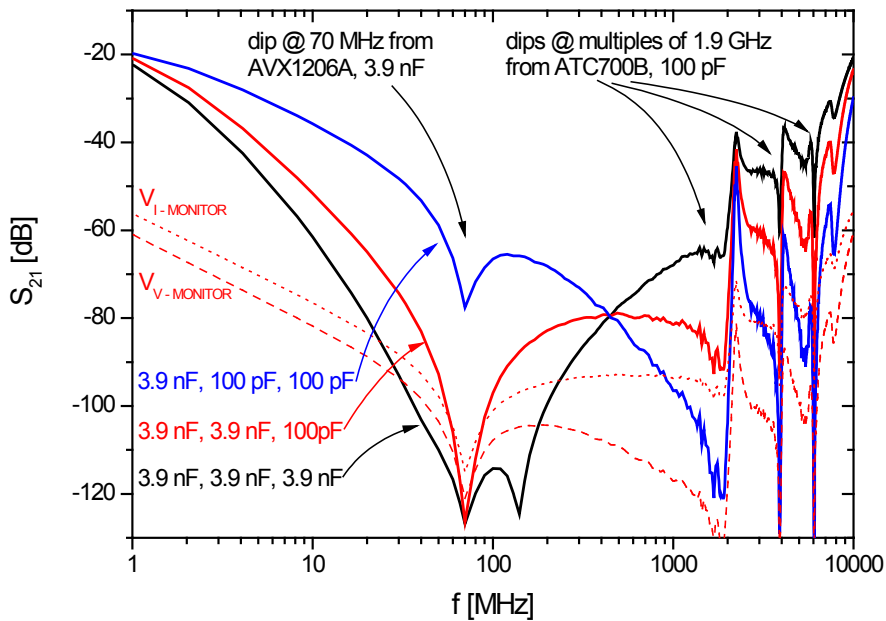
Fig. 2.35: *EMI rejection capabilities of the V_{BIAS} line with three combinations of capacitors with different values (solid lines) The S-parameters are calculated using the equivalent circuit for the AVX1206 3.9 nF capacitors and an S-parameter file for the ATC100B 100 pF capacitors. In the QM/FM, the (3.9 nF, 3.9 nF, 100 pF) (red solid line) combination is used because it provides broadband performance. For comparison, the EMI rejection over the $V_{I-MONITOR}$ and $V_{V-MONITOR}$ line is added to the plot.*
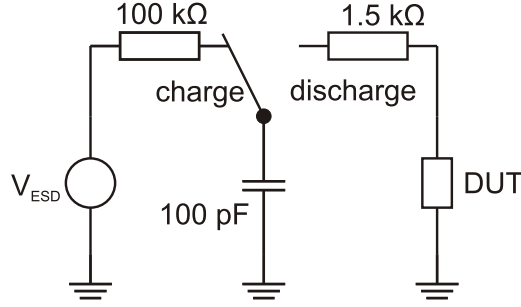
Fig. 2.36: *Human body ESD model. The 100 pF capacitor is charged to V_{ESD} and than discharged over the 1.5 kΩ resistor in series with the DUT.*

One 100 pF capacitor was placed directly parallel to the mixer chip as close as possible to the bias output in order to short circuit radiatively coupled E-fields at high frequencies.

The routing of the ESD-board layout could be optimized manually to gain space for three capacitors in the bias line. Because the resistors have a very small (0603) case size, R_S could be split into two 47 Ω resistors. This allowed three possible combinations for the bias-line:

$$
\begin{array}{lll}
3.9\,\text{nF}, & 3.9\,\text{nF}, & 3.9\,\text{nF} \\
3.9\,\text{nF}, & 3.9\,\text{nF}, & 100\,\text{pF} \\
3.9\,\text{nF}, & 100\,\text{pF}, & 100\,\text{pF}
\end{array}
$$

The transmission of the three filters is shown in Fig. 2.35. The filter with (3.9 nF, 3.9 nF, 100 pF) is chosen for the final design because it shows an excellent and flat EMI-rejection performance up to 1.9 GHz. The EMI-rejection of the R-C-R T-element filters of the $V_{V-MONITOR}$ and $V_{I-MONITOR}$ lines is plotted for comparison.

The ESD protection capabilities are evaluated using a SPICE model of the ESD filter and an implementation of the human body model (HBM). The human body model (Fig. 2.36) is a good choice for devices which are assembled manually. It uses a 100 pF capacitor and a 1.5 $k\Omega$ resistor to describe a characteristic discharge. SIS devices at room temperature and liquid helium temperature survive direct exposure to a discharge of up to 10 V [35] independently of operating temperature. Discharges of 15 V and more may destroy the SIS tunnel barrier. Fig. 2.37 shows the pulse form at the mixer chip contacts and at the SIS contact itself. The DC resistance of the entire mixer chip consists of the junction resistance $R_N = 15\ldots30\,\Omega$ and the RF blocking filter resistance, which has a value of about $R_B = 90\,\Omega$ at room temperature. The $V_{ESD} = 100\,V$ model pulse is reduced to a peak voltage of 0.064 V (factor $1.5\ 10^3$) when applied over the V_{BIAS} line and to 0.022 V (factor $4.6\ 10^3$) when applied over the $V_{V-MONITOR}$ line. With these values, it is possible to assign the mixer unit to class 1A ($V_{ESD} = 250\ldots500\,V$) of the HBM classification [36].
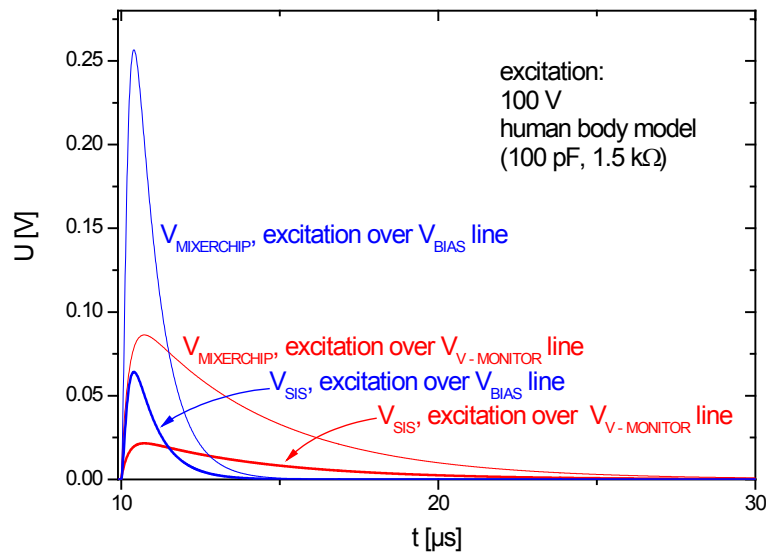
Fig. 2.37: *Response to a 100 V ESD pulse over the V_{BIAS} line (blue curves) and over the $V_{V-MONITOR}$ line (red curves). When the RF blocking filters are normal conducting, they add an additional 90 Ω resistance is series with the tunnel contact. This further decreases the pulse hight (thick lines).*

Chapter 3

Bias-T fabrication

The fabrication and assembly of the various parts and circuit boards of the bias-T are a very complex tasks involving manifold details. In order to reach the high performance and reliability criteria, a variety of very different materials have been used. Each material needs a specific treatment to become a space-qualifiable part of the mixer unit. Design flexibility in the tight HIFI schedule and quality control have been achieved by keeping as many fabrication steps as possible in house. Among the most critical tasks are the cut out of the TMM10 and RT/Duroid6002 boards, the gluing of the boards into the housing (Ablefilm 5025E) and gluing of the components (EPO-TEK H20E). The most critical and demanding manual work is the application of solder joints of the SMA cable and the SMA jack.

The bias-T has to comply with space qualification standards and has to survive the harsh conditions during test, launch and operation. The manufacturing know-how had to be acquired by tests and experiments. The assistance by ESA/ECSS , by JPL (ESD-training), SRON (J. Evers (quality assurance) and common parts procurement) was very helpful to finally succeed in designing and fabricating the mixer unit.

In this section, details of the fabrication processes, which have been developed within this thesis, are provided. The focus is placed on non-standard solutions, which helped to maintain the high performance standards and assure in the same time high reliability and quality.

The milling of the IF circuit boards, the manufacturing of both the SMA cable and the SMA jack assemblies and the gluing of all components using EPO-TEK H20E have been carried out by the author for all mixer unit models (DM, QMs, FMs FSs).

3.1 Bias-T box

The bias-T box is a filigree aluminum construction designed by M. Schultz (see Fig. 2.2). The shape is milled by the in-house workshop on a five-axis CNC machine. The surface is electroplated with $\approx 1\,\mu m$ Au plating on a Ni buffer layer. The Au plaiting is required as surface finish for the gluing of the TMM10 and RT/Duroid6002 boards with Ablefilm 5025E. The Alumina board with the ESD filter is mounted in a separate compartment by CuBe clamps, which are integrated in the box walls. The box covers are EMI leak proof by the use of a tight fit, a protruding inner edge and many screws with a small spacing. The L-shaped box arrangement optimally uses the remaining place in the small mixer unit envelope. The ESD box can be separated from the bias-T box including the ESD board and thus enables parallel fabrication of both sections. This highly increased the flexibility of the fabrication schedule. (The fabrication of the Alumina substrate including the integration of the components was outsourced to Hymec, NL.)

3.2 Printed Circuit Boards

The first IF filter boards for the DM have been manufactured by the author using a standard etch process similar to that used for the directional coupler described in section 6.6.2. The masks have been obtained by a 4:1 reprography to a AGFA Copyproof CPN/CPF 0.10 film pair. The AGFA reprography system contains three instruments: Repromaster 2200 II (exposure), Copyproof CP38 (developer) and Copyproof WD37 (dryer). The board outline was cut manually with a small saw or a scalpel.

In order to accelerate the design cycle, the etch process was replaced by a fast prototyping process using a LPKF milling machine. The circuit pattern and the board outline can be milled without removing the substrate material from the machine. This gives a very good alignment between board contour and circuit pattern and is much faster than the etching process.

3.2.1 Quality control of the wet etching process of the QM/FM boards by Printech

For the final version, used in the QM, FM and FS, the boards have been etched and gold plated ($1\,\mu m$ Au) by Printech (UK) because the mask quality obtained using the AGFA reprography system was not sufficient for QM/FM production and because the gold plating process could not be done in house. Again the gold plating serves as finish for the gluing with Ablefilm 5025E into the housing, for the gluing of components to the board and for a corrosion-free wire bond contact area.
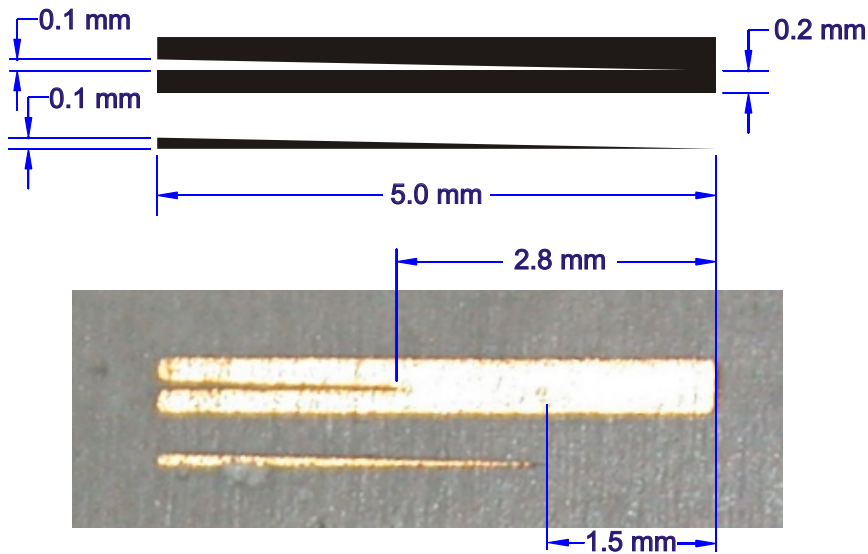
Fig. 3.1: *The quality of the printed circuit boards, manufactured by Printech (UK), can be evaluated by means of a control structure. With the given dimensions, undercutting is amplified 100 times because it acts on both sides of the structure. Thus, the etched structure below, taken from a RT/Duroid6002 board shows a mask induced line broadening of 28 μm and an effective undercutting of 15 μm. (The total undercutting is then 28 μm + 15 μm = 43 μm.) As could be seen by checking other structures, this high etch quality is distributed uniformly over the whole area on both TMM10 and RT/Duroid6002 boards.*

In order to monitor the precision of the Printech etch process, a special structure has been added to the board design, which can be seen in Fig. 3.1. It shows the effect of undercutting "amplified" by a factor of 100 ($= 2\frac{5.0\,mm}{0.1\,mm}$) by means of the spiky triangular structure. Likewise, any line broadening due to the mask or the photo resist is "amplified" in the structure which forms a negative triangle. In this way, any tolerances of the fabrication process can be easily measured along the long side of the structure. After delivery and quality control, the large patterned substrate sheets have been cut out with the LPKF system in house.

3.2.2 The milling machine, tools and machining parameters

The milling machine Protomat C100/HF, which is depicted in Fig. 3.2, has a resolution of 7.9 μm per step and an 340 mm by 200 mm working area, which makes it very suitable for the processing of substrate materials [37]. High rotation speeds of up to 100000 rpm make it possible to use milling tools with a very small diameter.

The substrate materials TMM10 and RT/Duroid6002 have very different mechanical properties: TMM10 is hard and brittle, with an elastic modulus of
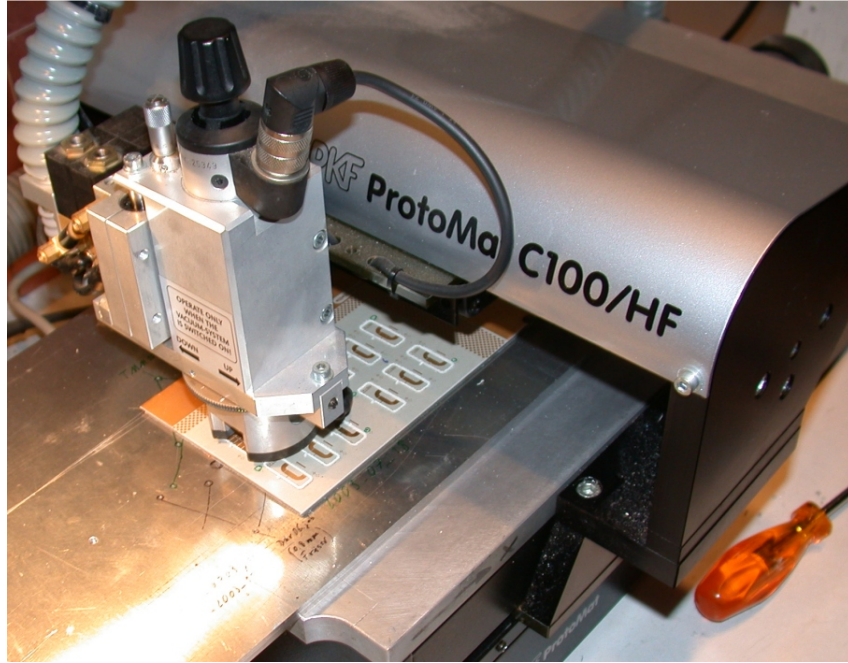
Fig. 3.2: *The milling machine Protomat C100/HF (LPKF) during the cut out of the RT/Duroid6002 boards for the QM/FM mixer units. For alignment purposes, the substrate is glued to a carrier substrate and aligned to the machine via an Aluminum board.*

16.5 GPa, while RT/Duroid6002 is very soft and can be (inelastically) bent with an elastic modulus of just 0.8 GPa. Thus, different tools and machining parameters are needed in order to obtain clear and smooth cutting edges.

For the test circuits, the circuit pattern is obtained by removing the copper with surface milling tools. This is done even before the board is cut out from the substrate sheet. Here the diameter of the surface milling tools determines the machining parameters rather then the substrate properties. The used tools and machining parameters are presented in appendix A.1.

For the QM/FM, the circuit development was entirely based on milled test circuits, although the final circuit patterns are fabricated by etching. Thus, a small engraving depth had to be maintained in order to obtain similar electric results of etched and milled circuits. The substrates are fixed with dowel pins in lateral direction. Unfortunately, little can be done to avoid the uneven distance of the substrate to the machine. Especially the RT/Duroid6002 substrate tends to deform inelastically under weak forces. Thus, it is difficult to establish a surface milling process which removes only a very thin layer, ideally $< 0.05 \ldots 0.1 \, mm$ of the substrate surface. A special procedure and special tooling has been developed for this purpose, which is summarized in appendix A.2.

3.2.3 Cutting of the QM and FM boards
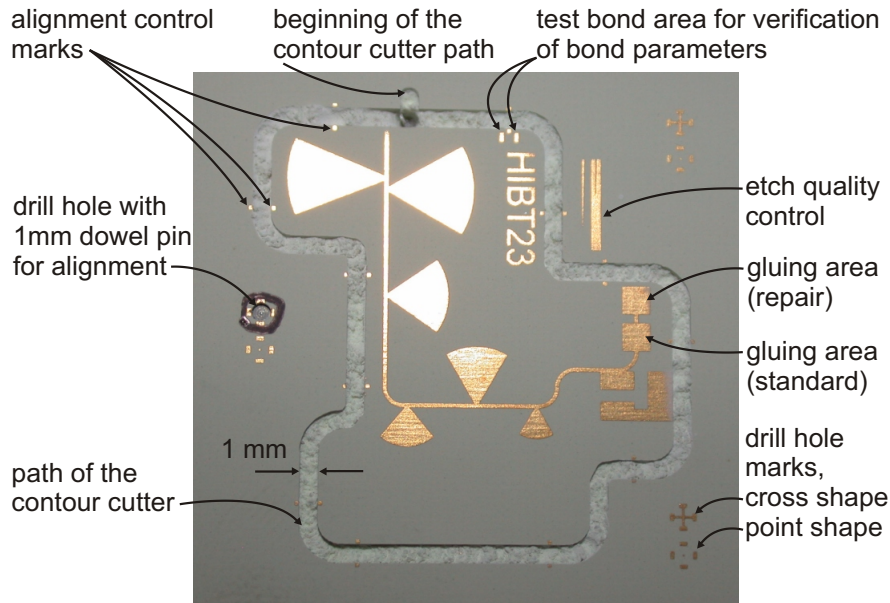
Fig. 3.3: *TMM10 board after cut out with a 1.0 mm contour cutter. The board is still fixed to the carrier substrate by wax. The photo illustrates different features of the Cu pattern and the milling process.*

The test boards could be cut out except for two small ligaments which assure mechanical contact and fixation of the board during the whole process. Afterwards, the board could be separated from the substrate sheet by braking the ligaments. The remains of the ligaments have to be removed by careful work with sandpaper. For the QM/FM boards, the ligament technique could not be applied because of the risk of a hidden crack in the substrate.

For the test boards, the alignment between the PCB outline and the circuit pattern is excellent because both are milled in subsequent steps without removing the substrate from the machine. For the QM/FM boards, a similar alignment quality was achieved with marks for 1 mm drill holes on the circuit pattern, as can be seen in Fig. 3.3.

The method developed for the HIFI IF boards implements both a good alignment and an entire cut out without the use of ligaments. The method is described in appendix A.3.

3.2.4 TMM10 and RT/Duroid6002 board gluing with Ablefilm 5025E

The gluing technology described here was developed by T. Tils and partly by the author who took part on the identification of the pressure parameter and developed and fabricated the soft intermediate layer of the plungers.

plunger for
RT/Duroid6002 board

plunger for
TMM10 board

temperature
sensor

plunger
soft layer

bias-T box

heated
mount

heaters
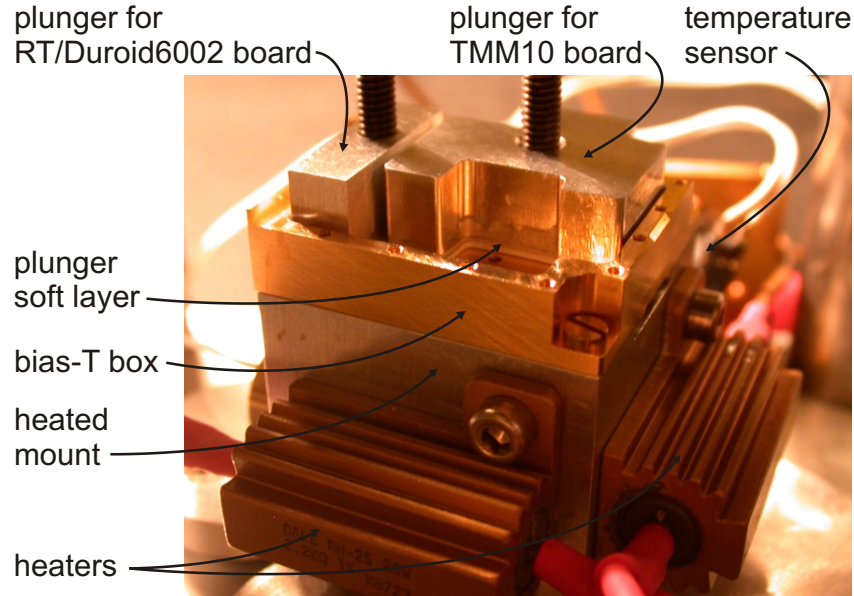
Fig. 3.4: *IF circuit boards being glued to the bias-T box. The photo shows the bias-T box fixed to the heatable mount. The boards are pressed down with a well defined force by two plungers, while the conducting, silver loaded epoxy film, Ablefilm 5025E, is cured at 127°C.*

Both TMM10 and RT/Duroid6002 circuit boards are glued to the bias-T box with Ablefilm 5025E, a conductive, silver loaded, adhesive epoxy film with a thickness of $5\,\mu m$ [38]. Pieces of Ablefilm are cut out with a punching tool, which repeats the form of the boards, but with 0.1 mm reduced size at all boundings. The film and the boards are clamped to the box and adjusted with dedicated spacers (stainless steel). The boards are pressed down with a well defined force during the gluing process with aluminum plungers, having a similar shape as the boards. An intermediate layer of soft, unplated RT/Duroid6002 with the exact board dimensions uniformly distributes the pressure over the board area. The pressure is applied over a small lever with dedicated weights. This assures a repeatable and defined pressure level over the whole gluing process. The bias-T box is screwed to a heatable mount, which is shown in Fig. 3.4. The whole unit (mount and press) is operated in an evacuated glass container. The adhesive film is cured with $T = 127°C$ for 120 min and an additional 30 min warm up and cool down phases.

The correct pressure was determined by gluing boards to glass slides. After the curing process, the samples can be inspected from the backside with a microscope. The film shows inclusions (air or vacuum) if the pressure is to low and disruptions if the film is squeezed by excessive pressure.
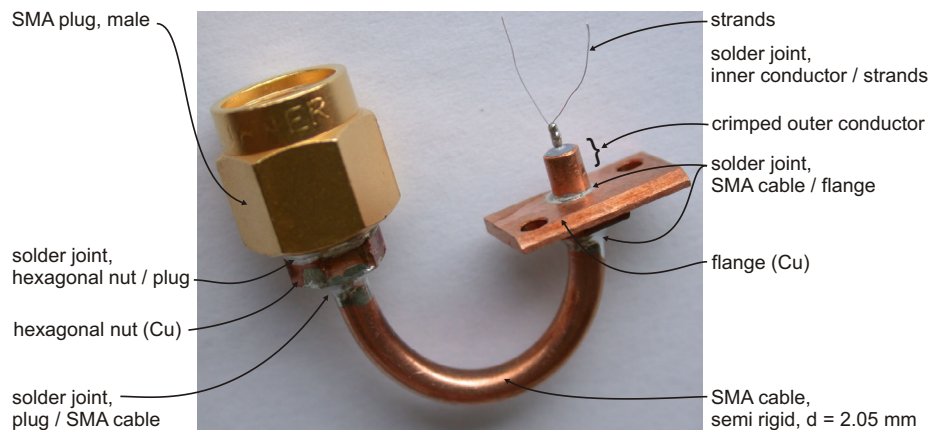
Fig. 3.5: *SMA cable ready to be mounted to the bias-T box. The photo shows some of the feature of the SMA cable construction.*

3.3 SMA cable manufacturing

An average of 6 to 8 hours net working time is needed to manufacture a single SMA cable with all solder connections to the SMA plug, the copper flange and the strands (Fig. 3.5). In some very critical steps, the quality of the joint is very dependant on the right timing of the (manual) solder process. Unfortunately, some steps can not be repeated and the cable must be refused when the quality does not satisfy cryogenic space application standards. In order to fabricate enough high quality cables in a reasonable time, a whole batch is manufactured in parallel. The yield for the QM, FM and FS batches was around 60%.

The development of the soldering procedure [39] included several cycles of manufacturing, performance tests and environmental reliability tests. Parallel to this very complex and time consuming task, a collection of some simple, but very helpful tools has been developed. The ESA/ECSS manuals for the manufacturing of coaxial cables [40] and for manual high reliability soldering [41] could provide helpful information about the thermal preconditioning of the cable (after confection and bending) and about the use of different kinds of solder.

3.3.1 SMA plug with hexagonal nut

A usual SMA plug of the "Huber+Suhner" SMA-1-110 series for semi-rigid SMA cables is delivered preassembled. This preassembled plug contains a silicon rubber gasket, which is not allowed in space applications because of possible outgassing, which would result in a contamination of other parts (e.g., cryostat, optics). Unfortunately, it is not possible to remove the gasket without damaging the preassembled nut. Thus, the SMA plug had to be procured completely disassembled and the nut of the plug had to be preassembled
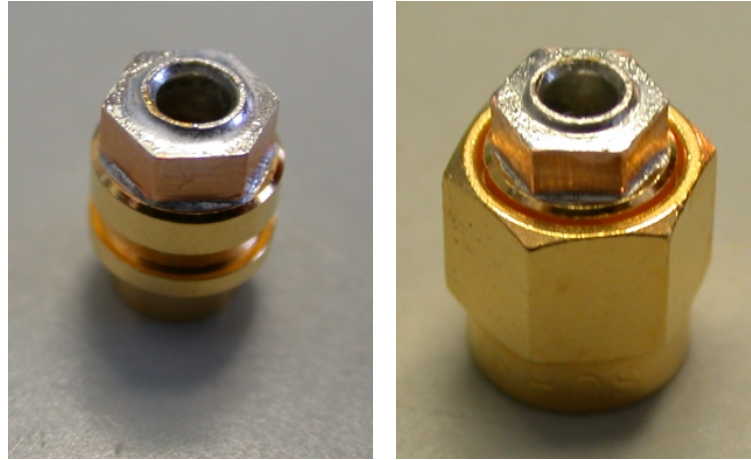
Fig. 3.6: *Left: Body of the SMA plug with hexagonal nut (Cu). The nut is soldered to the body prior to the assembly with the SMA nut.*
Right: SMA plug assembly completed.

without the gasket. The special tooling for this task was developed together with the KOSMA in house workshop.

In an QM test run, it was found that the bias-T box had moved 0.2 mm from its original position at the bracket after an extensive thermal cycling test, although the box was tightened with three stainless steel M2 screws, which had been torqued with torque levels for cryogenic applications (35 Nm). This intolerable displacement was found to originate from a high mechanical tension, which arises when the SMA plug is torqued to the mixer block. To prevent the cable from being distorted while being torqued to the mixer block, a hexagonal nut (Cu) was soldered to the back end of the SMA plug (Fig. 3.6). The cable, which is soldered to the plug later, has to have a particular orientation relative to this nut in order the nut be accessible with a small screw-wrench during the torque process. With the screw-wrench, it is possible to compensate for the torque forces and prevent the cable from torsion. Thus, the bias-T box can be mounted entirely stress free to the mixer bracket.

3.3.2   The flange

The flange is a very stable and EMI proof way to precisely mount the SMA cable to the bias-T box. It saves the weight and the space of an additional connector. In order to assure a precise orientation, the cable and the flange are screwed (and torqued) to the tool, which is depicted in Fig. 3.7. The flange is mounted to an epoxy PCB with low heat capacity and conductivity. With two movable parts, the flange can be aligned and the SMA cable length behind the flange can be controlled. After the alignment, the flange is torqued and the movable parts (metal) are removed to minimize the heat
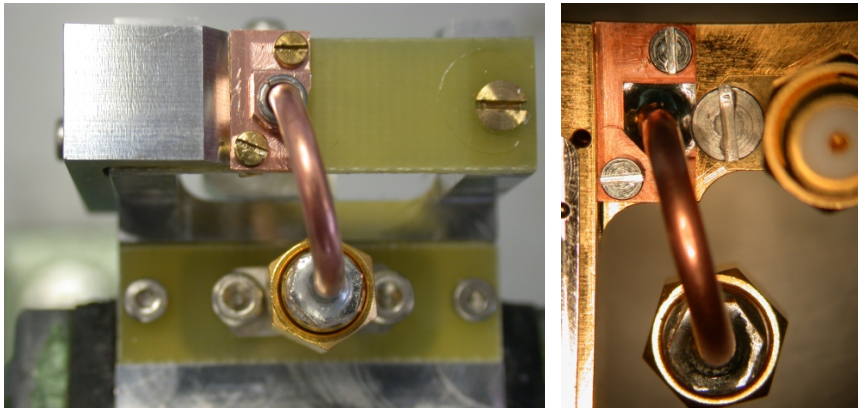
Fig. 3.7: *Left: Soldering the flange to the SMA cable. The flange position is controlled with an alignment tool, which is optimized for low heat conductivity in order to afford a short solder time.*
Right: For comparison, a view of the flange assembled to the bias-T box.

capacity and conductivity. This allows a short solder time, which is necessary to avoid a damage of the SMA cable dielectric. (Compare section 3.3.3.)

3.3.3 Crimping the cable

The short (32 mm) SMA cable is subjected to extreme heat when the flange and even more when the SMA plug is soldered to the cable, although everything is done to reduce the soldering time (flange: $\approx 9\,s$, plug: $\approx 15\,s$) and the heat input to the cable. The high temperatures cause the dielectric (PTFE) of the cable to flow and to partially relieve the pressure against the outer conductor. Thus, the short length of the cable and the reduced friction may cause the dielectric to move relatively to the tube when strong forces are applied. Such strong forces may occur, for instance, when the dielectric of the plug is pressed over the central pin and into the nut of the SMA plug. Such a movement can be safely averted by slightly modifying the shape of the outer conductor at the flange side of the cable. This can be done with the tool shown in Fig. 3.8. The outermost ending of the cable is pressed in the mold. The solder joint of the flange is not affected by this deformation because a spacer keeps a 1.0 mm distance between the flange and the crimping region.

A 3D-solver simulation revealed that the deformation even slightly improves the transmission of the SMA cable to microstrip transition in the 4-8 GHz range. This may be explained by a slight increase of the capacitance in the crimping region, which partly compensates the inductive part of the transition.
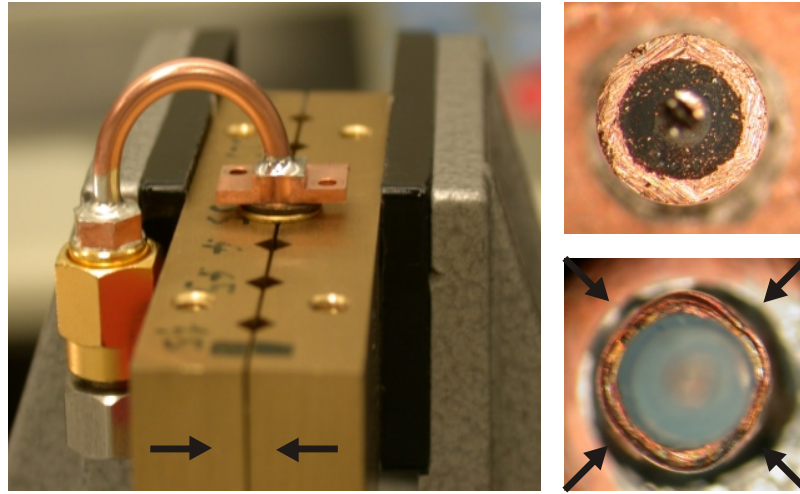
Fig. 3.8: *Left: Crimping tool. The tool is used to obtain a slight deformation at the ending of the SMA cable. This deformation fixes the dielectric of the cable.*
Right: SMA cable before and after application of the tool.

3.3.4 Soldering the strands

Although the inner conductor of the SMA cable is placed directly over the microstrip line, this can not assure DC contact because all materials are subjected to thermal shrink when the mixer unit is cooled down to 2.8 K operating temperature. A reliable and flexible connection for the bias current is provided by a single strand of a Habia wire with AWG 34 (American Wire Gauge), which is wound around the inner conductor. To facilitate the soldering of the strand, a clamping mechanism, which is explained in Fig. 3.9, is used. The tool allows to fix the strand at the inner conductor close to the dielectric of the SMA cable, which results in a good high frequency performance of the connection (compare section 2.7.8). The clamp fixes the strand without disturbing the free flow of the solder in the vicinity of the strand. Once the strand is clamped, it can be tightened with the aid of an auxiliary wire and a defined weight ($\approx 20\,g$). Then the eutectic solder paste is distributed and the strand is soldered to the inner conductor. After a final clean and inspection, the cable is ready to be mounted to the bias-T box.

3.4 The SMA jack

The SMA jack is connected to the microstrip line via a flexible $25\,\mu m$ CuBe strip. The strip is preformed putting in a small kink to gain additional flexibility, which is necessary to withstand thermal contraction during cool down. This step-like shape is obtained by clamping the strip between two molds, which are moved against each other, as can be seen in Fig. 3.10.
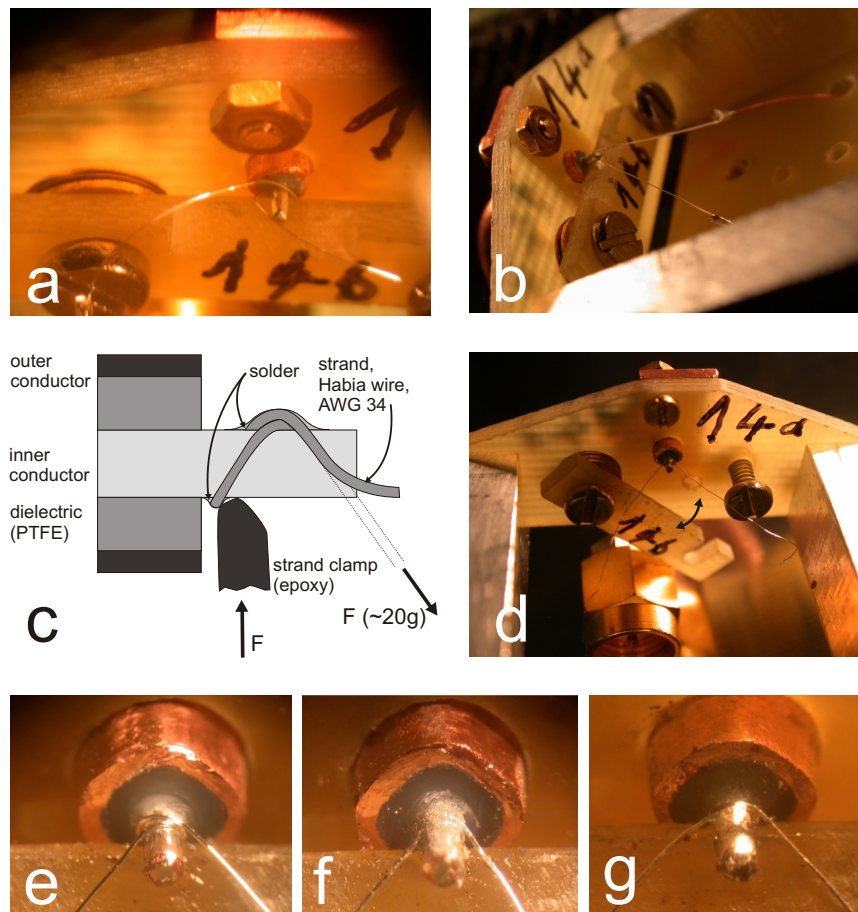
Fig. 3.9: *Soldering procedure for the strand.*
a) The strand is wound around the inner conductor of the SMA cable and fixed with a clamp (averts slip off).
b) The strand is tightened by an auxiliary wire via dedicated holes and a 20 g weight (not visible).
c) The strand clamp fixes the thin wire without disturbing the free flow of solder and flux by means of the special form.
d) After the soldering process, the auxiliary wire is desoldered and the clamp is opened for removal of the cable.
e)-g) Soldering process of the strand:
e) Strand fixed in the correct position around the inner conductor.
f) colloidal solver paste (eutectic solder Sn 96.5%, Ag 3.5%) is distributed in the right quantity.
g) After the soldering process

The SMA jack is mounted to the tool shown in Fig. 3.11 g) whose parts are made of fibre-glass reinforced epoxy in order to achieve a good thermal isolation of all soldered parts. The tool allows to adjust the CuBe strip to the slit in the inner conductor. The slit is cut in the workshop with a 67 μm blade, pretinned and cleaned as shown in the sequence in Fig. 3.11 a)-d). The strip is trimmed, adjusted in the slit and soldered with a defined quantity of solder from both sides.

CuBe-strip, w = 1.8 mm, t = 0.025 mm

h = 0.2 mm
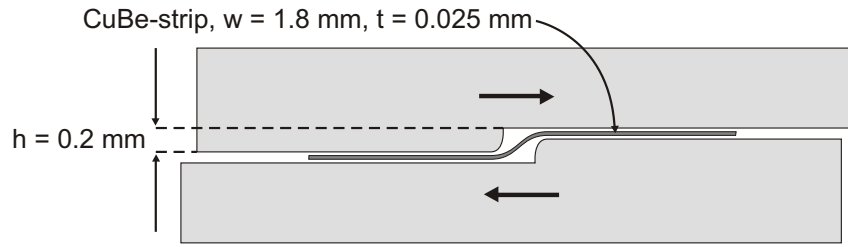
Fig. 3.10: *CuBe-foil strip forming process. The foil is clamped between two Aluminum molds. While the molds are moved against each other, the step-like feature is formed. The sharpness of the step only depends on the radii of the steps in the Aluminum forms.*
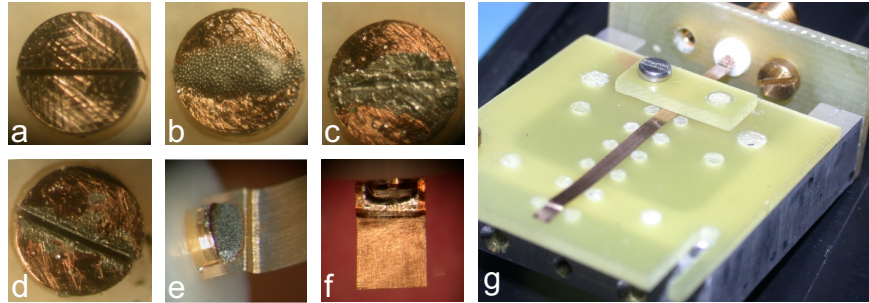
Fig. 3.11: *Soldering process of the CuBe-foil to the SMA jack:*
a) Slit (w ≈ 70 μm) in the inner conductor of the SMA jack.
b) Solder paste is distributed for pretinning process.
c) Pretinning of the slit for good wetting of the insight of the slit.
d) Solder from pretinning partly removed for isertion of preformed CuBe-strip.
e) CuBe-strip adjusted in the slit. Eutectic solder paste distributed on top and below.
f) After the solder process, the CuBe-strip and the SMA jack are unmounted and the strip is cut to the correct length.
g) Adjustment tool for soldering of the CuBe-strip to the SMA jack. The tool is designed to minimize solder time by using materials with low heat conductance.

3.5   Gluing components with EPO-TEK H20E

Fig. 3.12 shows the bias-T and filter section with the four interconnections glued with EPO-TEK H20E. A fifth small test quantity is added to control the mechanical and electrical properties of the glue after the curing on the hotplate. EPO-TEK H20E is a silver loaded, two component (1:1), epoxy glue with a soft, smooth consistency. The main advantage is the high reliability and the low curing temperature (85°C, 120 min), which is necessary to not to weaken the wire bonds and other materials [42].

Unfortunately, it was not possible to apply all gluing connections at once because the mount used for the wire bonding at Hymec (NL) could
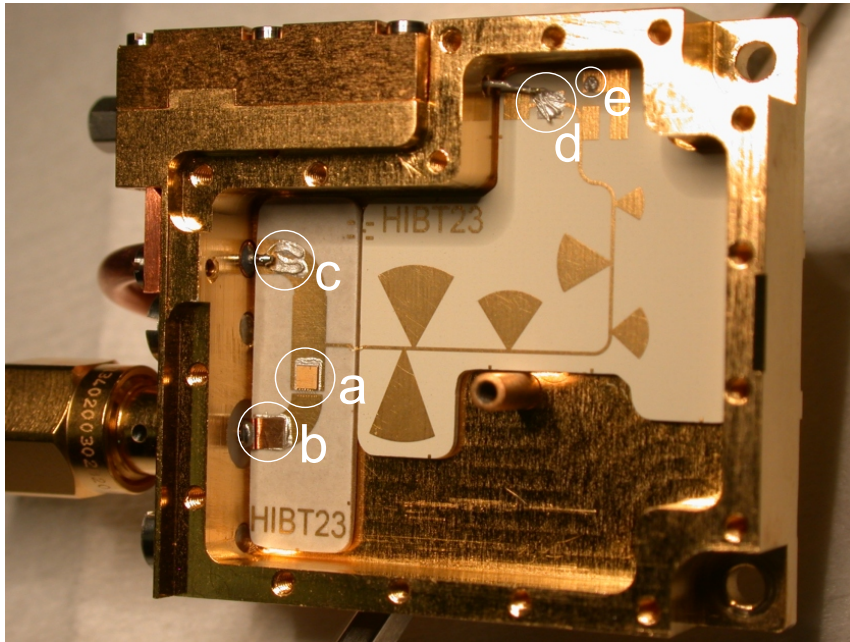
Fig. 3.12: *Open Bias-T box with marked gluing areas. In a first process, the ATC capacitor is glued. Then all wire bonds are applied. In a second gluing process, the strip of the SMA jack, the strands of the SMA cable and the connection to the ESD box are glued.*

only be used without SMA cable. Thus, the ATC capacitor had to be glued first, then all bond wires are applied at Hymec (bonds between capacitor and RT/Duroid6002 board and bonds between TMM10 and RT/Duroid6002 board). Subsequently the remaining three parts are glued to the PCBs. This has the further drawback that extreme care has to be taken to avoid any contact with the bond wires during the whole gluing procedure to not to damage the bond wires.

For all adhesive bonds, special care had to be taken to assure a proper wetting of all surfaces. This can be done by slightly moving the parts relatively to each other or by prewetting of both surfaces, as is done in case of the CuBe-strip of the SMA jack.

3.5.1   Gluing the ATC capacitor

The glue which holds the ATC capacitor is distributed manually with a small polyethylene stick uniformly over an area slightly larger than the capacitor dimensions. Excessive glue can be spread on the microstrip line until the right thickness of the glue is obtained. The right amount of glue has been determined by several tests on a test board, which was fabricated on the same RT/Duroid6002 substrate as the QM and FM boards (Fig. 3.13 a), 2-4). The stability of the adhesive bond was investigated by destructive testing.
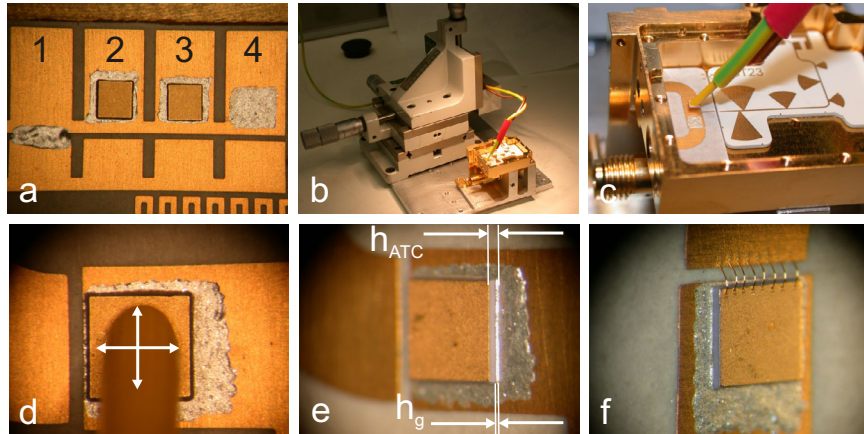
Fig. 3.13: *a) Test board to identify the right amount of glue for the ATC capacitor. (Strength determined by destructive testing.)*
b-c) The micro vacuum tweezers mounted to an XYZ-stage.
d) The capacitor hold by the tweezers directly over the gluing area. Accurate wetting of the capacitor is achieved by slightly moving the capacitor in the glue.
e) The wetting is controlled under the microscope. Complete wetting along the capacitor border is required. Excessive glue at the border is not allowed $(h_g/h_{ATC} \leq 1/2)$.
f) ATC capacitor after curing and application of the wire bonds.

Fig. 3.13 b) and c) show the micro vacuum tweezers which are mounted to an XYZ-stage. The tweezers are equipped with a tiny (0.9 mm) and soft end tube, which is cut under 45°. The tube is guided by a flexible metallic arm, which gives additional adjustment possibilities and allows to build up a constant pressure in Z-direction.

The capacitor is picked up, aligned with the microstrip line and placed into the glue. By multiple, slight movements in X and Y-direction and under a weak force in Z-direction, the capacitor bottom electrode is wetted with glue (Fig. 3.13 d)). The wetting process is controlled under the microscope. A complete wetting is required, but without excessive glue on the edges of the capacitor ($h_g/h_{ATC} \leq 1/2$, see Fig. 3.13 e)). If this result could not be obtained, the capacitor had to be removed and both the capacitor and the entire housing had to be cleaned in order to completely remake the gluing. After the curing, the top electrode of the capacitor is contacted with Au wire bonds at the wedge bond facility of Hymec (NL) (Fig. 3.13 e)).

3.5.2 Gluing the strands of the SMA cable

Before the SMA cable flange can be screwed to the bias-T box, the strands have to be carefully passed through the hole in the box without being damaged by touching the box walls or the PCB. When the flange is fixed, the strands are bend in an U-shape with the outer path close to the microstrip edge in
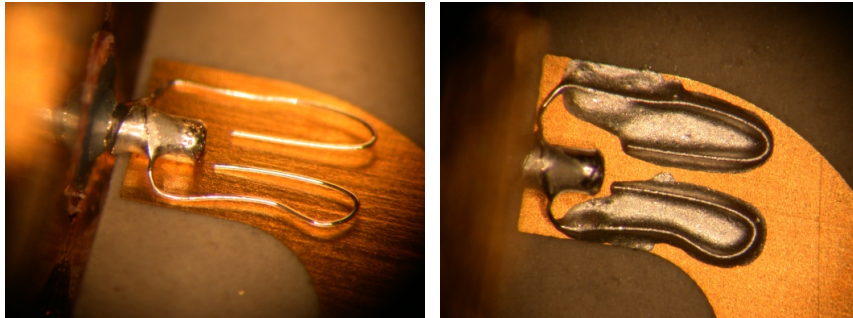
Fig. 3.14: *Left: Strands are preformed in an U-shape. The strands should be as close as possible to the microstrip in the gluing area.*
Right: Strands after application of a small amount of EPO-TEK H20E.

order to improve the RF-performance (compare section 2.7.8). Furthermore, the strands should be arranged as close as possible to the microstrip line over the entire length except from the part close to the inner conductor, which has to have sufficient slack to tolerate any thermal contraction and any vibrational stress. Fig. 3.14 a) shows the strand right before being entirely covered by a small amount of glue (Fig. 3.14 b)).

3.5.3   Gluing the CuBe-strip of the SMA jack

Unlike the ATC capacitor, the CuBe-strip of the SMA jack can not be moved when it is placed to its final location. Thus, another way to achieve the wetting of the entire surface must be chosen. First the strips bottom surface is cleaned from any oxide and roughened without damaging the preform of the strip (Fig. 3.15 a)). The clean surface is wetted with a thin layer of EPO-TEK H20E (Fig. 3.15 b)). The microstrip is likewise coated with glue and finally the SMA jack is inserted in its mounting hole and tightened with screws. The step-like preform of the strip must be kept free from any glue in order to maintain flexibility of the junction. While the glue is being cured the CuBe strip is slightly pressed down to the microstrip with a guided needle in order to achieve close contact between the strip and the Au-plated microstrip. This way, excessive glue is pressed out from under the CuBe strip unto the microstrip line (compare Fig. 3.15 d)).

3.5.4   Gluing the interconnecting wire between ESD box and bias-T box

Prior to mounting the SMA cable and the SMA jack, the ESD box is attached to the bias-T box. The Habia wire, which connects the ESD board with the bias-T compartment, is threaded through a build-in tube to the bias-T box. The ending of the wire is untwisted and all strands are spread over the gluing
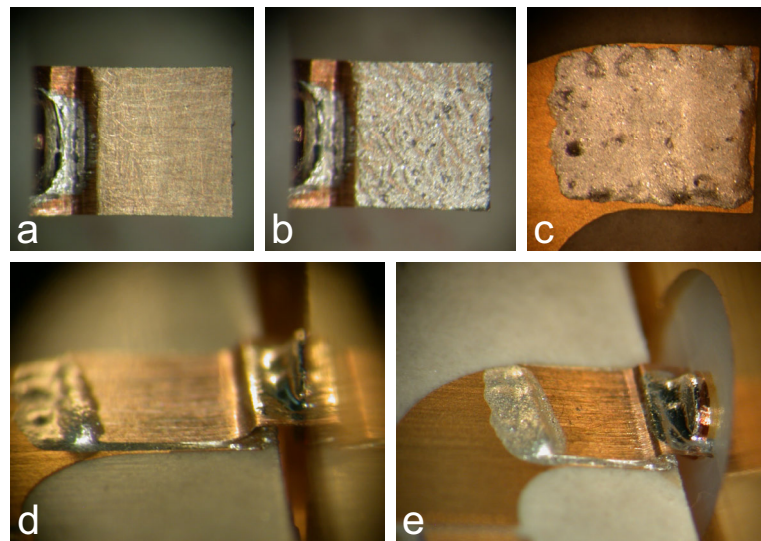
Fig. 3.15: *Gluing of the CuBe strip of the SMA jack.*
a) The CuBe-strip is roughened and cleaned with sand paper without deformation of the strips preform.
b) The strip is wetted with a small amount of glue.
c) The microstrip is wetted in the gluing area.
d) After insertion of the SMA jack to its hole and placing of the CuBe-strip on the microstrip line: The step-like structure has to be free of glue in order to maintain mechanical flexibility.
e) View of the complete CuBe-strip and the SMA jack.
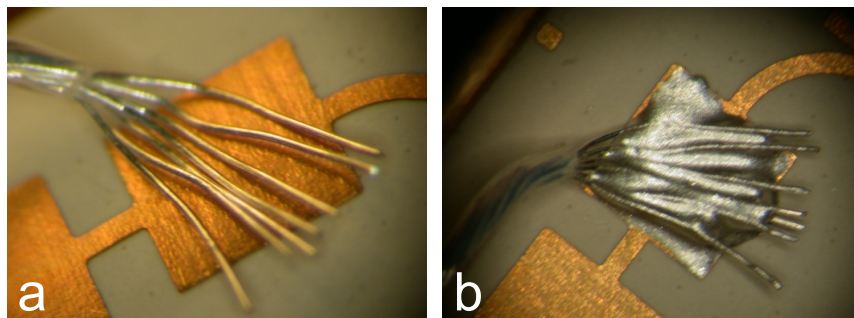
Fig. 3.16: *Gluing of the connection to the ESD box.*
Right: The strands of the wire are distributed over the pad.
Left: The glue has to cover all strands.

pad as close as possible to the surface in order to achieve a stable bond. The glue is distributed according to Fig. 3.16 coating all strands and the complete pad.

Chapter 4

IF performance measurements

4.1 Bias-T signal path transmission

In the following chapter, three measurement methods are presented to characterize the IF performance of the mixer units for band 2.

The first method is the measurement of S-parameters of the bias-T (separated from the mixer block) by means of a vector network analyzer at room temperature. To verify these results, the transmission of the bias-T is further checked by noise temperature measurements of the IF chain with and without the bias-T. Unlike the S-parameter measurements, this method can evaluate the transmission at the operating temperature of the device (2.8-4.2 K). The third method uses the SIS-junction itself as a noise source (after the integration of the bias-T in the mixer unit). The shot noise generated by a DC current flowing (tunneling) through the barrier is used for these measurements. Thus, the complete IF path from the junction to the IF output of the mixer unit can be checked for any unwanted features.

Fig. 4.1 summarizes the performance in the three major design stages of the bias-T. The DM performance is mainly reduced by the use of substrate material with a higher dissipation factor and a blocking capacitor in multilayer technology (compare section 2.7.10). In the QM design, the suppression of the box resonance (section 2.7.7) and the redesign of the SMA cable to microstrip transition likewise contribute to an improvement in comparison with the DM design.

The slightly decreased performance of the QM in comparison with the FM is only due to the incorrect position of the inner conductor of the SMA cable directly over the microstrip line. This non-conformance was corrected for the FM and FS mixer units.

Because the IF signal, generated by the SIS-junction, is first passing through the bias-T before it is amplified, every attenuation in the bias-T strongly
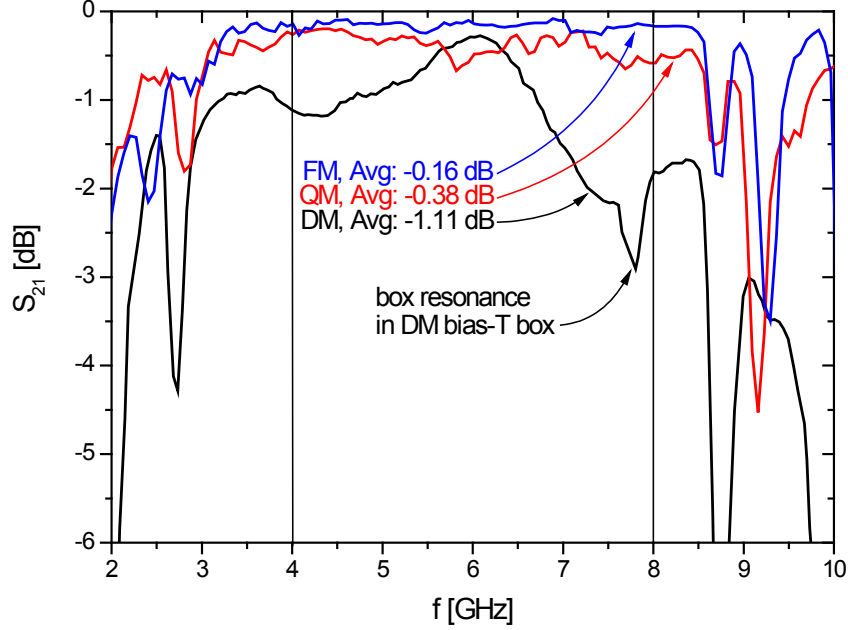
Fig. 4.1: *Network analyzer measurements of the transmission of the bias-T in different design stages. The small difference between FM and QM are due to an incorrect placement of the SMA cable in the QM.*

bias-T model	G_{bias-T} [dB]	Noise Contribution to T_{SYS} [K]
DM	-1.11	7.25
QM1 (HMBT4)	-0.376	2.25
FM1 (HMBT7)	-0.160	0.94

Tab. 4.1: *Contribution of the bias-T to the receiver noise temperature in different design stages. The noise temperatures are calculated for $T_{IF} = 10K$ and $G_{MIX} = -4\,dB$ (QM-mixer at $f_{LO} = 666\,GHz$)*

contributes to the system noise temperature:

$$T_{SYS} = T_{MIX} + \frac{T_{IF}}{G_{MIX}G_{bias-T}} \tag{4.1}$$

where contributions of the optics are not considered. For the HIFI signal chain, an IF noise temperature $T_{IF} \approx 10\,K$ can be assumed. If the mixer gain is known, the contribution of the bias-T to the overall noise temperature can be calculated:

$$T_{bias-T} = \frac{T_{IF}}{G_{MIX}} \frac{1}{G_{bias-T} - 1} \tag{4.2}$$

For Tab. 4.1, this contribution is calculated for a mixer gain of $G_{MIX} = -4\,dB$ (which corresponds to the mixer gain of QM1 at $f_{LO} = 666\,GHz$). The additional noise temperature due to the bias-T could be reduced below $1\,K$ for the FM mixer units.

4.1.1   S-parameter measurements with a network analyzer
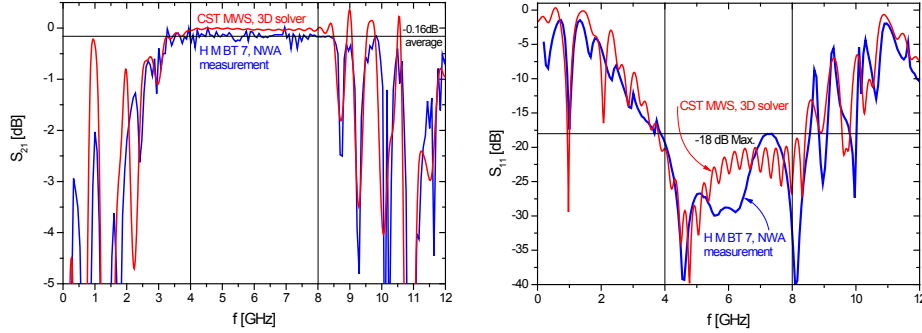
Fig. 4.2: *Transmission and reflection of the FM bias-T. Measured S-parameters in very good agreement with simulation results.*

A straight forward way to characterize the signal transmission performance of the bias-T is to measure S-parameters with a network analyzer. Fig. 4.2 shows measurements of the transmission and reflection obtained with a HP 8719A vector network analyzer. The calibration of the transmission measurement can be done with an approximate accuracy of $\Delta S_{21} \approx 0.1\,dB$. Unfortunately, the quality of the measurement is reduced by small spikes caused by standing waves in the long cables connecting the network analyzer and the bias-T. This spiky structure can not be completely removed by calibration because the inevitable bending of the SMA cables introduces phase differences between measurement and calibration.

The losses in the bias-T can be broken down as follows: The losses due to signal reflection are $1 - S_{11} \geq -0.07\,dB$, which corresponds to a maximum reflection $S_{11} \leq -18\,dB$. The remainder can be attributed to ohmic losses in the SMA cable and in the printed circuit boards in the bias-T box. The SMA cable between mixer block and bias-T box has a length of L=32 mm and contributes $-0.04\,dB \ldots -0.06\,dB$ in the 4-8 GHz range [31]. Radiative losses on the RT/Duroid6002 and TMM10 board are reduced by the pillar to a very low value (compare section 2.7.7).

In the CST MWS simulations (which are shown in comparison with the measurements), only dielectric losses due to the non-zero dissipation factor of the substrate material are reproduced. Losses due to the final conductance of the Cu-layer are not considered because the circuit structure is implemented using a PEC layer (perfectly electrically conducting). Furthermore, the losses in the SMA cable are not included in the simulation.

When the losses in the dielectrics and the conductors are reduced by cooling down the whole bias-T to cryogenic temperatures (77 K, liquid N_2), the measured S-parameters and the simulation converge within the measurement accuracy. For performance characterization at operating temperature (4.2K, liquid He), other methods have been used, which are presented in the next sections.

4.1.2 The IF chain for the measurements of the mixer units for band 2

The IF-chain, which was used for heterodyne measurements as well as for performance measurements of the bias-T, consists of a cryogenic chain followed by a chain at room temperature. Both chains are connected via a stainless steel SMA cable, which guides the signal from the 4 K-stage to the output connector of the dewar, and a flexible SMA cable, which connects the dewar with the IF-chain at room temperature.

The cryogenic IF chain
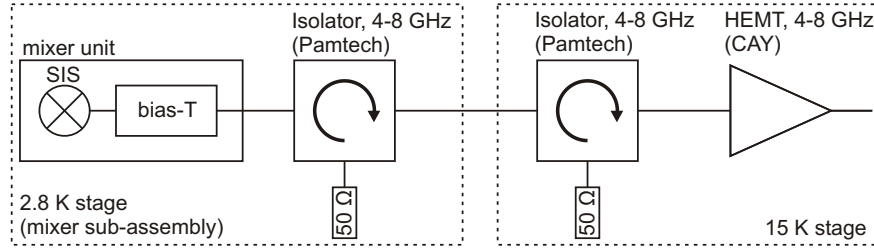
Fig. 4.3: *The complete cryogenic IF-chain. The isolators avoid standing waves on the SMA cable between the 2.8 K stage and the 15 K stage.*

The IF-chain at the 4 K stage of the dewar is similar to the first part of the IF chain of the HIFI Instrument, which is shown in Fig. 4.3. This chain includes two cryogenic isolators from Pamtech (USA) [43], which absorb signal reflections in order to avoid standing waves on the SMA cable between the mixer sub-assembly (MSA) and the amplifier input at the 15 K stage. The HEMT amplifier (high electron mobility transistor) is supplied by CAY (Centro Astronómico de Yebes (Spain), supplier for the amplifiers for the HIFI imstrument). It provides an average noise temperature of 4.2 K and an average gain of $25.5 \pm 1.3\,dB$ over the 4-8 GHz band [44].

For the test measurements, the first isolator is omitted because, unlike the set-up in the HIFI instrument [45], mixer unit and HEMT amplifier are both mounted on the 4 K stage of the test dewar close to each other.

The IF chain at room temperature

The schematic of the IF chain at room temperature is depicted in Fig. 4.4. It employs three low noise amplifiers, which amplify the weak signal, coming out of the dewar with a maximum gain of 73-69 dB (4-8 GHz), to power values, which can easily be measured with various devices, which follow the amplifier chain. Small attenuators avoid standing waves between the amplifiers. Together with a band pass, they avoid a saturation of the last amplifier. Thus,
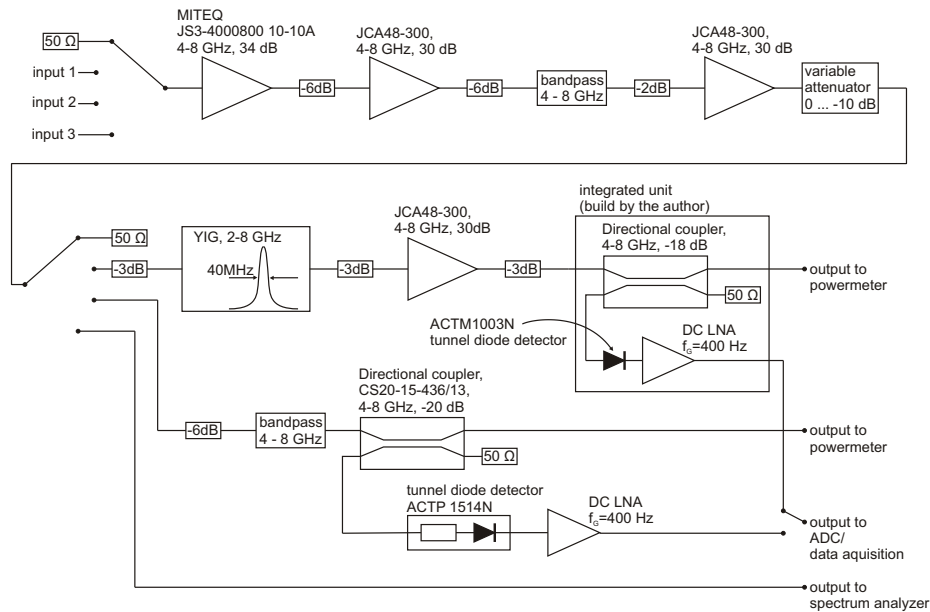
Fig. 4.4: *IF chain at room temperature. The various methods of IF output power evaluation enable a versatile use of the instrument.*

the instrument can be used with input levels up to -55 dBm without any gain compression. The subsequent variable attenuator is used to adapt the output power to the powermeter and to calibrate the detector diodes for different power levels with the powermeter.

With a manually or remotely controlled switch, the user may chose between a 4–8 GHz total power measurement, a variable narrow-band power measurement and signal analysis by means of a spectrum analyzer. All three signal paths contribute to a very useful and versatile instrument design:

The 4-8 GHz total power measurement is done via a -20 dB directional coupler, where 1% of the power is split and fed into a tunnel diode detector enabling fast $P(V)$-sweeps over the whole bias voltage range of the SIS-junction. For calibration and control purposes, the powermeter can be connected with the direct port of the coupler.

The narrow-band power measurement is done via a 6-stage YIG filter with 40 MHz bandwidth (FWHM) with a subsequent amplifier. The amplified signal is split by a 4-8 GHz directional coupler (-18 dB) on a RT/Duroid5880 substrate, which is integrated with a tunnel diode and a low noise DC-amplifier in a custom made box.

The output for the spectrum analyzer can be used for fast measurements of the noise temperature in the 3.0-8.3 GHz range. For this purpose, the spectrum analyzer is interfaced via a GPIB-interface to a computer with dedicated software.

The components of the IF chain are mounted on a Aluminum base plate which

is thermalized to a constant temperature of 20°C by a refrigerated circulator thermostat. This results in a good gain- and noise-stability of the instrument.

Software for hot/cold measurements with the spectrum analyzer

Parallel to the construction of the IF chain, a software for hot/cold-measurements has been developed. The software is able to interface any spectrum analyzer of the HP 8566/8567/8568/8569 A/B-series via the GPIB-interface. Many subsequent frequency sweeps can be accumulated in order to reduce the noise of the measurement. Absolute power values are calculated from the read out of the spectrum analyzer. The noise temperature $T_{SYS}(f)$ and the overall gain $G_{TOTAL}(f)$, are calculated with

$$T_{SYS}(f) \quad = \quad \frac{Y(f)T_{COLD} - T_{HOT}}{1 - Y(f)} \text{ with } Y(f) = \frac{P_{HOT}(f)}{P_{COLD}(f)} \qquad (4.3)$$

$$G_{TOTAL}(f) \quad = \quad \frac{k_B(T_{HOT} + T_{SYS}(f))}{P_{HOT}(f)} \qquad (4.4)$$

where T_{COLD} and T_{HOT} are the equivalent noise temperatures of the load and $P_{COLD}(f)$ and $P_{HOT}(f)$ are the corresponding power spectral densities (output of the spectrum analyzer is in [dBm/MHz]).

All relevant values including the standard deviation of each frequency channel $\Delta P(f)$ are calculated and displayed in real time. The variance is plotted versus time, which helps the user to determine the optimum number of sweeps. The variance plot also helps to detect erratic gain fluctuations of the particular spectrum analyzer used for most of the measurements.

4.1.3   Variable temperature load method (Y-factor measurements)

The variable temperature load method is a standard method widely applied for noise temperature measurements of low noise amplifiers and cryogenic IF systems for astronomical receivers. With the equipment used for the characterization of the IF of the HIFI band 2 mixers, an accuracy of 1-2 K can be achieved, which is similar to the accuracy of measurements of other groups [46]. Like in other systems, the actual physical temperature of the load is the main source of error [46]. The load with variable temperature is shown together with the cryogenic IF chain in Fig. 4.5.

The following compact construction is chosen to achieve a close thermal contact between the 50 Ω load, the heater and the temperature sensor: The load is press fitted in a small Al-block with an integrated heater. The Si-diode for the temperature measurements is sealed with Sycast-epoxy in a
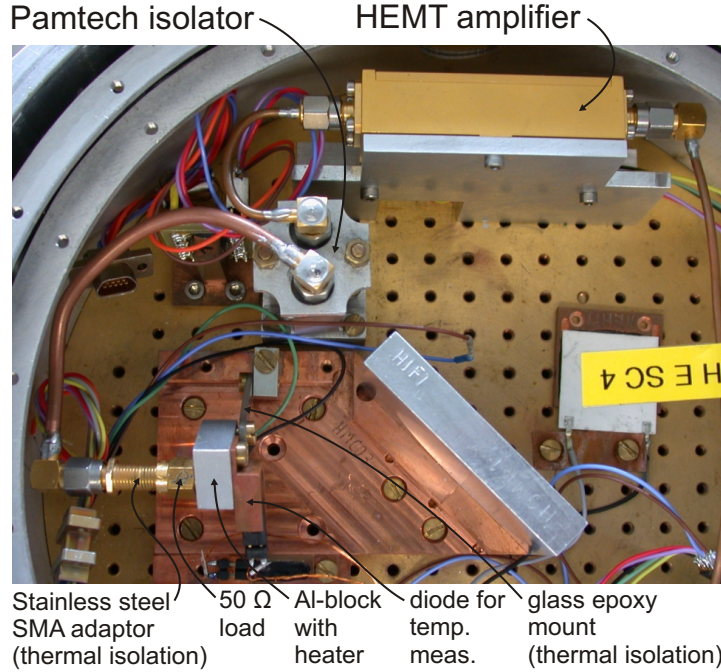
Fig. 4.5: *Load with variable temperature attached to the cryogenic IF chain. The 50 Ω load is thermally isolated by means of a stainless steel adaptor and an glass-fiber reinforced epoxy mount in order to improve measurement accuracy and to reduce the heat load to the 4 K stage.*
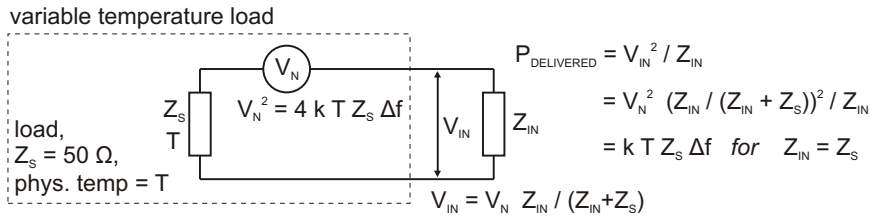
Fig. 4.6: *Equivalent circuit for calculation of the delivered power from the variable temperature load. For $Z_S = Z_{IN} = 50\,\Omega$, the delivered power is maximized: $P_{MAX} = k_B T \Delta f$*

Cu-carrier and can be screwed to the Al-block. The entire block is mounted to the 4.2 K stage by a thin piece of glass-fiber reinforced epoxy with low thermal conductivity. The connection to the 50 Ω line to the DUT is done via a stainless steel SMA adaptor, which provides moderate thermal isolation. This way, the temperature gradients in the Al-block are reduced to a minimum and the load temperature is similar to the temperature measured by the Si-diode, once the block is in thermal steady state equilibrium.

Besides temperature gradients in the small block, the calibration of the V(T)-curve of the Si-diode is a second source for a systematic error for the load temperature.

Between two measurements at different temperature levels, a heat up time of 1-2 min (thermalization included) and a much longer cool down time may
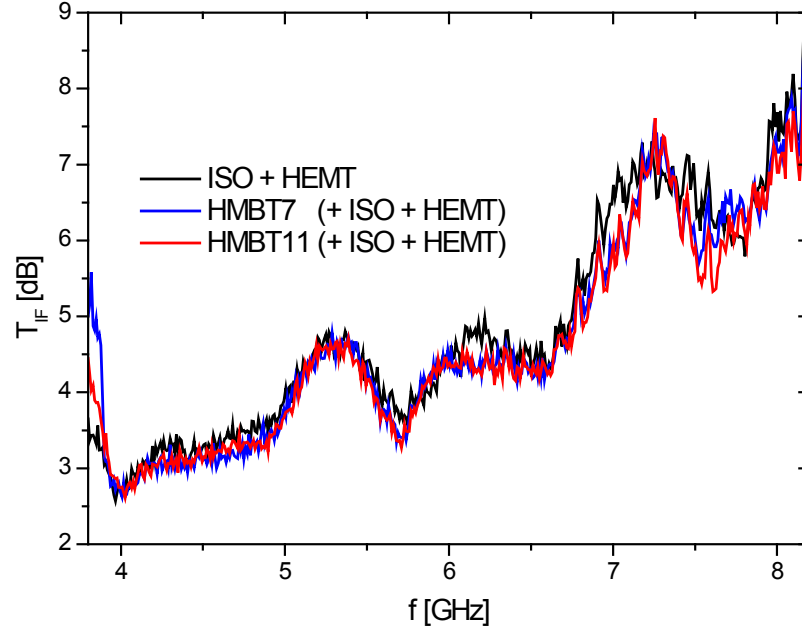
Fig. 4.7: *Measurements of IF noise temperature of ISO + HEMT and ISO + HEMT + bias-T. Every curve is the sum of at least 7 independent measurements. The contribution of the bias-T to the IF noise temperature is smaller than the error of the measurement.*

cause a further decrease of the accuracy due to small drifts in the overall gain of the IF chain. (Although the isolator and the HEMT amplifier of the cryogenic IF chain are in good contact with the He bath and the IF chain at room temperature is kept stable within $20 \pm 0.1°C$.

Fig. 4.6 sketches the calculation of the delivered thermal noise power. In the given case $Z_L = Z_{IN} = 50\,\Omega$, the maximum power $P_{MAX} = k_B T \Delta f$ is delivered to the input impedance of the IF chain. This means that in this case T_{HOT} and T_{COLD} correspond to the physical temperature of the load.

To characterize the performance of the bias-T at 4.2 K, two sets of measurements are necessary: First the noise temperature of the total IF-chain is determined without bias-T (see Fig. 4.5). In a second cool down, the noise temperature of the IF-chain including the bias-T is determined. This is achieved by mounting the bias-T on a special dummy mixer, which establishes the connection between the bias-T and the heated load. Fig. 4.7 shows T_{IF}-measurements for HEMT amplifier and isolator only (as shown in Fig. 4.5) in comparison with measurements including the bias-T. Every trace consists of the average of at least seven independent measurements. Although the measurements for different configurations are done at different days, the plot shows the good reproducibility of the noise temperature measurements. The excellent transmission of the bias-T at cryogenic temperatures makes it impossible to distinguish between measurements with and without bias-T. The same result can be obtained by looking to the average measured noise temperature of different configurations, which are summarized in Tab. 4.2.

cryogenic IF components	noise source	$\langle T_{IF} \rangle$ [K] (4-8 GHz)	ripple and slope [K] $\langle (T(f) - \langle T_{IF} \rangle)^2 \rangle^{1/2}$
HEMT YCF 6012	cold attenuator + noise figure meter (by CAY) [44]	4.2	0.3
ISO + HEMT	Var. temp. load	4.8	1.3
HMBT7 (FM1)	var. load temp.	4.6	1.3
HMBT8 (FM2)	var. load temp.	4.9	1.5
HMBT9 (FS1)	var. load temp.	5.5	1.4
HMBT11 (FM3)	var. load temp.	4.6	1.2
FM1 (HMBT7)	SIS shot noise $(V > V_{GAP})$	5.9	3.6
FM3 (HMBT11)	SIS shot noise $(V > V_{GAP})$	5.6	3.5

Tab. 4.2: *Averaged noise temperatures for different setups and measurement methods. Although the shot noise measurements are compensated for the mismatch between junction impedance and 50 Ω line impedance, they show a +1K offset in comparison with the variable load temperature results.*

All flight bias-T's have been characterized in this way prior to assembly on the mixer unit. For all measurements with different bias-T's and without bias-T, the differences are smaller than the error margins.

4.1.4 Shot noise measurements
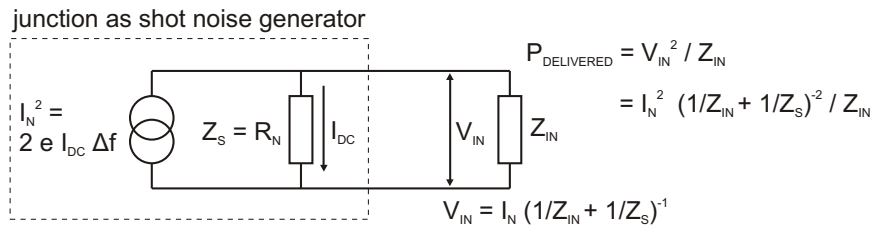
Fig. 4.8: *Equivalent circuit for the calculation of the delivered power from the SIS-junction as shot noise generator with impedance $Z_L = R_N$*

When the SIS-junction is biased above the gap, it can be used as shot noise source with an impedance $Z_L = R_N$ equal to the dynamic resistance, which is equal to the normal resistance R_N for $V > V_{GAP}$. The mean transit time of the quasi particles through the tunnel contact is very short, hence a very high cutoff frequency of the noise spectral distribution can be expected. Thus, the shot noise can be considered as independent of frequency within the IF band. At bias voltages above the gap voltage of the SIS-junction ($V_{BIAS} > V_{GAP}$), the noise current I_N can be described with a current source with
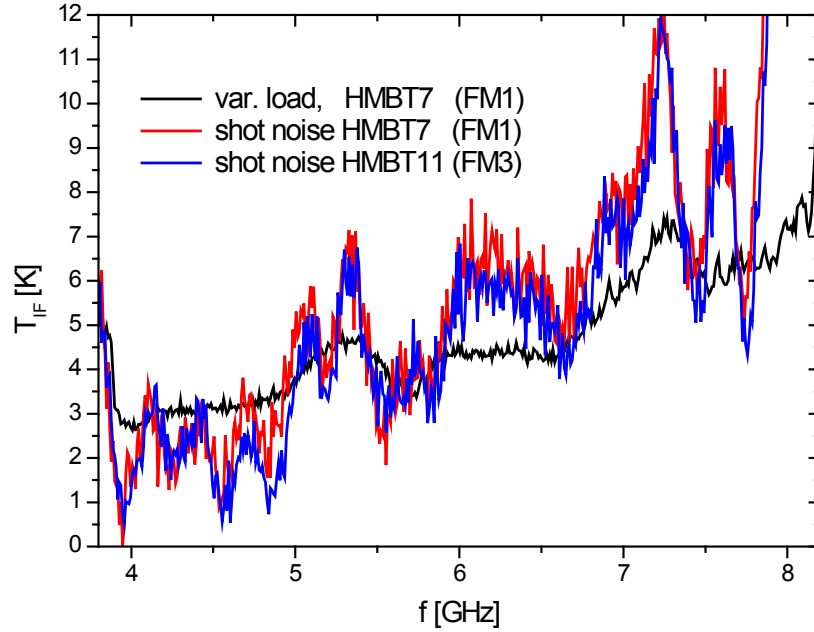
Fig. 4.9: *IF noise temperature measured with shot noise from SIS-junction biased above the gap voltage. The used equivalent load temperatures (e.g., equation 4.5) lead to considerably more ripple and slope of the T(f) traces compared to the measurements with the heated load method.*

$I_N^2 = 2\,e\,I_{DC}\,\Delta f$ parallel to the tunnel contact [47], [48]. Fig. 4.8 illustrates the calculation of the delivered noise power $P_{DELIVERED}$.

With $P_{DELIVERED} = k_B\,T_{EQUIV}\,\Delta f$, an equivalent load temperature T_{EQUIV} can be calculated. For example, the calculation for the junction PS8_C_19 with $R_N = 19.1\,\Omega$ which is used in FM1, yields for V=4 mV and V=7 mV:

$$
\begin{aligned}
T_{COLD} &= T_{EQUIV}(4\,mV) = 18.6\,K \\
T_{HOT} &= T_{EQUIV}(7\,mV) = 32.5\,K
\end{aligned}
\qquad (4.5)
$$

This can be used for calculations of the system noise temperature $T_{SYS}(f)$. The result of such a measurement can be seen in Fig. 4.9 for FM1 ($R_N = 19.1\,\Omega$) and FM3 ($R_N = 21.49\,\Omega$).

A somewhat more correct calculation takes into account that the actual input impedance $Z_{IN}(f)$ is different from $50\,\Omega$ and varies with frequency. $Z_{IN}(f)$ can be estimated using the model shown in Fig. 4.10.

Fig. 4.11 shows $Z_{IN}(f)$ and the corresponding calculation for T_{SYS}. The correction for $Z_{IN}(f)$ has only a week influence of the calculated noise temperature.

The conspicuous ripple and slope, which runs in parallel to the ripple measured for the IF-chain itself, can not be explained up to the moment. Nevertheless, the mean noise temperatures over the 4-8 GHz range obtained with the shot

Junction+Tuning Capacitance   Bonds to GND (in mixerblock)   Bonds to SMA jack (in mixerblock)   SMA cable   bias-T HMBT7   HEMT+ISO Z_{IN}=50 Ω
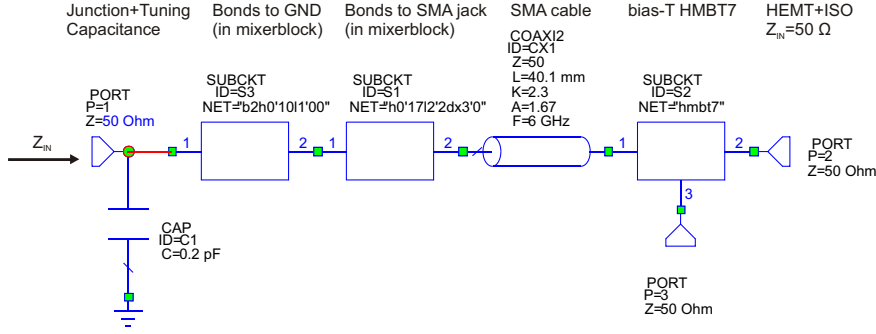
Fig. 4.10: *Schematic for the calculation of $Z_{IN}(f)$. The strongest influence on deviations from the nominal $50\,\Omega$ input impedance comes from the junction capacitance and the wire bonds in the mixer block. The model for the calculation of $Z_{IN}(f)$ uses best estimates for the C_{J+T} and wire bond height and length. The bias-T, which has only marginal influence, is terminated with an approximate impedance of $50\,\Omega$ which is composed by HEMT amplifier and isolator.*
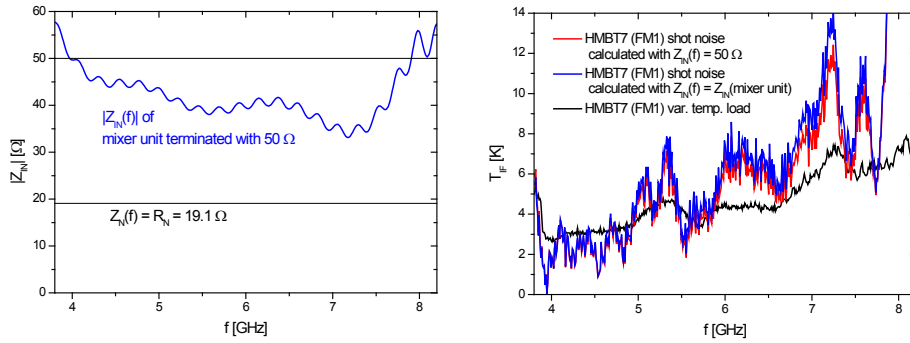
Fig. 4.11: *Left: $|Z_{IN}(f)|$ calculated with the model in Fig. 4.10.
Right: IF noise temperature measurement with shot noise. The plot shows a trace with $Z_{IN} = 50\,\Omega$ and $Z_{IN} = Z_{IN}(f)$. The correction has only a small influence.*

noise method are comparable with the other noise temperatures in Tab. 4.2 within the error margins.

4.2 Heterodyne measurements with the flight-models for HIFI band 2

A detailed characterization of the heterodyne performance of the mixer units is essential for the use in the HIFI instrument. Only when the optimum bias voltage, optimum LO power and optimum magnet current is known, the mixers are suitable for remote operation. A detailed analysis of the noise properties as a function of LO frequency f_{LO} is needed to check the quality of the mixer chip (quality and current density of the SIS tunnel junction and film quality of the tuning structure, the probe and the RF blocking filters).

Likewise an analysis of the noise temperatures (at a fixed f_{LO}) as a function of the IF frequency f_{IF} is needed to check the performance of the bias-T and the other IF connections.

4.2.1 RF noise measurements
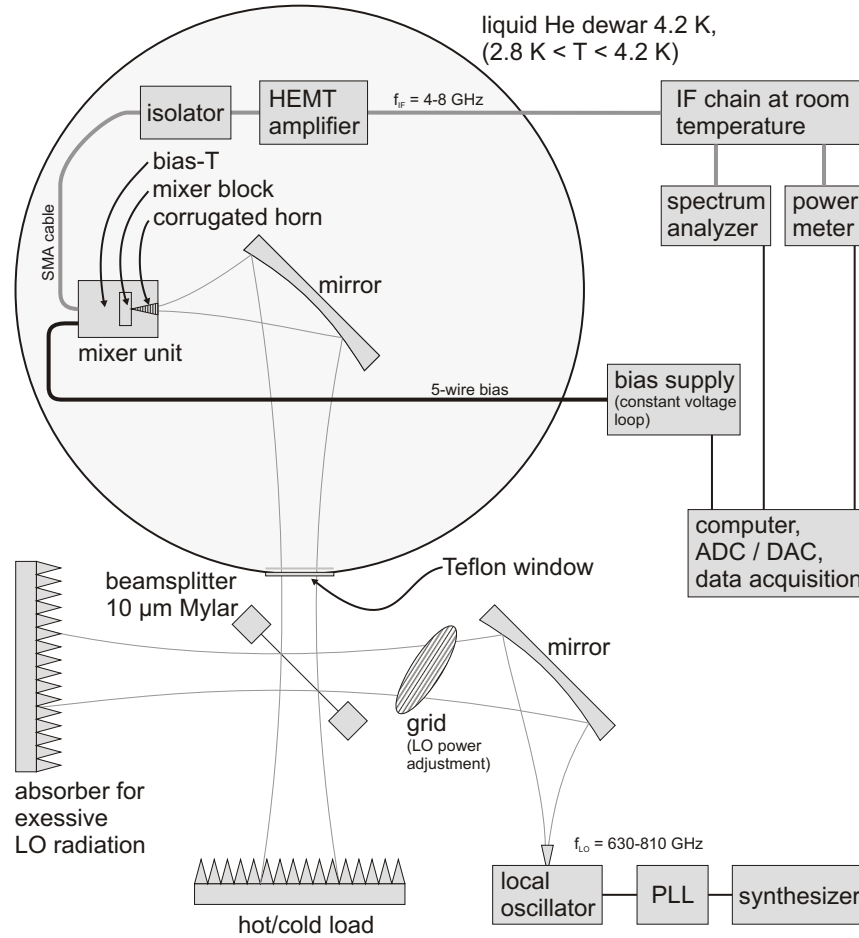
Fig. 4.12: *Heterodyne test setup for the characterization of the HIFI mixer units. The signal from the hot/cold load is superimposed with the LO signal by means of the beam splitter and focussed to the waist of the corrugated feed horn by the Gaussian optics. The IF signal is amplified and evaluated with the power meter and the spectrum analyzer.*

Fig. 4.12 gives an overview of the test setup for the heterodyne measurements. The noise signal of the hot/cold load is superimposed with the monochromatic LO signal with a $10\,\mu m$ beam splitter, which is situated close to the waist of the Gaussian beam in the dewar window. The focussing $90°$ mirror reflects the beam into the corrugated feed horn of the mixer unit. By sweeping the bias-voltage, it is possible to obtain $I(V)$ and $P_{IF}(V)$ curves of the SIS-junction for different LO frequencies and LO powers.

Measurements with the hot/cold load (295 K/77 K) immediately result in

the Y-factor $Y = P_{HOT}/P_{COLD}$ and the system noise temperature (equation 4.3) for a given setting. For the heterodyne measurements, the equivalent temperatures of the load have to be calculated with the Callen-Welton formulation [49] because $\frac{hf}{k_B T} = 0.09 \ldots 0.45 \not\ll 1$. From the system noise temperature T_{SYS} and the system gain G_{SYS} (equation 4.3) the mixer noise temperature T_{MIX} and the mixer gain G_{MIX} can be evaluated by considering the losses in the optics and the noise and gain of the IF chain. A detailed analysis is given in [13]. Fig. 4.13 shows the "HIFI receiver noise temperature" $T_{REC\,HIFI} \overset{\text{def}}{=} T_{MIX} + \frac{10\,K}{G_{MIX}}$, which is defined for a 10 K IF chain noise temperature in order to account for the influence of the mixer gain.
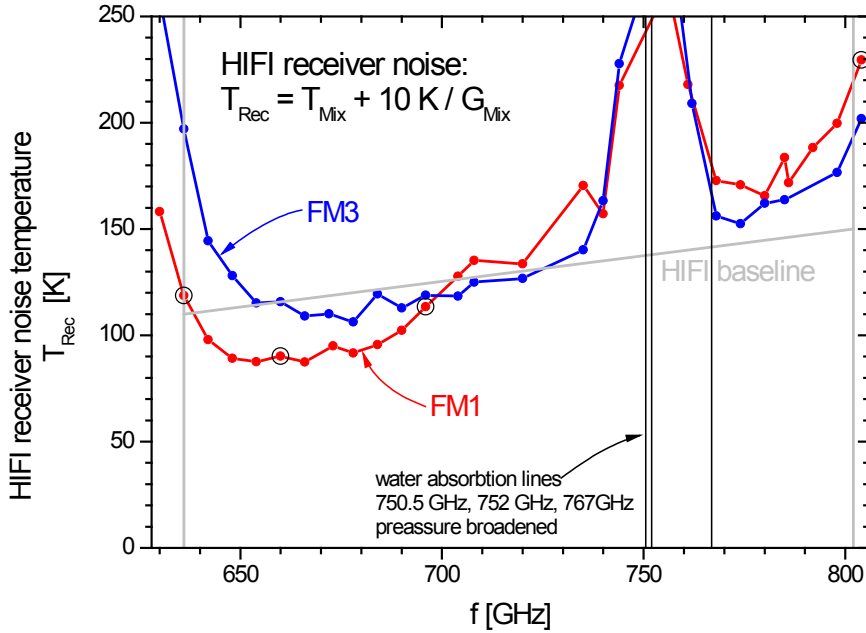
Fig. 4.13: *HIFI receiver noise temperature T_{REC} of FM1 and FM3 calculated with an IF chain noise temperature $T_{IF} = 10\,K$. Around the water line at 750.5 GHz the noise temperature is dominated by the absorption of water vapor in the optical path between hot/cold load and dewar window. The IF performance of FM1, shown in Fig. 4.14 and 4.15, is calculated for the RF frequency points surrounded by a black circle.*

4.2.2   IF noise measurements

Fig. 4.14 and 4.15 present noise and gain measurements of FM1 at different LO frequencies. The measurements differ not only by the mixer noise $T_{MIX}(f)$ and gain $G_{MIX}(f)$, but also by the source impedance presented by the SIS-junction. While the reactive part (C_{J+T}) remains constant, the dynamic resistance at the optimum bias point and pump level varies from $102\,\Omega$ at 804 GHz to $215\,\Omega$ at 636 GHz. In section 2.6.3, the effect of such a change in the source impedance is discussed. The dynamic resistance has

been measured by linear fitting of the I(V) curve in the vicinity of the optimum bias point (FM1: $V_{BIAS} = 2.0\,mV$, pump level: $I_{BIAS} = 35\,\mu A$ for all LO frequencies).

For each selected LO frequency, a $T_{SYS}(f_{IF})$ plot is presented. The IF band is very flat, but shows some ripple in dependence of the LO frequency. The ripple over the IF band is due to standing waves in the RF optics. At the RF band edges, the match between the SIS-junction (as RF load) and the optics degrades, which results in an increased reflection coefficient of the mixer.

Another interesting quantity is $G_{MIX}(f_{IF})$, which is shown in the plots below. It is calculated from the gain of the IF chain $G_{IF\ chain}(f_{IF})$, the losses in the optics $G_{OPTICS}(f_{LO})$ and the total gain of the system $G_{SYS}(f_{IF})$ measured with the Y-factor method using equation 4.3:

$$G_{MIX}(f_{IF}) = \frac{G_{SYS}(f_{IF})}{G_{IF\ chain(f_{IF})}G_{OPTICS}(f_{LO})} \tag{4.6}$$

The plots show a flat gain within the measurement accuracy ($\approx 1\,dB$). Again at $f_{LO} = 804\,GHz$ an influence of standing waves in the optics can be observed. The mean values over the 4–8 GHz IF band show an excellent agreement with values obtained from $P_{IF}(V)$ curve fits, which are presented in [13].
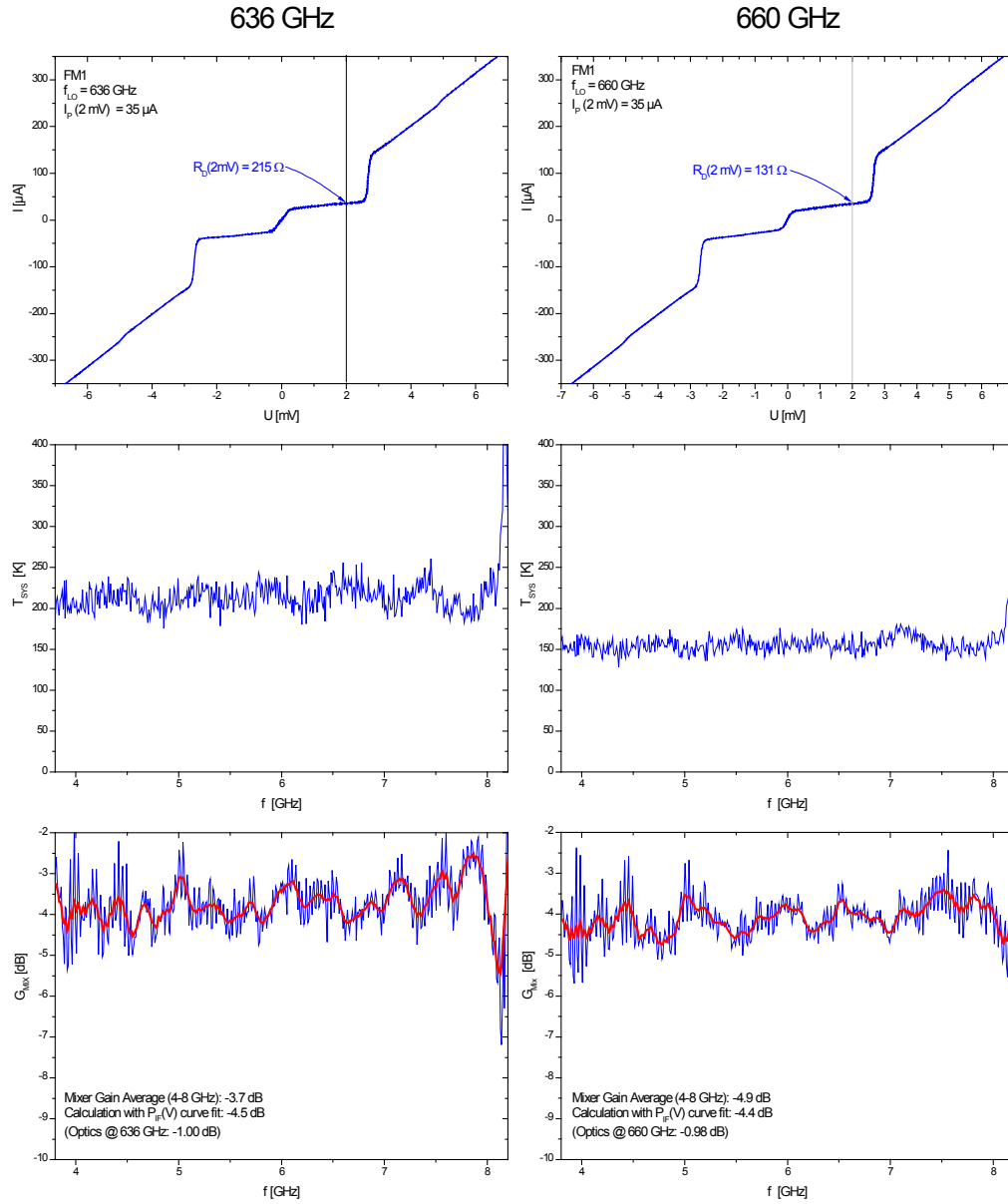
Fig. 4.14: *Noise and gain measurements over the 4-8 GHz IF band for four different LO frequencies. For each LO frequency, an $I(V)$-curve at optimum LO power, a $T_{SYS}(f_{IF})$ plot and a $G_{MIX}(f_{IF})$ plot for optimum bias voltage is presented. ($V_{BIAS} = 2.0\,mV$, optimum pump level $I_{BIAS} \approx 35\,\mu A$) The curves show a flat IF band. The wiggles occurring at some LO-frequency points are due to standing waves in the optics of the experimental setup. (See Fig. 4.12)*

696 GHz

804 GHz
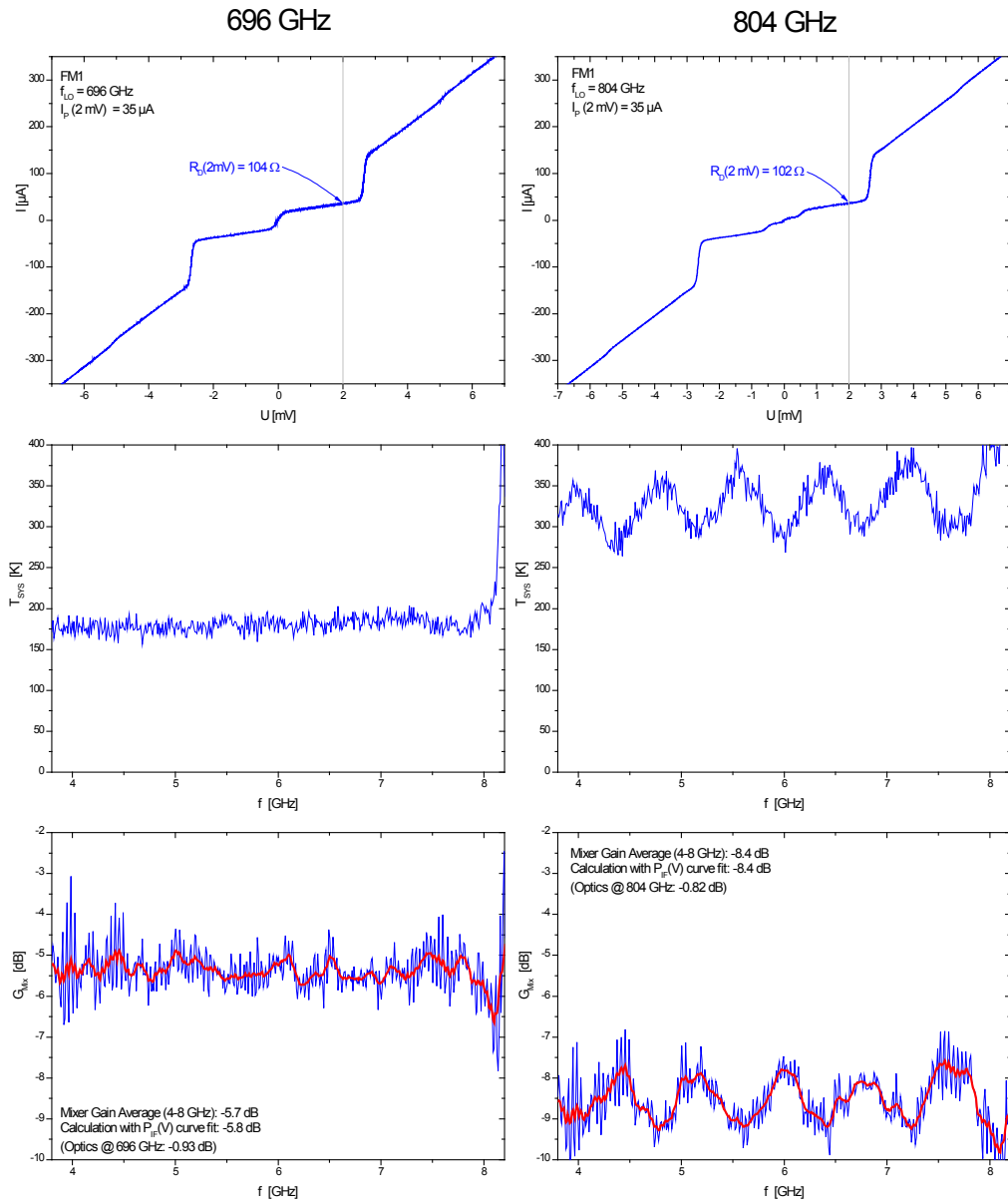
Fig. 4.15: *For a description, please refer to Fig. 4.14.*

4.3 EMI tests

For the mixer unit, an electromagnetic interference (EMI) proof design is very important. Electromagnetic noise (e.g., spikes from power line switching) can result in fluctuations of the bias voltage which can affect the receiver stability (Allan time) [17].

Especially in the 4-8 GHz IF band the mixer units need a very good shielding because there are several high power transmitters and oscillators on board of the Herschel spacecraft (For instance, oscillators in the WBS and HRS, which are switched ON during HIFI operation.) Noise which passes the shielding would immediately result in noise in the IF signal. A maximum EMI noise contribution of 0.5 K is accepted for the HIFI mixers [17]. Another strongly disturbing effect would be feedback caused by large signals from the end of the IF chain reentering in a poorly shielded mixer unit.

In order to be able to compare this acceptable 0.5 K noise level with the CW signal power of the EMI test facility, one has to calculate a minimum noise power by integrating the noise spectral density over the minimum instrument resolution bandwidth, which is 134 kHz (bandwidth of one HRS channel). Thus, the maximum noise power per channel is

$$k_B \cdot 0.5\,K \cdot 134\,kHz = 9.2\,10^{-19}\,W = -150\,dBm \qquad (4.7)$$

The maximum allowed power levels are defined in [50] as follows:

The generic requirement is $P_{MAX} < -93\,dBm$, in the 2-4 GHz range $P_{MAX} < -98\,dBm$ and in the 4-8 GHz range $P_{MAX} < -155\,dBm$ according to equation 4.7 (with -5 dB margin).

4.3.1 EMI test facility

Because of the importance of an EMI proof design, the EMI rejection performance has been tested three times: for the DM, for a "pre-QM" and for the QM1 design at the "EMC test laboratory" of the NLR, Marknesse, NL.

Fig. 4.16 shows a schematic of the test facility and two pictures of the used antennas. The test procedure is described in detail in [51]. The radiated E-field susceptibility was determined by measuring the power at the IF output of the mixer while irradiating the mixer with a CW signal with an E-field strength of 2 V/m in the range from 1 MHz to 18 GHz. During the test, unshielded cables of 1 m length were attached to the bias input connector. These cables should have a comparable antenna effect as the bias cables inside the Herschel cryostat. (The bias cables are not shielded to reduce the heat transfer into the cryostat in order to maximize the instrument lifetime.)
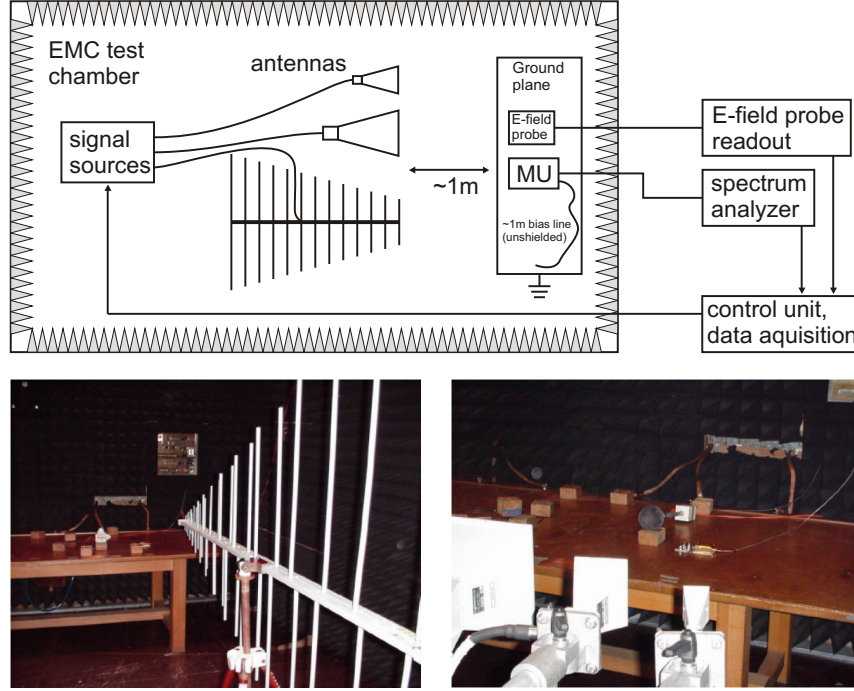
Fig. 4.16: *Above: Overview of the EMI test setup. The mixer unit is placed on a massive ground plane while being irradiated by means of various antennas for different frequency ranges. The E-field in the vicinity of the mixer unit is measured by an E-field probe. The mixer unit is tested with 1 m unshielded lines attached to the bias connector, which should have a similar effect as the unshielded bias lines in the Herschel cryostat.*
Below: Yagi-antenna for the 0.1-1 GHz range (left) and horn antennas for the 1-18 GHz range (right). A mixer unit and an E-field probe can be seen in the background on top of the ground plane.

4.3.2   EMI test results compared with maximum levels in the Herschel cryostat

The mixer unit for band 2 turned out to have the best shielding (compared to other mixer units) due to the careful design of the filter circuit and the EMI proof design of all boxes [51]. The test results can be scaled down to actual E-field levels in the FPU in order to compare them to the maximum allowed power levels.

During operation of the HIFI instrument, the E-field levels at the FPU, estimated by Alcatel are $8\,mV/m$ falling to $2\,mV/m$ in the 4-8 GHz band [16]. (Based upon HIFI's high sensitivity to E-fields in the HIFI IF band, ESA/Alcatel have agreed to place a notch in this band.) With

$$\frac{P_{EMC\,TEST}}{P_{FPU}} = \frac{E^2_{EMC\,TEST}}{E^2_{FPU}} \tag{4.8}$$

and $E_{EMC\,TEST} = 2\,V/m$, one obtains

$P_{FPU} = 1.6 \, 10^{-5} \, P_{EMC \, TEST}$ (-48dB) and

$P_{FPU} = 1.0 \, 10^{-6} \, P_{EMC \, TEST}$ (-60dB) for the 4-8 GHz range.

Fig. 4.17 compares the maximum allowed noise levels with the measured and down scaled EMI levels. From this plot it is clear that the band 2 mixer units meet the EMI specs in the whole range except from 6.5 GHz to 8 GHz, where the trace exceeds the limits with approximately +20 dB. This leakage is identified with a change in the mixer block design in comparison with the DM which did not show such a characteristic in EMI measurements [52]. A check of the performance of the bias-T circuitry separated from the mixer block confirms this interpretation (compare Fig. 4.17). For the QM and FM design, the aperture of the responsible slits is reduced to the old DM design values. So the QM/FM design is expected to meet the EMI requirements over the whole band.
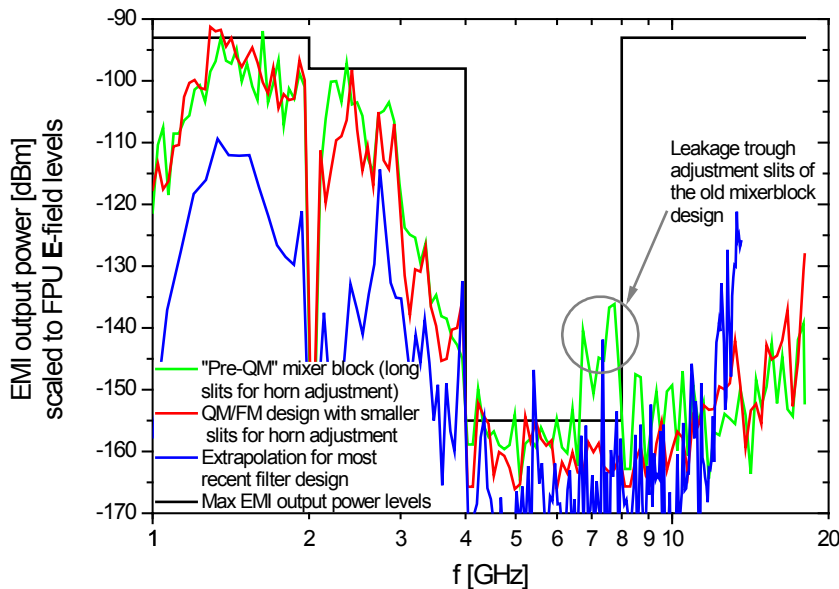
Fig. 4.17: *EMI power at the IF output of the mixer unit scaled to FPU E-field levels. The "Pre-QM" design with long adjustment slits in the mixer block fails the test in the 6.5-8 GHz range. The QM/FM design uses small slits as already tested in the DM. The EMI rejection performance of an improved model (QM1) is also added to the plot.*

4.3.3 EMI filter with improved performance

From the measurements presented in Fig. 4.17 it became clear that the EMI rejection performance of the bias-T is only limited by the bias line filtering and not by any leakage of the housing. Because the bias-T can easily be separated from the mixer block (modular design), it is easy to measure the EMI rejection by means of a small adaptor between SMA and the MDM connector, which is shown in Fig. 4.18.
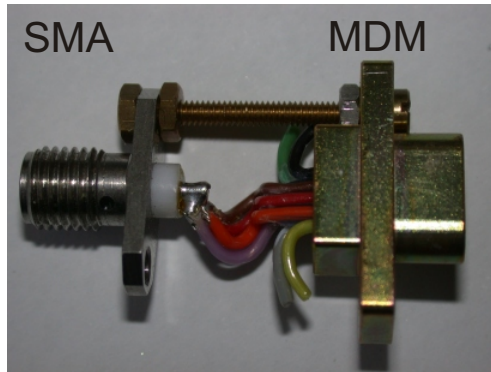
Fig. 4.18: *SMA to MDM adaptor used for EMI tests with a network analyzer. The SMA inner conductor is connected with all non-GND bias lines of the MDM connector.*

By simply measuring the transmission with a network analyzer and the adaptor plugged to the bias input connector of the bias-T, it is possible to compare different filter designs to the filter measured in the EMI test laboratory. Fig. 4.19 shows the EMI rejection performance of a filter design with improved performance in the low frequency range in comparison with the tested filter.
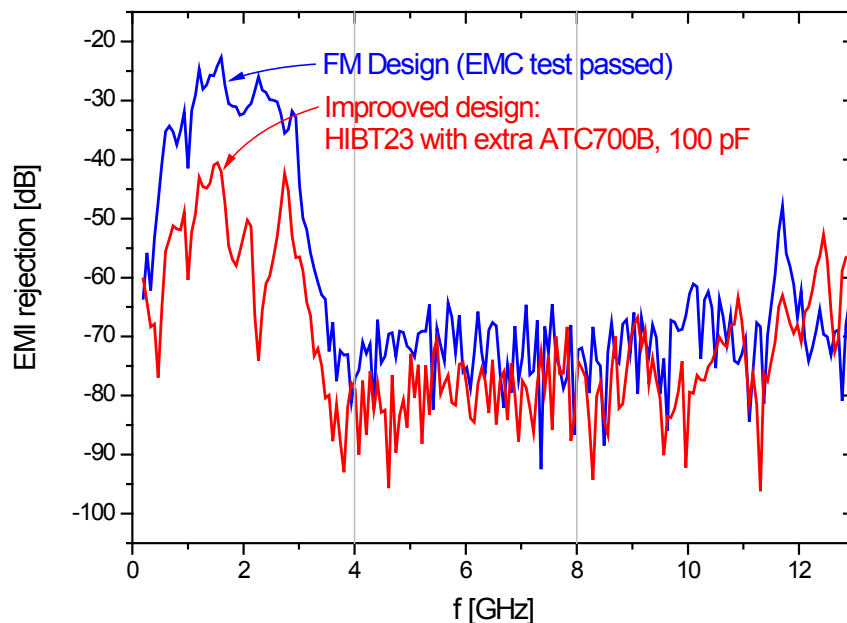
Fig. 4.19: *The EMI rejection performance of the improved design (HIBT23, QM1) in comparison with the "pre-QM" design tested at the NLR facility. Special attention has been given to improve the filter performance in the low frequency range.*

By comparing the transmission of both filters, it is possible to extrapolate the performance to the FPU E-field levels. This is added to Fig. 4.17 (blue

trace).

This improved design with an additional ATC700B 100 pF capacitor glued to the TMM10 board and a large radial stub was integrated in QM1 and passed the complete qualification program.

Chapter 5

Environmental tests

5.1 Vibration tests

The mixer unit is subjected to mechanical vibration and shock during shipment, handling (e.g., integration into the FPU) and launch. During the shipment, the shock levels are controlled by mechanical shock detectors. During flight, the payload is subjected to static and dynamic loads induced by the launch vehicle (Ariane 5 with strap-on boosters P230). Such excitation may be of aerodynamic origin (wind, buffeting at transonic velocity, etc.), or due to the propulsion systems (thrust build-up, tail-off transients, structure-propulsion coupling, etc.). The highest static longitudinal acceleration occurs at the end of the boosters burn phase. It will not exceed 4.55 g [53]. Furthermore, the spacecraft is subjected to mechanical shocks mainly during separation of the fairing and on actual spacecraft separation. Although the Ariane 5 launcher provides comparatively low vibration levels, the mechanical stress can be highly increased by resonance- and lever-effects.

Thus, the HIFI mixer units will be exposed to high random vibration levels during launch, due to a combination of:

- Relatively high input levels on the Herschel Optical Bench

- A resonance frequency within the main FPU structure of approx. 160 Hz

- A resonance frequency within the mixer console of approx. 270 Hz

The very hard qualification test levels have been defined with some margin included to balance the uncertainty in the Q-factors of the FPU and console resonances [16]. These levels should be applied to all three axes at cryogenic temperatures (i.e. at $T < 90\,K$).

Random vibration test, 2 minutes each axis		
f	Level	
20-100 Hz	$+6\,dB/Oct$	HIFI test levels
100-500 Hz	$0.4\,g^2/Hz$	HIFI test levels
500-2000 Hz	$-6\,dB/Oct$	HIFI test levels
High-level, low frequency sine sweep		
5-21.3 Hz	$\pm 11\,mm$ displacement	HIFI test levels
21.3-100 Hz	20 g, 2 oct./min sweep rate	HIFI test levels
100-2000 Hz	20 g, 2 oct./min sweep rate	Internal test levels

Tab. 5.1: *Table with the qualification test levels for the HIFI mixer units. The last item in the table was added in order to access possible high frequency resonances of the small mixer unit parts.*

5.1.1   In-house test facility

A picture of the KOSMA vibration test facility (RMS-Testsystems, Germany) is shown in Fig. 5.1.
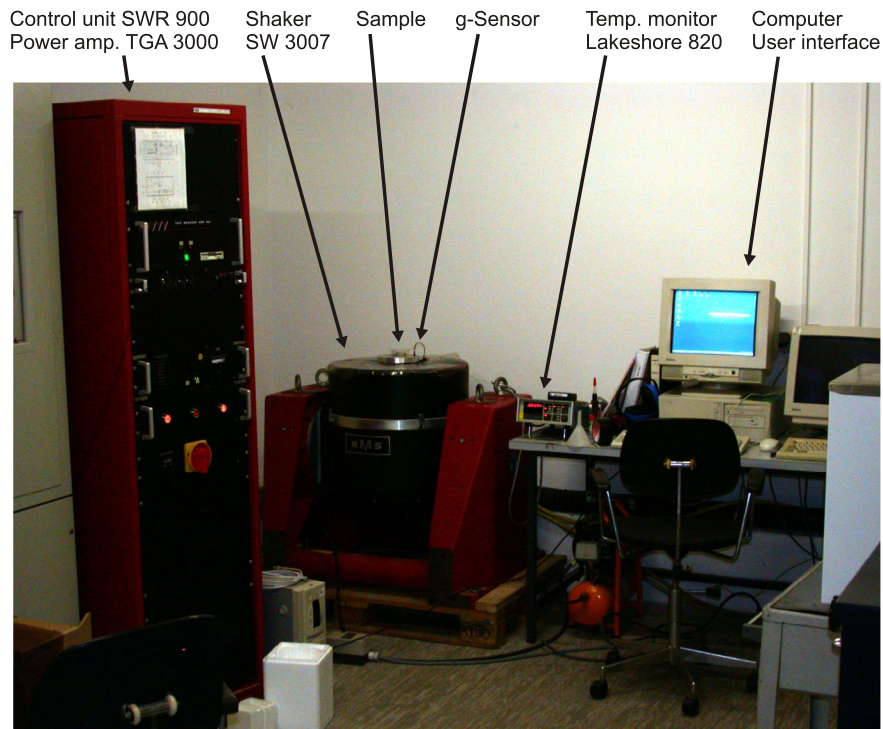
Fig. 5.1: *KOSMA vibration test facility.*

The electrodynamic shaker SW 3007 has the following maximum amplitude values: $s_{MAX} = 13\,mm$, $v_{MAX} = 1.2\,m/s$, $a_{MAX} = 100\,g$ and is operating in a frequency range of $f = 0 - 3\,kHz$. Thus, it is suitable to test the mixer unit for the levels given in Tab. 5.1. The movements of the shaker are measured with a piezoelectric acceleration sensor (PCB Piezotronics, M353B18,

$1.02\,mV/(m/s^2)$). The shaker is driven by the control unit SWR 900 with a high power amplifier (TGA 3000). The vibration levels are set up by means of a feedback loop.

5.1.2 Mixer unit critical parts

The mixer unit design is very rugged due to its almost cubic form and the three point mount of the bias-T to the mixer bracket. The only remaining points of concern, regarding vibration, are flexible connections, which are designed to compensate for thermal contraction. These connections are:

- The bond wires between mixer chip and the partly free standing inner conductor of the SMA jack of the mixer block.

- The Alumina ESD filter board, which is fixed in the housing by tiny CuBe clamps.

- The connection between the inner conductor of the SMA cable and the microstrip line on the RT/Duroid6002 board by thin Habia wire strands. (Possible vibration of the partly free standing inner conductor.)

5.1.3 The bond wires to the SMA jack in the mixer block

Fig. 2.7 in section 2.6 shows a close up of the bonds in the mixer block and the short, but free standing SMA inner conductor. This connection has been tested with a vibration test at DLR, (Berlin, Germany) already in an early design phase of the DM and proved its reliability in all subsequent tests.

5.1.4 The Alumina board clamps

One of the major concerns regarding mechanical stress was the behavior of the ESD board. The board can not be glued into the box because of it's low thermal expansion coefficient, which would result in a failure of the adhesive bond due to mechanical stress at repeated cool down. The $23.5 \times 12.4 \times 0.635\,mm^3$ Alumina board is clamped with three little Copper-Beryllium strips into its housing (98% Cu, 2% Be, strip thickness: 0.2 mm). The clamping mechanism, developed together with M. Schultz, is partly integrated in the box walls in order to save space. Fig. 5.2 shows a photo of the ESD box with the CuBe clamps and Fig. 5.3 shows the functional principle in the closeup. Commercially available clamps could not be used within the small envelope of the mixer unit because of their large size.

The small board, including components and Habia wire, has a weight of about 1.05 g, which corresponds to a load of 21 g at an acceleration of 20 g.
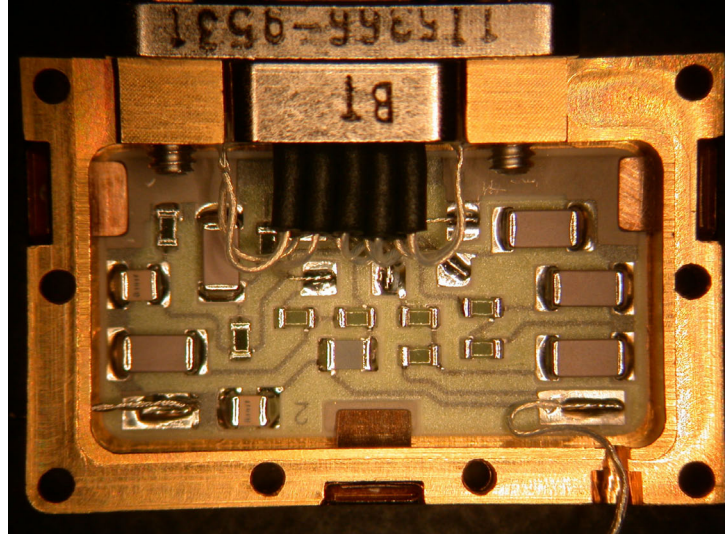
Fig. 5.2: *ESD filter board (Alumina) fixed in the housing by three CuBe clamps. The clamps are partly integrated in the box walls in order to save space.*
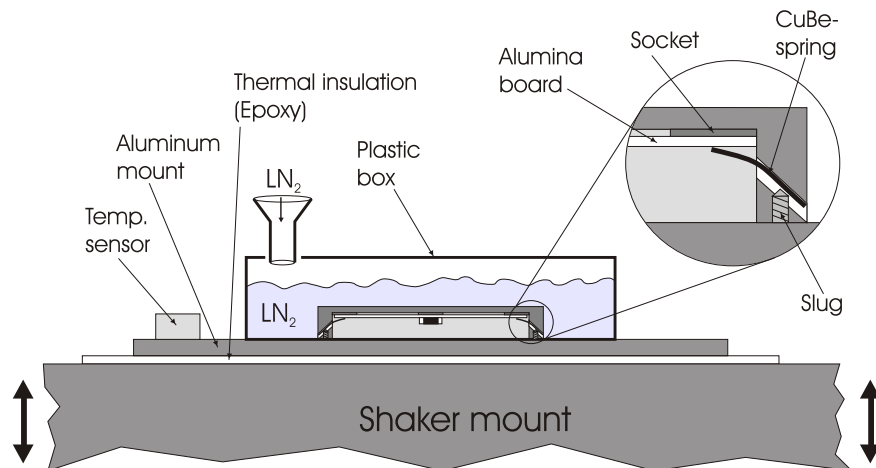
Fig. 5.3: *Vibration test at $T{<}83\,K$ for the Alumina board clamping mechanism. The details of the CuBe clamp geometry are shown in the closeup. During the vibration test, a permanent refill of liquid N_2 has been necessary to compensate losses by spreading.*

The 3-point bending strength is a good measure to appreciate the resistibility of Alumina boards:

$$\sigma(F) = F\frac{3l}{2wt^2} \tag{5.1}$$

where F is the load applied to a sample of test length l, width w and thickness t. Manufacturers claim a 3-point bending strength of up to $\sigma_{MAX} = 330\,MPa\ldots660\,MPa$ for their products, which corresponds to a maximal applyable force of $F/g = 4.8\,kg\ldots9.5\,kg \gg 21\,g$ for the used board dimensions. This is much higher then the expected vibrational stress,

but it does not account for the small support of the three sockets, burrs and other irregularities of the clamping mechanism. Because it is very difficult to take into account all structural imponderabilities and the effects of vibrational stress under cryogenic temperatures, it was thought necessary to test the structure intensively before using it for a space application.

Fig. 5.3 shows the test fixture used for the vibration tests. The fixture is thermally isolated against the shaker mount by an epoxy layer and surrounded by a housing with a small hole for continuous refill of liquid Nitrogen during the vibration test. With this arrangement, it is possible to cool the sample down to $T < 83\,K$. The temperature was monitored with a Lakeshore 820 instrument and a calibrated Si diode.
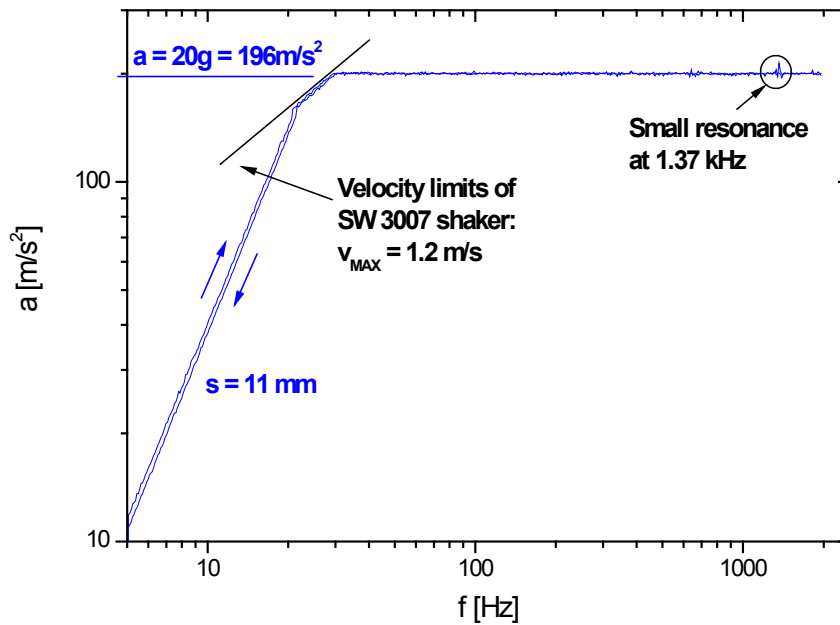
Fig. 5.4: *High level sine sweep. The frequency is tuned up at a constant rate (2 oktaves/min) from $f_{MIN} = 5\,Hz$ to $f_{MAX} = 2\,kHz$ and then tuned down again at the same rate. During the frequency sweep, the acceleration is measured permanently and regulated to the desired values. This particular measurement is a high level sine sweep with the "ProtoFM" mixer unit along the horn axis. The small resonance at $1.37\,kHz$ could not be attributed to a particular detail of the mixer unit.*

Fig. 5.4 and 5.5 show examples of a high level sine sweep and a random vibration noise spectrogram. The curves are recorded by means of the acceleration sensor, which was attached directly to the shaker mount because the small size of the mixer units did not allow to glue the sensor directly to the samples. This limits the sensitivity to resonances of the samples. The clamping mechanism and the Alumina board survived vibration tests along all 3 axes at room temperature. The cryogenic vibration test could only be done along the most critical axis perpendicular to the surface of the board.

The tests with the qualification test levels defined in Tab. 5.1 and some tests with even higher levels allowed to gain confidence in the structure and to give green light to proceed with the electrical design.
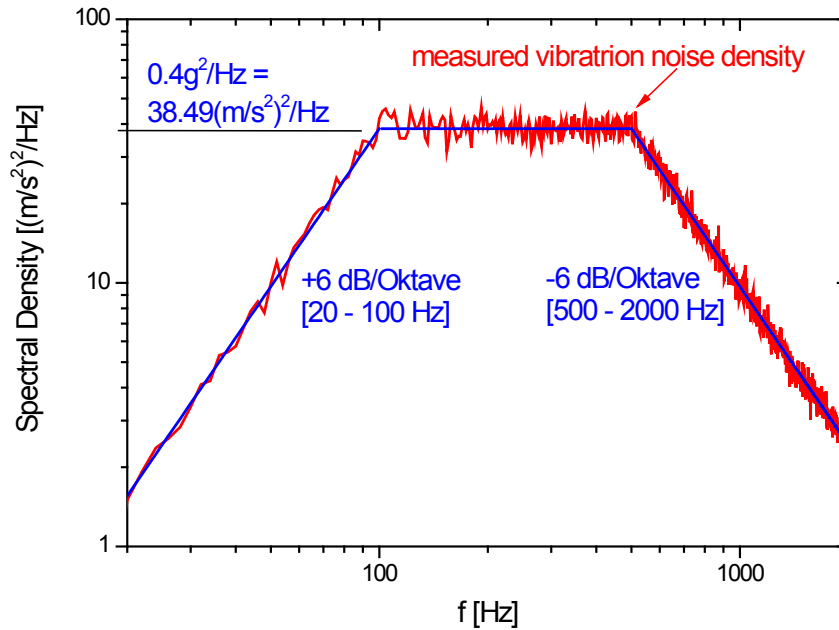
Fig. 5.5: *Measured noise density during a 4 min random vibration test. After each test, the sample has to be checked for any changes in mechanical and electrical parameters.*

5.1.5 Redesign of the adhesive joint of the Habia-wire strands

Vibration tests with the whole mixer unit at very high sine vibration levels (60 g, up to 2 kHz) revealed a failure of the adhesive bond of two very thin strands to the RT/Duroid6002 board in the bias-T box (compare section 2.7.8). This contact is necessary to bias the SIS-junction and, thus, is a single point of failure. The strands are soldered to the inner conductor of the SMA cable, which connects the bias circuits with the mixer block. On the other side they are glued to the microstrip line on the RT/Duroid6002 board with conductive silver loaded epoxy, EPO-TEK H20E, in order to assure the DC contact between the cable and the microstrip. Fig. 5.6 shows the old configuration on the left and the new on the right.

The new strand topology provides slightly more slack of the strands which allows minimal movements of the inner conductor relatively to the microstrip line. These movements are considered to originate from a resonance of the whole SMA cable bow ($L = 21.7\,mm$) rather than from the inner pin ($f_{RES} \approx 71\,kHz$, with material=Cu, $l = 1.5\,mm$, $r = 0.26\,mm$). The lead-back of the
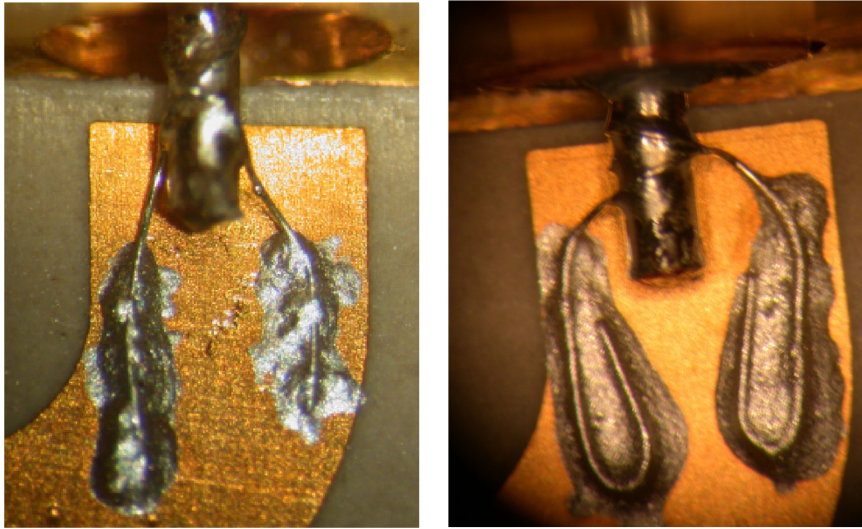
Fig. 5.6: *Comparison of old (left) and new (right) configuration of the strands enabling DC contact between SMA cable and microstrip line for the bias voltage of the SIS-junction. The new configuration provides more slack and higher strength and reliability due to the loop.*

strands in the gluing area doubles the contact area and, thus, the contact strength. The special form enables functionality (DC contact) even with a partially ruptured bond.

5.1.6 Qualification- and acceptance- test level vibration at cryogenic temperatures

The investigation of the mechanical properties of the mixer unit with vibration tests resulted in a design with very high resistibility against mechanical stress. Within the qualification test program, the Quality Models have been tested at the facility of the NLR (Noordoostpolder, NL) with the vibration levels described in Tab. 5.1 at cryogenic temperatures. The Qualification Models have successfully passed all tests along all three axes.

5.2 Cryogenic cycling and bakeout

One of the most crucial test conditions defined in the environmental test plan [16] is the cryogenic cycling from room temperature to 77 K and 4 K and additional cycling to $80°C$, the bakeout temperature of the Herschel cryostat.

During the mixer performance tests and the integration- and test-programs at FPU, instrument (HIFI) and satellite level, the mixer unit has to withstand a high number of cryogenic cycles (cycles needed for performance tests $\approx$

3+10 . . . 15 cycles for integration). The qualification test doubles the number of cycles to be on the save side. In addition, the instrument will be heated up to 80°C for 72 h at least once during the cryostat bakeout. Tab. 5.2 summarizes the qualification test run for the KOSMA mixer units.

Qualification test, thermal cycling	
30 cycles	RT - 77 K (LN_2)
>15 cycles	RT - 4 K (LHe)
3 cycles	RT - 82°C
dwell time = 30 min at T_{MIN} and T_{MAX}	
bakeout, 72 h	82°C

Tab. 5.2: *Thermal cycling to cryogenic temperatures and to bakeout temperatures for the qualification test program.*

In order to avoid failure due to thermal contraction and expansion, the coefficients of thermal expansion (CTE) of the different materials have to be considered. Tab. 5.3 gives an overview over most of the materials used in the mixer unit.

	Material	CTE [ppm/K]
	Al	24
Structure	Cu	17
	Steel	12. . .16
	Alumina	7.4
Boards	RT/Duroid6002	16
	TMM10	16
	Mixer chip (Quartz)	0.55
Components	ATC capacitor (CA dielectric)	10
	AVX capacitors (N0P dielectric)	8.5
	Thick film resistors (96 % Alumina chip)	7.4

Tab. 5.3: *Coefficients of thermal expansion (CTE) for various materials used in the mixer unit.*

Every material interface and every electrical connection has to be designed to hold under the test conditions. Where the difference in the CTE's is not too high, special adhesive bonds could be used. Tab. 5.4 summarizes the most critical interfaces, their characteristics and the design solutions, which enable a reliable operation.

During the design verification phase of the project, mixer noise measurements revealed a spike of the noise temperature at 7.8 GHz, just below the upper band edge of the IF band. At room temperature, no reason for the occurrence of the spike could be found. Dipstick measurements with a similar model, which was designed to fit into the small cross section of a liquid Helium can,

Interface	Charact. Feature	Design
Alumina board / AVX cap. (N0P ceramic) and resistors (Alumina)	Matched CTE	Usual solder joints (Reflow soldering by Hymec, NL)
Alumina board / Alu housing	High ΔCTE	Special clamping mechanism (see section 5.1.4)
TMM10 and RT/Duroid6002 boards, 17.5 μm Cu laminated / Alu housing	Medium ΔCTE	Gold plating of both interfaces, Ablefilm 5025E Special gluing procedure (vacuum) (see section 3.2.4)
RT/Duroid6002 board, 17.5 μm Cu laminated / ATC capacitor, bottom	Medium ΔCTE electrode	Gold plating of both interfaces, EPO-TEK H20E, special wetting procedure (XYZ-stage vacuum tweezers) (see section 3.5)
RT/Duroid6002 board, 17.5 μm Cu laminated / ATC capacitor, top side	Medium ΔCTE	Gold plating of both interfaces, $\geq$5 wedge bonds (25 μm Au) with adequate slack (by Hymec)
RT/Duroid6002 board / TMM10 board	Complex interface	Gold plating of both interfaces, $\geq$2 wedge bonds (25 μm Au) with adequate slack (by Hymec)
RT/Duroid6002 board / Habia-wire strands on SMA cable inner cond.	Complex interface, High ΔCTE	board gold plated, strands silver plated, with special geometry and adequate slack, EPO-TEK H20E, manual dispersion, (see section 5.1.5 and 3.5)
RT/Duroid6002 board / CuBe-foil on SMA jack inner cond.	Complex interface, High ΔCTE	board gold plated, flexible CuBe-foil with slack due to micro kink, EPO-TEK H20E, manual dispersion, (see section 3.4 and 3.5)
Mixer chip (quartz) / Substrate channel in mixer block (Cu)	High ΔCTE small size	Special UV-activated glue
Mixer chip electrode / Mixer block (Cu)	Complex interface	Mixer block gold plated, electrode gold plated, 2 double sided (25 μm Al) wedge bonds, with adequate slack
Mixer chip electrode / SMA jack in Mixer block	Complex interface	Mixer block gold plated, SMA inner cond. end plane gold plated, 2 wedge bonds (25 μm Al), with adequate slack

Tab. 5.4: *Thermal expansion properties of material interfaces and electrical connections. Short description of the interfaces and the design solutions, which guarantee a reliable function. "Complex interface" means in this context a multi material interface with a complex structure and different CTEs.*

could not reproduce the feature. It turned out that the small pillar, which suppresses the box resonance at 7.8 GHz and increases the EMI rejection ratio

(see section 2.7.7), lost electrical contact to the top cover of the bias-T box at low temperatures, although it was fixed with a torqued screw and the interface was gold plated on both sides. Replacing the aluminum pillar with a gold plated steel duplicate with lower thermal contraction, could reliably prevent the box resonance spike.

Another effect, which could be observed in the verification phase, was a misalignment between bias-T box and the mixer block mount which occurred after a large number of cryogenic cycles. Although the bias-T box is mounted with 3 torqued (M=35 Nm) M2 screws (stainless steel) on the mixer mount, a small tension, induced by the semi rigid SMA cable connecting the mixer block with the bias-T, was sufficient to displace the parts against each other by 0.2 mm. This is caused by the torque strength release due to the difference in the CTE of the steel screws and the Al structure of bias-T and mixer block mount. To prevent conflicts with the geometry of the mixer subassembly (MSA), it was possible to completely remove the tension by

- avoiding the tension of the SMA cable by a more accurate bending and soldering technique of the cable (for details see section 3.3).

- manual fine tuning of the cable form directly before the final assembly of the mixer unit.

- a counter force to a special hexagonal nut (for details see section 3.3) while the SMA connector is torqued during assembly. This prevents any build up of torsion in the cable.

5.3   Radiation tests

This section describes the Herschel radiation environment and presents the expected total proton fluence during the mission. From the fluences, total doses are calculated by taking into account the shielding of the cryostat walls. These doses are compared with the doses used for irradiation of SIS-devices with protons at the KVI. The beamline setup and the first experiment where SIS mixer devices have been irradiated at 4 K operating temperature is described.

5.3.1   The radiation environment of Herschel

The Herschel satellite is planned to be launched together with the Planck satellite in the beginning of the year 2008 by an Ariane 5 launcher. Both satellites are transferred to the second Lagrangian point L2 of the Sun-Earth system at about $1.5 \, 10^6 \, km$ from the Earth to the opposite side of the Sun. From the transfer orbit Herschel is injected to a large Lissajous orbit around L2, where it will be operating for about 4 years.

The journey to L2 will take 125 to 130 days. In the first phase of the transfer, the satellite and its instruments are exposed to energetic protons (up to several hundred MeV) and electrons (up to 10 MeV), which are trapped in the magnetosphere of the Earth. Because the flight through the radiation belt is very short in comparison to the overall mission duration, the effects of the trapped particles can be neglected.

When the spacecraft leaves the magnetotail of the Earth, which may extend up to $600\,000 \, km$ into space, it will fully be exposed to galactic cosmic rays (GCR) and solar protons flares.

Although GCR include energetic heavy ions, which can deposit significant amounts of energy in sensitive volumes, the flux is very low (a few $particles/cm^2/s$). During a solar maximum, the GCRs are partly shielded by the magnetosphere of the Sun even at L2 (1.01 AU away from the Sun). The total dose, deposited in Silicon, surrounded by a 4 mm Aluminum shield, during solar minimum (GCR maximum), within 4 years, is about 49 rad(Si).

By far the highest contribution to the damage by radiation comes from energetic protons (and heavier nuclei), ejected from the Sun's surface during a solar flare. If such a flare is in the vicinity of the tracing point of a magnetic field line, connecting the Sun's surface and the spacecraft, it is likely for protons to travel along this line and arrive at the location of the satellite. Such solar proton events especially occur during the solar maximum in the solar cycle, which has a period of approximately 11 years.

A new predictive flux-transport dynamo model [54] for solar activity predicts the onset of the next cycle (cycle 24) to be in the beginning of 2008 reaching

it's peak at 2012 while being 30-50% stronger than cycle 23. (Launch date of HIFI is presently March 2008.)

5.3.2 Radiation models

Mainly two different studies about the radiation environment for the Herschel spacecraft were published: "FIRST L-2 Radiation Environment" by ESA/ESTEC in 1997 [55] and "Radiation Shielding Analysis of Herschel and Planck Satellites" by Alcatel Space in 2002 [56]. Unfortunately, these documents are inconsistent with each other and partially out-dated because of the delayed launch, presumably in early 2008. In order to gain confidence for this work, the results were reviewed and compared with the authors own calculations. In these calculations, the most recent models together with an updated mission schedule could be used for total mission fluence calculations. With the CREME96 program package [57], the influence of GCR has been modeled. Solar proton fluences were predicted using the JPL-91 model [58] and the more resent ESP model (Emission of Solar Protons) [59], implemented in the program package SPENVIS [60].

The obtained data show good consistence with total fluence calculations by NASA for the Next Generation Space Telescope (NGST) published in [61]. Just as Herschel, the NGST will be positioned in L2. It is expected to be launched in mid 2009 and to observe for 5 to 10 years.
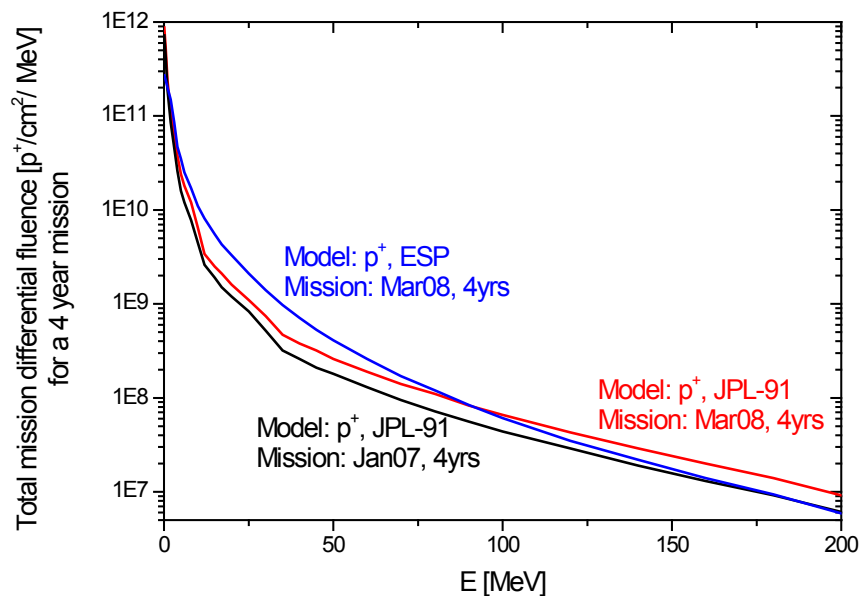

Fig. 5.7: *Total mission differential fluence $[p^+/cm^2/MeV]$ for a 4 year mission. Calculated for two different launch dates and two different models. The most realistic assumption is made in the ESP model with a launch date on March 2008.*

Fig. 5.7 shows the spectral intensity distribution of the solar proton fluence

for a 4 year mission for two different launch dates (January 2007 and March 2008) and evaluated with the JPL-91 model and the ESP model. All fluence and dose data have been calculated for a 95% confidence level that the actual radiation will not exceed these values.

In order to appreciate the influence of the radiation, it is necessary to account for the shielding of the Herschel cryostat vacuum vessel (CVV). The CVV has a 3 mm Aluminum outer shell. Alcatel Space calculates a total mission dose of $1.56\,k\,rad(Si)$ at the Focal Plane Unit (FPU) location in the cryostat. In the underlying radiation model, this corresponds to an effective shielding of 4 mm Al due to the cryostat together with the telescope mirror and the other surrounding instruments (See Fig. 5.8). The shielding influence for the updated mission schedule was calculated with SPENVIS in the Aluminum Sphere Model and compared to the Alcatel Space data.
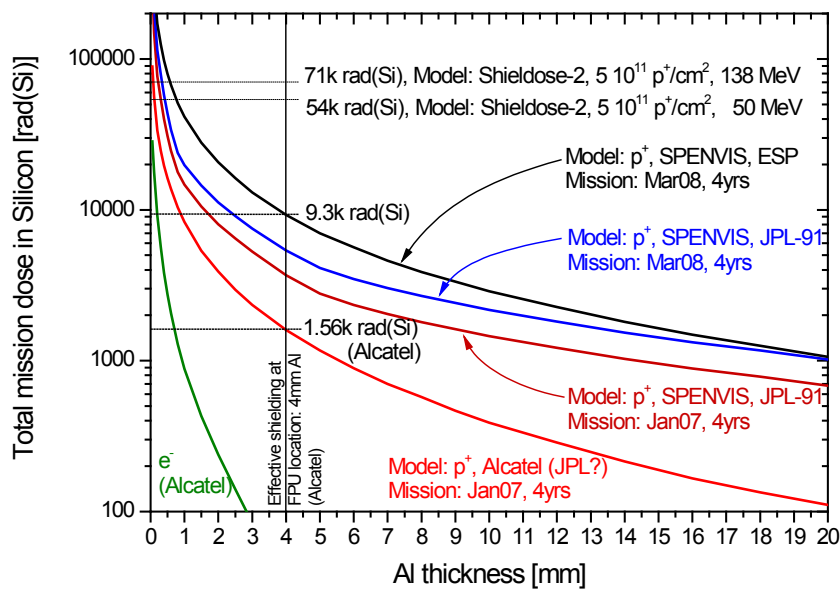
Fig. 5.8: *Total mission dose deposited in a Silicon target, shielded with Aluminum in [rad(Si)]. For the 4 mm Al effective thickness of the Herschel cryostat, the most realistic model (ESP, launch in March 2008, black line) yields in a dose, which is 6 times higher than the dose calculated by Alcatel for a launch in Jan. 2007 [55].*

The results for the different models and mission data can be compared with each other by means of the total mission dose (in *rad*, *radiation absorbed dose*, $1\,rad = 0.01\,J/kg$) in a Silicon target as a standard absorber. This also allows to compare the results with the (monoenergetic) proton radiation doses applied to the samples at the Kernfysisch Versneller Instituut (KVI) facility. These calculations have been carried out with the program SHIELDOSE-2 [62]. In Tab. 5.5, the doses have been summarized for different launch dates and radiation models for the effective 4 mm Al shielding of the cryostat.

Launch date	Radiation model	Absorber material	Total dose in $k\,rad$
Jan. 2007	Alcatel Space, solar p^+ (JPL)	Si	1.56
Jan. 2007	SPENVIS p^+ (JPL-91)	Si	3.69
Mar. 2008	SPENVIS p^+ (JPL-91)	Si	5.37
Mar. 2008	SPENVIS p^+ (ESP)	Si	9.27
Mar. 2008	SPENVIS p^+ (ESP)	Al	9.04
Mar. 2008	SPENVIS p^+ (ESP)	SiO_2	9.74
Solar Min.	CREME96, Gal. Cosmic Rays	Si	0.049
Jan. 2007	Alcatel Space, trapped e^- (AE8)	Si	0.032
Jan. 2007	Alcatel Space, trapped p^+ (AP8)	Si	0.002
KVI	cyclotron $5\,10^{11}\,p^+/cm^2$, 50 MeV	Si	53.95
KVI	cyclotron $5\,10^{11}\,p^+/cm^2$, 138 MeV	Si	70.33

Tab. 5.5: *Total dose in Si (behind a 4 mm Al shield) calculated with different models for different launch dates. The most realistic model (ESP, launch in March 2008) is evaluated for Si, SiO_2 and Al with very similar results. The dose in Al_2O_3 should have a similar value. These doses are compared with the doses accumulated at the KVI facility.*

5.3.3 Mechanisms of irradiation damage

Fig. 5.9 shows the cross section of a typical $Nb/Al/Al_2O_3/Nb$-junction between the $NbTiN$ bottom electrode and the Nb or Al top electrode. After deposition of 8-10 nm Al on top of the Nb electrode, the surface is oxidized with pure O_2 at a pressure of up to 6 Pa for about 10 min at room temperature. This results in an insulating layer with a thickness of 1-2 nm, corresponding to 3-5 unit cells Al_2O_3. This thin insulating layer is considered to be the radiation sensitive part of an SIS mixer device.

The first proton irradiation experiment with Nb SIS-junctions is reported by King et al. (1991) [63]. Pagano et al. [64] published a similar experiment at a different proton energy in 1997. They used Nb-junctions for digital logic circuits based on the hysteretic properties of Josephson junctions. They observed only slight changes of the I(V)-curve even at very high proton fluences of up to $10^{15}\,p^+/cm^2$ at 63 MeV [63] and 6.5 MeV [64].

SIS-junctions for logic circuits are fabricated with much smaller current densities (typically $60\,A/cm^2$ [64] and higher quality factors by strong oxidation of the Al layer. In contrast, the junctions used for heterodyne mixing have high current densities around $10 - 15\,kA/cm^2$ in order to achieve a large RF bandwidth. These current densities are obtained by much shorter oxidation time, resulting in a much thinner oxide barrier, which may result in a higher sensitivity to radiation induced point defects. Such point defects can occur if atoms of the insulating layer are displaced from their lattice sites, forming vacancy-interstitial pair defects [65]. Furthermore, metal atoms may be injected by radiation into the thin Al_2O_3 barrier forming bridges or weak
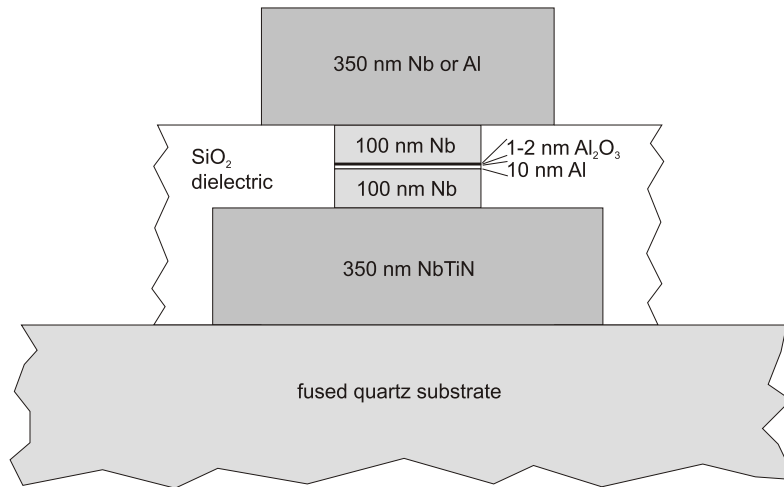
Fig. 5.9: *Cross section of the mixer chip through the SIS-junction. The sensitive area is not only the 1-2 nm Al_2O_3 barrier, but also its surroundings from where metal ions can diffuse into the barrier under the influence of radiation.*

links across the barrier. The reduced height of the tunnel barrier may result in local shifts of the fermi level, which would reduce the sharpness of the I(V)-curve or reduce the gap voltage [63]. This degradation of the I(V)-curve would result in increased losses in the mixing process. Another possible consequence is an increased barrier leakage, which would result in an increased sub-gap current and thus increased shot noise contributions to the overall receiver noise temperature.

The energy loss of ions passing through the target can roughly be divided into nuclear stopping (energy loss to the mediums nuclei) and electronic stopping (energy loss to the bound electrons). The latter being by far the dominating effect because of the high probability of a collision due to the ubiquitous abundance of the electrons. While the energy transfer to the light electrons is much smaller, the inelastic scattering on a core may transport high amounts of energy into the crystal lattice.

Modern computer programs calculate the linear energy transfer (LET, dE/dx) with the Bethe-Bloch equation describing the inelastic coulomb scattering of ions on bound electrons of the target atoms. With higher order corrections of the Bethe-Bloch equation and ray tracing, it is possible to calculate the energy transfer within a few percents [66].

Unfortunately, in the SPENVIS package no data for Al_2O_3 as target material is available. But the dose rates in Al_2O_3 should not be very different from those in *Si* (Z=14, $\rho = 2.3\,g/cm^3$), *Al* (Z=13, $\rho = 2.7\,g/cm^3$) or SiO_2 ($\rho = 2.2\,g/cm^3$). For comparison, the total mission doses for *Al* and SiO_2 are included in Tab. 5.5.

5.3.4 Experiments at the KVI facility

The experiment performed at the Kernfysisch Versneller Instituut (KVI) in Groningen (NL) was the first irradiation of SIS-junctions used for heterodyne mixing (with a thin oxide barrier). The radiation hardness of different SIS-junctions, hot electron bolometers (HEB) from Chalmers, Sweden, and HEMT transistors used for low noise amplifiers from CAY (Centro Astronómico de Yebes, Spain) has been investigated. As proton source the superconducting cyclotron AGOR, which accelerates protons up to 190 MeV, was used.
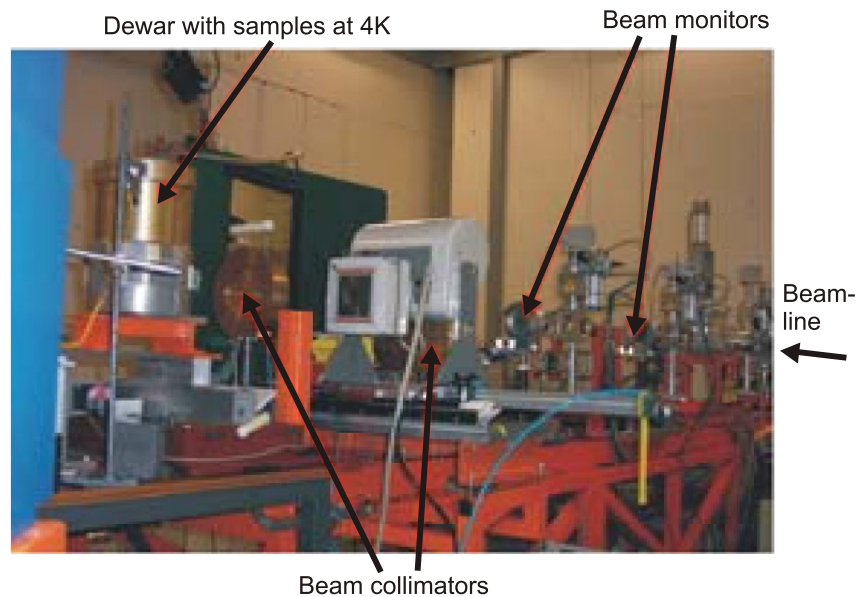
Fig. 5.10: *The AGOR beamline. The p^+ beam enters the beamline from the right and passes through the Tungsten foil, the beam monitors and the collimators, penetrates the Dewar wall and irradiates the samples.*

In Fig. 5.10 the experimental setup at the AGOR beamline is depicted, showing the dewar with the samples, beam collimators and beam monitors. The beam passes through a monitor ionization chamber and is then expanded by means of a Tungsten foil. The collimator forms a $2 \times 2\,cm^2$ beam. The uniformity of the beam was checked before the irradiation experiment.

During the whole test, the samples were cooled to 4.2 K in a liquid He wet cryostat. Keeping the devices at operating temperature, enables a realistic assessment of the radiation damage because annealing effects, which might occur at higher temperatures, [67] are avoided.

We exposed the samples to 50 MeV and 138 MeV proton beams with a flux of $10^7\,p^+/cm^2/s$ in order to investigate radiation damage at different energies. We subsequently accumulated a total fluence of $10^9\,p^+/cm^2$, $10^{10}\,p^+/cm^2$,

$10^{11}\,p^+/cm^2$ and $5\ 10^{11}\,p^+/cm^2$. Directly after each exposure, the I(V)-curves of the junctions have been recorded. More than 20 SIS-junctions with both Al and Nb top electrodes have been irradiated. During the exposures, it was possible to continuously monitor the I(V)-characteristics of one arbitrary SIS-junction in order to observe possible single event upsets. The junction was biased at 2 mV and a digital oscilloscope was used to monitor possible current spikes. Even at high dose rates, no such event, which would be the result of a highly localized energy deposition in the junction, could be observed. A detailed description of the experiment is given in [68].

The I(V)-curves, recorded directly after the application of different doses, did not show any change, which could be attributed to radiation effects. Merely slight changes due to magnet field influences in the noisy environment of the accelerator could be observed. Similar observations were reported in [63]. A repeated measurement after a new cool down of the samples confirmed these observations.

Chapter 6

Directional couplers for IF signal processing

Directional couplers can for example be used in sideband separating mixers and in balanced low noise amplifiers. This makes them very useful as a part of receivers for radio astronomy. Within this part of the thesis, directional couplers with good performance over a very large bandwidth were developed. A nonuniform stripline design is used to ensure TEM mode propagation. By the smooth change of the electrical parameters, uncontrolled reflections are avoided. The author developed a design procedure, which includes an appropriate mix of analytic calculations and an interpolation scheme, which uses results from the CST MWS 2D solver in order to calculate the actual geometry from even mode line impedances. The design of a -3 dB coupler from 1.9 GHz to 9.3 GHz and a -17 dB coupler with a bandwidth from 0.75 GHz to 10.1 GHz is presented.

6.1   Applications for directional couplers

In the next subsections, the use of -3 dB broadband couplers in sideband separating mixers and balanced amplifiers is described. Special attention is given to performance criteria for the coupler in the particular application.

6.1.1   Sideband separating mixers (2SB mixers)

When the noise temperature of SIS mixers approaches its fundamental quantum mechanical limits [69], there are still possibilities to increase receiver sensitivity by using both polarization directions of the incoming signal. If one likes to further improve sensitivity, one may use sideband separation or suppression. The aim of the KOSMA mixer group is to contribute with a sideband

separating mixer array for 345 GHz, which has to be build within the Ra-
dioNet contract. (RadioNet is an Integrated Infrastructure Initiative, funded
under the European Commission's Sixth Framework Programme (FP6) in or-
der to enhance the quality and quantity of science, performed by European
astronomers. [70])

When the input signal and the LO signal are mixed in an SIS-junction, the
signals are multiplied with each other and both the signal and the image
band are mixed down to the IF band (double sideband mixer, DSB mixer). If
the mixers image response is unwanted, it can be either eliminated by filter-
ing out the image band (image enhanced mixer, sideband suppression mixer,
SSB mixer) or by separating the USB from the LSB (sideband separating
mixer, two sideband mixer, 2SB mixer).

The image enhanced mixer can be implemented by placing a cold filter ele-
ment in front of the mixer, which attenuates the image band and does not
contribute any noise because of its low temperature. At mm-wavelength, usu-
ally a quasi optical diplexer (e.g., Martin-Pupplet interferometer) with high
Q-factor is used as image rejection filter. Besides the large dimensions of
such a filter, this method has the disadvantage that the filter has to be (me-
chanically) tuned with the LO frequency, which may be difficult, especially if
the filter is installed in the cryostat.

Another elegant, but likewise challenging possibility, is to separate the USB
and the LSB and deliver the sidebands at two different IF connectors at the
output of a 2SB mixer. The functional principle is explained in the next
section.

Both the SSB and the 2SB mixers offer a lot of advantages compared to a
usual DSB mixer.

Measuring a sideband separated from the other, enables a clear assignment
of spectral lines to the sideband and thus to a unambiguous frequency. This
may be useful in particular in galactic line surveys, where a high line density
can be expected.

The increase of receiver sensitivity is due to suppression of unwanted noise
of the atmosphere and the warm telescope optics coming through the image
sideband. The image band is terminated by a cold RF load rather then by
the sky, which may have a much higher effective temperature (as it is the
case in DSB receivers). This further improves the calibration of the receiver
because the response to atmospheric noise (and to the broadband calibration
load signal) is through one sideband only.

Furthermore, the 2SB mixer has the advantage that both the USB and the
LSB IF ports can be connected to a signal processing chain, which enables
simultaneous observation in both sidebands.

Thus, sideband separation offers a lot of advantages, which are worth sub-
stantial development and fabrication effort. A detailed analysis of 2SB vs.

DSB observing efficiency is given in [15].

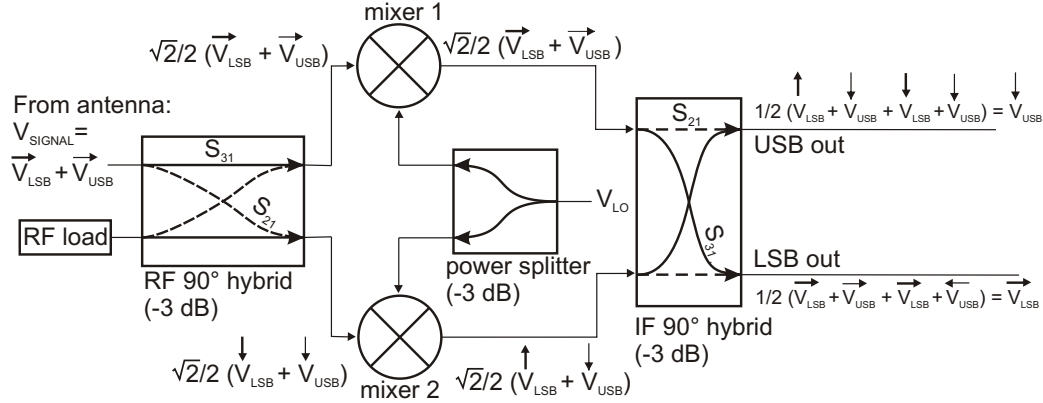## 6.1.2 Operation mode of 2SB mixers

Fig. 6.1: *Schematic of a 2SB mixer. The signal ($V_{USB} + V_{LSB}$) enters the RF 90° hybrid from the left. The relative phases (arrows) and the amplitudes are indicated separately for LSB and USB. In both -3 dB 90° hybrids (RF and IF), the signal is split. The signal part which is coupled to an output port (dashed lines) has always a −90° phase shift in comparison to the part of the signal which directly passes the coupler.*
Arrow notation: →= 0°, ↓= 90°, ←= 180°, ↑= 270°)

In the following, the operation of a sideband separating mixer is explained with the functional block diagram shown in Fig. 6.1.

The signal, consisting of USB and LSB, is split in the -3 dB RF 90° hybrid and one branch is phase shifted relatively to the other by −90°. These signals are fed to two separate SIS-mixers, which are pumped with an LO signal, which has the same phase for both mixers. The resulting IF signal amplitudes and phases can be calculated with theorems for trigonometric functions. In mixer 1, the signal and LO voltages are multiplied the following way (arrow notation explained in Fig. 6.1):

$$
\begin{aligned}
USB : \quad & \cos(\omega_{LO}t)\cos((\omega_{LO} + \omega_{IF})t) \\
= \quad & 1/2\cos(-\omega_{IF}t) + 1/2\cos((\omega_{2LO} + \omega_{IF})t) \\
\Rightarrow \quad & IF : \cos(-\omega_{IF}t) = \cos(\omega_{IF}t) = " \rightarrow "
\end{aligned}
$$

$$(6.1)$$

$$
\begin{aligned}
LSB : \quad & \cos(\omega_{LO}t)\cos((\omega_{LO} - \omega_{IF})t) \\
= \quad & 1/2\cos(\omega_{IF}t) + 1/2\cos((\omega_{2LO} - \omega_{IF})t) \\
\Rightarrow \quad & IF : \cos(\omega_{IF}t) = " \rightarrow "
\end{aligned}
$$

In mixer 2 the −90° phase shift of the signal changes the situation. With $\cos((\omega_{LO} \pm \omega_{IF})t + 90°) = \sin((\omega_{LO} \pm \omega_{IF})t)$, one obtains a 180° phase

difference of USB and LSB:

$$
\begin{aligned}
USB : \quad & \cos(\omega_{LO}t)\,\sin((\omega_{LO}+\omega_{IF})t) \\
= \quad & 1/2\sin(-\omega_{IF}t)+1/2\sin((\omega_{2LO}+\omega_{IF})t) \\
\Rightarrow \quad & IF : \sin(-\omega_{IF}t) = \cos(\omega_{IF}t-90^\circ) = " \downarrow "
\end{aligned}
$$

$$
\begin{aligned}
LSB : \quad & \cos(\omega_{LO}t)\,\sin((\omega_{LO}-\omega_{IF})t) \\
= \quad & 1/2\sin(\omega_{IF}t)+1/2\sin((\omega_{2LO}-\omega_{IF})t) \\
\Rightarrow \quad & IF : \sin(\omega_{IF}t) = \cos(\omega_{IF}t+90^\circ) = " \uparrow "
\end{aligned}
\tag{6.2}
$$

When these mixer IF signals are recombined with a -3 dB 90° hybrid, one obtains the separated USB and LSB signals at the output ports by constructive and destructive summation (see Fig. 6.1).

It is possible to achieve 2SB operation also by interchanging the RF hybrid and the RF power splitter. However, the advantage of the configuration described above is that the mixers are isolated from each other by the 90° hybrid over the RF signal path. The mutual interference via the LO path (the power splitter) may be improved by placing attenuators between the mixer and the power splitter without decreasing the mixer performance. Another advantage is that standing waves in the telescope optics are avoided because the optics is effectively terminated by the broadband RF load rather then by the mismatched, frequency dependent junction impedance.

6.1.3   Sideband separation ratio (SSR)

An important quantity, which is influenced by the performance of the IF hybrid, is the sideband separation ratio (SSR):

$$
SSR(\omega) = \frac{P_{Image(\omega)}}{P_{Signal(\omega)}}
\tag{6.3}
$$

When the RF hybrid has a power and phase imbalance, one may describe this by a factor

$$
A(\omega) = \frac{V_{M1}}{V_{M2}} = A_0(\omega)\,e^{i\phi(\omega)}
\tag{6.4}
$$

In the ideal case $A_0(\omega) = 1$ and $\phi(\omega) = -90^\circ$. Small asymmetries in the other waveguide structures and the mixing elements may also have an effect to $A(\omega)$. With this complex voltage ratio, it is possible to describe the image separation capabilities of the mixer unit in terms of the complex S-parameters of the IF hybrid:

$$
SSR(\omega) = \frac{P_{Image(\omega)}}{P_{Signal(\omega)}} = \frac{|S_{21}(\omega)+S_{31}(\omega)\,A(\omega)|^2}{|S_{31}(\omega)+S_{21}(\omega)\,A(\omega)|^2}
\tag{6.5}
$$

where $S_{21}(\omega)$ and $S_{31}(\omega)$ are the S-parameters for the coupled and the direct path in the IF hybrid respectively. With an ideal RF hybrid, the best performance is obviously obtained if the S-parameters satisfy the following amplitude and phase relations $\mathrm{abs}(S_{21}(\omega)/S_{31}(\omega)) = 1$ and $\arg(S_{21}(\omega)/S_{31}(\omega)) = -90°$, which are the same as for the RF hybrid.

6.1.4 Balanced amplifiers

The IF impedance of an SIS-junction strongly depends on LO frequency, pump level and IF frequency. If such a poorly matched source is connected to the input of a low noise amplifier via an electrically long cable, the input impedance of the amplifier needs to be well matched to the transmission line. Otherwise multiple reflections cause standing waves and, thus, ripple in the receiver gain over the IF frequency band.

The best way to eliminate standing waves is to place an isolator between mixer and amplifier. In addition to the reduction of standing waves, this configuration has the advantage that possible noise waves, coming from the input of the amplifier, are absorbed by the isolator termination. Unfortunately, sufficient isolator performance can be obtained only over an octave bandwidth up to now (4–8 GHz, Pamtech Isolator for HIFI). Isolators with higher bandwidths are available only at the cost of high signal attenuation (4–12 GHz, -1.7 dB, Pamtech Isolator for ALMA). In addition, the procurement of cryogenically coolable broadband isolators is difficult.

Another possibility is to use a balanced amplifier, which can maintain a good match over a very broad bandwidth in dependency of the performance of the 90° hybrid at the input of the amplifier. (For a detailed comparison of noise properties of balanced amplifiers versus isolator configuration, see [71].) A functional block diagram is depicted in Fig. 6.2.
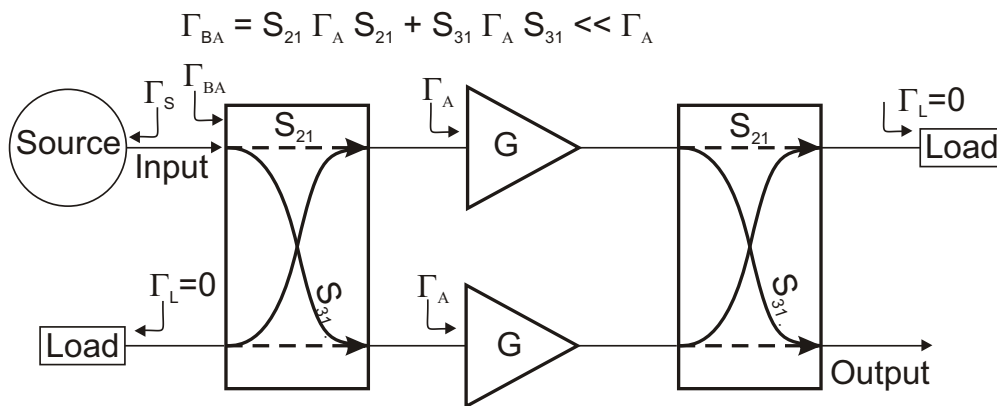

Fig. 6.2: *Schematic of a balanced amplifier for the calculation of the reflection coefficient at the input port of the amplifier.*

The balanced amplifier employs two quadrature hybrids for input and output. Any reflections of an incident signal on the input due to the poor match Γ_A of the amplifiers will be channeled back through the hybrid to the $50\,\Omega$ load, where they will be absorbed. Signals traveling back to the source have $180°$ phase difference and cancel out provided that the hybrid is ideal and the transistor input stages have equal reflection coefficients. (The same argumentation can be used for the output.) Therefore, the source is effectively terminated in the $50\,\Omega$ load and standing waves can be avoided over the whole bandwidth of the quadrature hybrid.

For a non ideal hybrid, the overall reflection coefficient of the input can be expressed as follows:

$$\Gamma_{BA} = S_{21}\Gamma_A S_{21} + S_{31}\Gamma_A S_{31} = C_{BA}\Gamma_A \ll \Gamma_A \tag{6.6}$$

In addition to the improved input match, the balanced amplifier provides some other benefits:

- The amplifier stability is increased because the amplifier is always terminated by $50\,\Omega$ at its terminals regardless of changes in the source and load impedance. (This relaxes the need for unconditional stability as an amplifier design criterion [72].)

- The gain of a BA is increased by $+3\,dB$ compared to a single stage amplifier ($G_{BA} = 2\,G_A$). The same is true for the $1\,dB$ compression point.

- The redundancy of the balanced amplifier minimizes the probability of a hard failure. I.e., if one of the two amplifiers were to fail, the entire amplifier will still be operational, but with degraded performance.

The main drawback of a BA is the power required for two amplifiers instead of one. This power is dissipated in the transistors and must be drained by the cryostat cooling mechanism. The power consumption of cryogenic LNAs can be reduced by using InP- instead of GaAs-HEMTs.

6.2   Theory of nonuniform coupled lines

As already mentioned in the introduction to this chapter, a nonuniform stripline design is used here in order to achieve good coupling performance over a very large bandwidth. Such couplers are needed in order to build astronomical receivers with a large IF bandwidth.

This section delves into the theory of nonuniform coupled lines. In this context, nonuniform means that the impedance (and the geometric shape of the

lines) varies continuously over the length of the lines. It is shown that the differential equation describing symmetric, nonuniform coupled lines can be reduced to a differential equation for a single nonuniform line. This differential equation for a single line is well understood because it has formal analogy with the Schrödinger equation. The solution of the equation relates the even mode line impedance $Z_e(z)$ to the Fourier transform of the coupling bandshape.

6.2.1 The analogy of ideal symmetric nonuniform couplers with nonuniform transmission lines

In this section, an analogy between nonuniform couplers and single nonuniform transmission lines is established, following a derivation of C.B. Sharpe [73]. It is shown that the differential equations describing a nonuniform coupler can be reduced to those describing a single nonuniform line, provided that the coupler shows perfect isolation and zero reflection at the input port. The differential equations, relating currents and voltages on nonuniform coupled lines, are simplified, rewritten for electrical length rather than physical length and normalized to $1\,\Omega$. From the desired coupler characteristics, the boundary conditions at the endings of the coupler are derived. These boundary conditions lead to two independent solutions. Combining these solutions leads to separation into two independent equations for single nonuniform lines. To illustrate the argumentation, the reader is referred to Fig. 6.3.
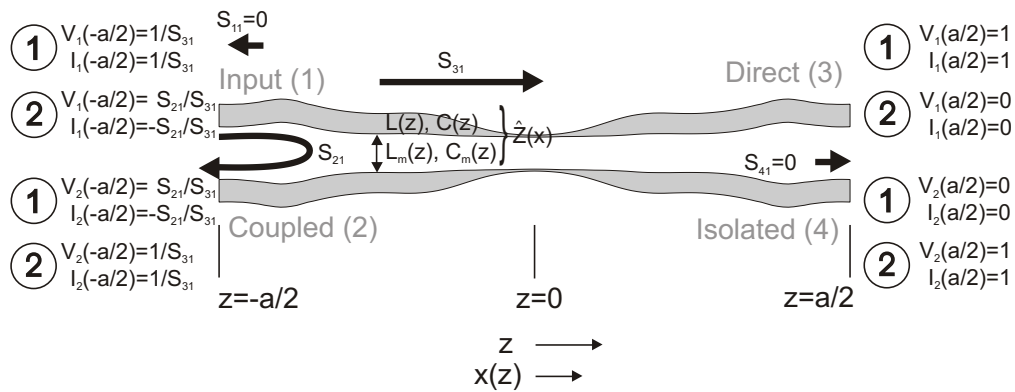

Fig. 6.3: *Nonuniform coupled lines with all relevant electrical parameters. Boundary conditions for two independent solutions marked with ① and ②.*

The behavior of two coupled, lossless TEM transmission lines is described in

general by the following set of differential equations:

$$\frac{dV_1}{dz} = -i\omega L_1 I_1 - i\omega L_m I_2$$

$$\frac{dV_2}{dz} = -i\omega L_2 I_2 - i\omega L_m I_1$$

$$\tag{6.7}$$

$$\frac{dI_1}{dz} = -i\omega C_1 V_1 - i\omega C_m V_2$$

$$\frac{dI_2}{dz} = -i\omega C_2 V_2 - i\omega C_m V_1$$

where L_j and C_j are series-inductances and shunt-capacitances per unit length of the lines ($j = 1, 2$). L_m and C_m describe inductive and capacitive coupling per unit length. Here the discussion is restricted to symmetric couplers $L_j = L$ and $C_j = C$.

If the fields of the propagating waves are perpendicular to the propagation direction z (e.g., TEM mode), one can assume simple local functions $L = L(z)$, $C = C(z)$, $L_m = L_m(z)$, $C_m = C_m(z)$ of the electric parameters of the coupler. One may rewrite the above system of differential equations using a more compact matrix formulation:

$$\frac{d\mathbf{V}(z)}{dz} = -i\omega \mathbf{L}(z)\mathbf{I}(z)$$

$$\tag{6.8}$$

$$\frac{d\mathbf{I}(z)}{dz} = -i\omega \mathbf{C}(z)\mathbf{V}(z)$$

where

$$\mathbf{V}(z) = \begin{pmatrix} V_1(z) \\ V_2(z) \end{pmatrix}, \mathbf{I}(z) = \begin{pmatrix} I_1(z) \\ I_2(z) \end{pmatrix} \tag{6.9}$$

and

$$\mathbf{L}(z) = \begin{pmatrix} L(z) & L_m(z) \\ L_m(z) & L(z) \end{pmatrix}, \mathbf{C}(z) = \begin{pmatrix} C(z) & C_m(z) \\ C_m(z) & C(z) \end{pmatrix} \tag{6.10}$$

The symmetry of the coupler also implies that the wave propagation velocity is equal on both lines:

$$v_1(z) = v_2(z) = v(z) = 1/\sqrt{L(z)C(z) + L_m(z)C_m(z)} \tag{6.11}$$

The velocity can be used to define the electrical length of the coupler

$$x(z) = \int_0^z \frac{d\tilde{z}}{v(\tilde{z})} \tag{6.12}$$

The electrical length can be interpreted as the signal travel time ($\dim(x) = time$) for the distance z. Because $v > 0$, $x \leftrightarrow z$ is a one to one relation and we can write $\mathbf{V}(x) = \mathbf{V}(z(x))$ and

$$\frac{d\mathbf{V}(z(x))}{dz} = \frac{d\mathbf{V}(z(x))}{dx}\frac{dx}{dz} = \frac{d\mathbf{V}(x)}{dx}\frac{1}{v} \tag{6.13}$$

With the expression for the characteristic impedance $\mathbf{Z}(x) = \mathbf{L}(x)^{1/2}\mathbf{C}(x)^{-1/2}$, the above matrix differential equation can be formulated in a more symmetric form:

$$\frac{d\mathbf{V}(x)}{dx} = -i\omega\mathbf{Z}(x)\mathbf{I}(x)$$

$$\tag{6.14}$$

$$\frac{d\mathbf{I}(x)}{dx} = -i\omega\mathbf{Z}^{-1}(x)\mathbf{V}(x)$$

In order to give an easy interpretation of the boundary conditions, all for ports of the coupler should be terminated with the same impedance Z_0. This is not a loss in generality: Once a complete set of S-parameters normalized to Z_0 of the coupler is calculated, it is easy to determine it's behavior for different terminating impedances because the coupler is a lossless linear network.

With the transformations

$$\hat{\mathbf{V}}(x) = \mathbf{Z}_0^{-1/2}\mathbf{V}(x) \tag{6.15}$$

$$\hat{\mathbf{I}}(x) = \mathbf{Z}_0^{1/2}\mathbf{I}(x) \tag{6.16}$$

$$\hat{\mathbf{Z}}(x) = \mathbf{Z}_0^{-1/2}\mathbf{Z}(x)\mathbf{Z}_0^{-1/2} \tag{6.17}$$

one obtains the above set of differential equations normalized to a terminating impedance of $1\,\Omega$:

$$\frac{d\hat{\mathbf{V}}(x)}{dx} = -i\omega\hat{\mathbf{Z}}(x)\hat{\mathbf{I}}(x)$$

$$\tag{6.18}$$

$$\frac{d\hat{\mathbf{I}}(x)}{dx} = -i\omega\hat{\mathbf{Z}}^{-1}(x)\hat{\mathbf{V}}(x)$$

Now the desired coupling characteristics $S_{21}(\omega)$ may be chosen. The other relevant S-parameters are $S_{11}(\omega) = 0$ (no reflection at the input port), $S_{41}(\omega) = 0$ (perfect isolation) and $S_{31}^2(\omega) = 1 - S_{21}^2(\omega)$ (follows from energy conservation with $P_{IN} = 1$). Subsequently the boundary conditions may be derived from these S-parameters. Two possible boundary conditions which lead to two independent solutions of equation 6.18 are illustrated in Fig. 6.3.

The boundary conditions of the first solution $\hat{V}^{(1)}$ are marked with ①. If the voltage of the direct output port is set to $\hat{V}_1^{(1)}(a/2) = 1V$ and the voltage at the isolated port is set to $\hat{V}_2^{(1)}(a/2) = 0V$, one obtains with the desired S-parameters for the input port $\hat{V}_1^{(1)}(-a/2) = 1V/S31$ and for the coupled port $\hat{V}_2^{(1)}(-a/2) = \frac{1VS21}{S31}$. The boundary conditions of the second independent solution $\hat{V}^{(2)}$ are obtained by interchanging the voltage levels between adjacent ports (Fig. 6.3, boundary conditions marked with ②).

Adding and subtracting the two independent solutions results in the separation of the matrix transmission line equations into two scalar equations:

$$\frac{d}{dx}(\hat{V}_1^{(1)}(x) \pm \hat{V}_1^{(2)}(x)) = -i\omega(\hat{Z}_{11}(x) \pm \hat{Z}_{12}(x))(\hat{I}_1^{(1)}(x) \pm \hat{I}_1^{(2)}(x))$$

$$(6.19)$$

$$\frac{d}{dx}(\hat{I}_1^{(1)}(x) \pm \hat{I}_1^{(2)}(x)) = -i\omega(\hat{Y}_{11}(x) \pm \hat{Y}_{12}(x))(\hat{V}_1^{(1)}(x) \pm \hat{V}_1^{(2)}(x))$$

where $\hat{Y}(x)_{11}$ and $\hat{Y}(x)_{12}$ are elements of $\hat{\mathbf{Y}}(x) = \hat{\mathbf{Z}}^{-1}(x)$.

By using the definitions $\hat{V}^{\pm} = \hat{V}_1^{(1)}(x) \pm \hat{V}_1^{(2)}(x)$, $\hat{I}^{\pm} = \hat{I}_1^{(1)}(x) \pm \hat{I}_1^{(2)}(x)$, $\hat{Z}^{\pm} = \hat{Z}_{11}(x) \pm \hat{Z}_{12}(x)$ and $\hat{Y}^{\pm} = \hat{Y}_{11}(x) \pm \hat{Y}_{12}(x) = 1/\hat{Z}^{\pm}$, the equations (6.19) can be rewritten in the form

$$\frac{d\hat{V}^{\pm}(x)}{dx} = -i\omega\hat{Z}^{\pm}(x)\hat{I}^{\pm}(x)$$

$$(6.20)$$

$$\frac{d\hat{I}^{\pm}(x)}{dx} = -i\omega\hat{Y}^{\pm}(x)\hat{V}^{\pm}(x)$$

with the corresponding boundary conditions

$$\hat{V}^{\pm}(x = -a/2) = \frac{1 \pm S_{21}}{S_{31}} \quad , \quad \hat{V}^{\pm}(x = a/2) = 1$$

$$(6.21)$$

$$\hat{I}^{\pm}(x = -a/2) = \frac{1 \mp S_{21}}{S_{31}} \quad , \quad \hat{I}^{\pm}(x = a/2) = 1$$

(6.20) and (6.21) describe two nonuniform transmission lines (one "+"line and one "−"line) with electrical characteristics represented by $\hat{Z}^{\pm}(x)$ and $\hat{Y}^{\pm}(x)$ (series-impedance and shunt-admittance per unit length respectively). Each nonuniform transmission line is terminated in $1\,\Omega$ and possesses the S-parameters $S_{21}(\omega)$ for the reflection at the input port and $S_{31}(\omega)$ for the transmission through the lines. Hence a symmetric coupler with zero reflection at the input port $S_{11} = 0$ and perfect isolation $S_{41} = 0$ can be described in analogy to a single nonuniform transmission line.

By choosing the coupling characteristics $S_{21}(\omega)$, the boundary condition $V^+(-a/2, \omega)$ is characterized and the required impedance distribution along the line $\hat{Z}^+(x)$ is uniquely determined. Analogous for $V^-(-a/2, \omega)$ and $\hat{Z}^-(x)$. Therefore, from (6.21), $\hat{V}^\pm(x = -a/2, \omega) = \hat{I}^\mp(x = -a/2, \omega)$ follows the relation between the even and odd mode impedance of the lines:

$$\hat{Z}^+(x) = 1/\hat{Z}^-(x) \tag{6.22}$$

This is a generalization of the well known matching condition for uniform couplers $Z_{EVEN}Z_{ODD} = 1$. Thus, it is sufficient to find a solution $\hat{Z}^+(x)$ for the "+"line with the desired coupling parameters.

6.2.2 Solutions for the equivalent nonuniform line

The section is dedicated to the solution of the differential equation of a single nonuniform transmission line. It is shown that the impedance distribution along the propagation direction can be calculated from the Fourier transform of the desired S-parameters.

For the solution of the differential equation (6.20) with the desired boundary conditions (6.21), describing the "+"line, theories for nonuniform transmission lines can be used. The elimination of $\hat{I}^+(x)$ leads to a single second order differential equation for $\hat{V}^+(x)$:

$$\frac{d^2\hat{V}^+(x)}{dx^2} - \underbrace{\frac{1}{2}\frac{d(\ln \hat{Z}^+(x))}{dx}}_{P(x)} - \omega^2\hat{V}^+(x) = 0 \tag{6.23}$$

Solutions for this equation are well understood because it has formal analogy with the one dimensional Schrödinger equation with the potential $P(x)$. The quantity $P(x)$ is called the logarithmic line taper. For weak coupling $S_{21}(\omega) \ll 1$ (e.g., low backscattering of the analog single transmission line and, thus, only slow variations of $\ln(\hat{Z}^+(x))$), a solution for (6.23) and boundary condition (6.21) can be derived [74]. This results in:

$$S_{21}(\omega) \stackrel{S_{21}(\omega)\ll1}{=} C(\omega) = \int_{-a/2}^{a/2} e^{-2i\omega x}P(x)dx \tag{6.24}$$

With other words: The logarithmic line taper $P(x)$ and thus the even mode impedance distribution $\hat{Z}^+(x)$ is related to the boundary condition $S_{21}(\omega)$ by a Fourier transformation.

Because only symmetric couplers ($\hat{Z}^+(x) = \hat{Z}^+(-x)$) are considered here, $P(x)$ is an odd function and (6.24) can be rewritten using this symmetry:

$$S_{21}(\omega) \stackrel{S_{21}(\omega)\ll1}{=} C(\omega) = \int_{-a/2}^{a/2} \sin(-2\omega x)P(x)dx \tag{6.25}$$

For weak coupling, we can set $S_{21}(\omega) = C(\omega)$. In order to build couplers with higher coupling coefficient, it is necessary to increase the logarithmic taper and the above relation is not longer valid. Youla's formulation [75] of the scattering problem leads to a second order expression for $S_{21}(\omega)$:

$$S_{21}(\omega) = \frac{C(\omega)}{\sqrt{1 + C(\omega)^2}} \tag{6.26}$$

And Bergquist [76] states an exact closed form solution:

$$S_{21}(\omega) = \frac{C(\omega) + C(\omega)^3/3! + C(\omega)^5/5! + \dots}{1 + C(\omega)^2/2! + C(\omega)^4/4! + \dots} = \tanh(C(\omega)) \tag{6.27}$$
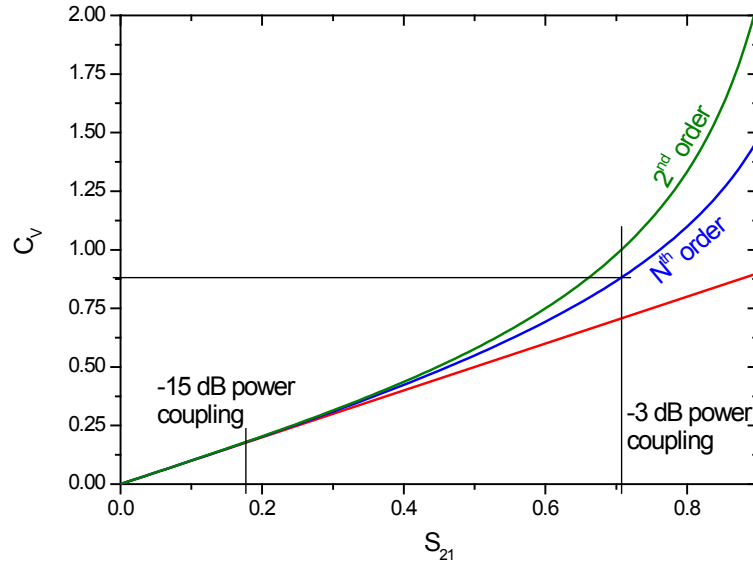

Fig. 6.4: *Voltage coupling coefficient C_V in dependence of the desired S_{21} for 1st, 2nd and N^{th} order coupling. While for a -15 dB coupler the C_V values are almost identical, for the -3 dB coupler the Nth order coupling should be used ($C_V = 0.881$).*

Now it is possible to calculate $\hat{Z}^+(x)$ by following these steps, which are illustrated in Fig. 6.5:

- Calculate $C(\omega) = \text{arctanh}(S_{21}(\omega))$ from the desired voltage coupling. (The voltage coupling and the power coupling are related by $P(\omega) = S_{21}^2(\omega)/Z_0$, where, in this case, $Z_0 = 1$ because of the normalization in equation 6.18. For instance, 50% power coupling (-3 dB) results in $S_{21} = \sqrt{2}/2 \approx 0.707$.)

- Calculate the logarithmic line taper $P(x)$ by inverse Fourier transform:

$$P(x) = \int_0^{\omega_{MAX}} \sin(2\omega x)C(\omega)d\omega \tag{6.28}$$

- Calculate the desired $\hat{Z}^+(x)$ distribution by integration of $P(x)$:

$$\hat{Z}^+(x) = e^{2\int_{-a/2}^{x} P(\tilde{x})d\tilde{x}} \tag{6.29}$$

- In order to obtain values for a real coupler, it is necessary to renormalize the impedance $Z^+(x) = \hat{Z}^+(x)Z_0$ (compare equation 6.15) and to calculate the spacial distribution $Z_e(z) = Z^+(z) = Z^+(z(x))$.
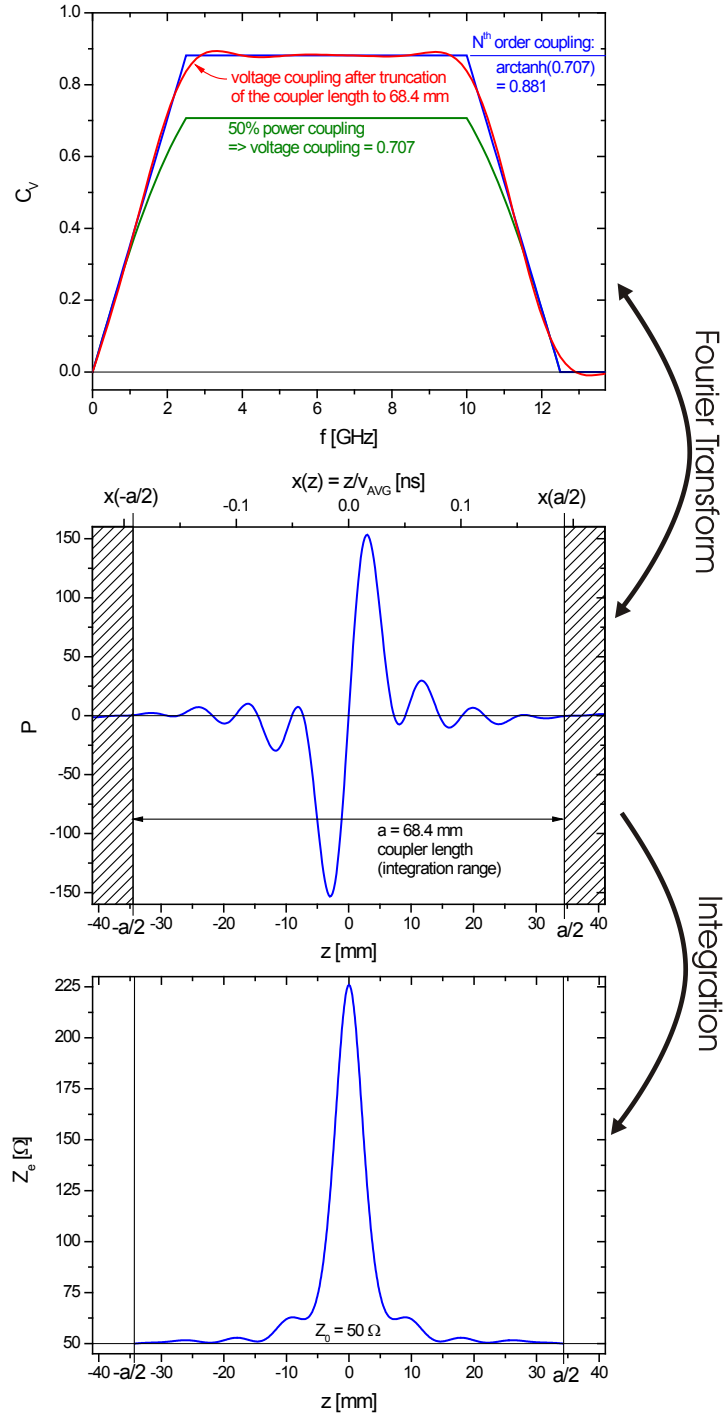
Fig. 6.5: *Illustration of the procedure for the calculation of $Z_e(z) = Z^+(z) = Z^+(z(x))$. A -3 dB coupler is used as example.*
Above: N^{th} order voltage coupling function C_V (blue) is calculated from desired voltage coupling function (green). By inverse Fourier transform of the truncated logarithmic line taper $P(x(z))$, $[-a/2 \ldots a/2]$, the actual coupling can be evaluated (red line).
Center: Logarithmic line taper $P(x(z))$ is calculated by Fourier transform of C_V
Below: $Z_e(z)$ is calculated by integration of $P(x(z))$.

6.3 Z_e, Z_o calculations with CST Microwave Studio

If one wants to evaluate the even and odd mode impedances from the geometry of two uniformly coupled lines, one usually only considers the E- and B-field distribution at a given frequency in the plane perpendicular to the propagation direction. For simple structures, the equations and the boundary conditions for the quasi static fields can be set up and solved, e.g., using Galerkin's method [77]. Sometimes it is possible to benefit from the symmetry of the waveguide using electric and magnetic walls for even- and odd-mode respectively. For some structures such as coupled microstrip lines, accurate closed form expressions can be found in the literature [78].
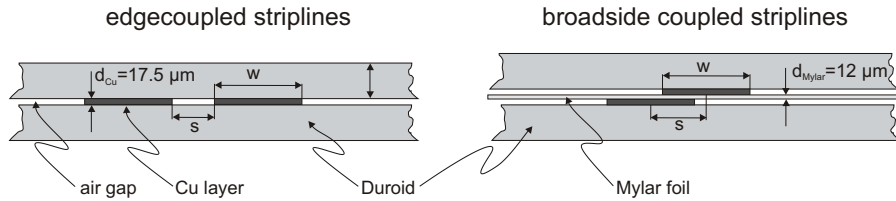

Fig. 6.6: *Geometry of edgecoupled and broadside coupled striplines. For the -3 dB coupler, a Mylar foil with 12 μm is used.*

For this work, however, the program library "CST Microwave-Studio" [79] was used to solve the field equations and to calculate the impedances and propagation constants. This has the advantage that almost arbitrary structured transmission line configurations can be used. First the structure is defined using the graphical user interface of CST MWS and the dimensions s and w are parameterized (see Fig. 6.6). In the z-dimension, the structure can be very short because only the port face (xy-plane) is used in the calculations. In the "multipin dialogue" in CST-MWS, the polarity of the conductors is defined for odd- and even- mode ([+, −] and [+, +] respectively) as indicated in Fig. 6.7.

Then the 2D frequency domain eigenmode solver is used to calculate the possible eigenmodes in the two dimensional port face region. Because the solver uses E- and B-field distributions, the line impedance is calculated with quantities which can easily be derived from the fields: The power flow P is calculated by integrating the Poynting vector over the port face and the current I can be expressed as the curl of the B-field. CST-MWS only considers the currents heading into the structure. Currents leaving the structure are not counted for the following calculation rule [79]:

$$Z_{CST} = \frac{P}{\sum I_{IN}^2} \tag{6.30}$$

The direction of the electric field in the vicinity of a conductor is determined by its potential. The direction of the magnetic field, and thus the current
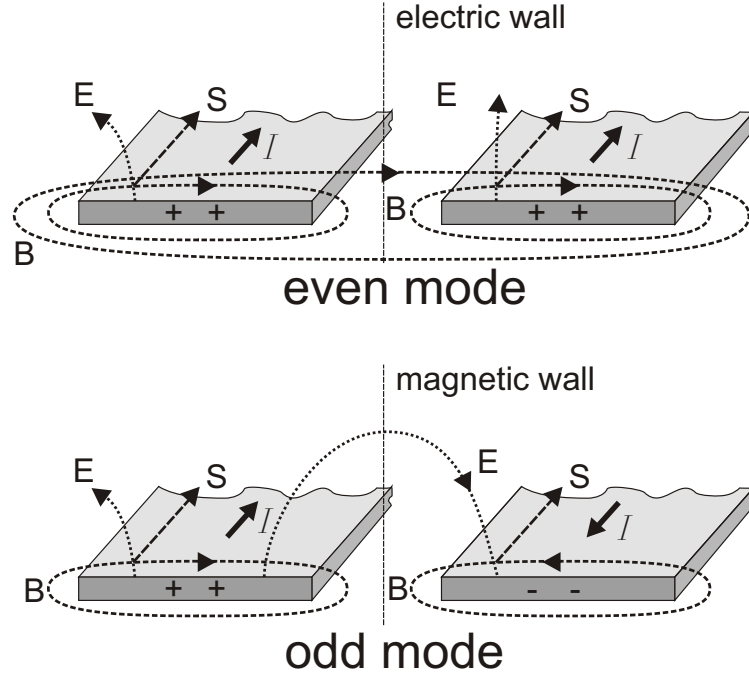
Fig. 6.7: *Even and odd mode of coupled strip lines. The polarity of the conductors is indicated by "+" and "−". The direction of the Poynting vector **S** can be derived from the **E**- and **B**-field lines. From the Poynting vector and the current distribution the even- and odd-mode impedances are calculated in CST MWS.*

direction is chosen such that the Poynting vector points into the structure. In the case of odd mode excitation, from $U_2 = -U$ follows that the current of the negative conductor is leaving the structure: $I_2 = -I = I_{OUT}$. This means that Z_{CST} differs from the commonly used definition of Z:

$$Z_{CST\,ODD} = \frac{U_1 I_1 + U_2 I_2}{I_1^2} = \frac{2UI}{I^2} = 2\frac{U}{I} = 2Z_{ODD} \qquad (6.31)$$

and

$$Z_{CST\,EVEN} = \frac{U_1 I_1 + U_2 I_2}{(I_1 + I_2)^2} = \frac{2UI}{4I^2} = \frac{1}{2}\frac{U}{I} = \frac{1}{2}Z_{EVEN} \qquad (6.32)$$

If the waveguide is filled with different dielectric materials, it is called inhomogeneous. Then the field patterns of the different modes show a frequency dependence: The higher the frequency, the more the field is concentrated in the material with the higher ϵ_r. The propagation constant is different for even and odd mode and varies with frequency and coupling factor strength. This means that the modes are not degenerated any more and can not be considered as simple TEM modes. Then it is difficult to design a broadband coupler because the assumption $v_e(\omega) = v_o(\omega)$ is not longer valid.

To avoid such a degradation of the TEM modes, the materials of the coupler should be chosen to have similar dielectric constants and air gaps between

different layers should be reduced to a minimum. Fig. 6.6 shows two different configurations, which are used in this work. The edge coupled structure is suitable for weak coupling ($S_{21} < -17\,dB$) and the broadside coupled lines can be used to achieve coupling up to -3 dB over a wide bandwidth if the spacer is thin enough. The mylar foil, which is used as spacer, has typically $\epsilon_r = 3.05$, while the substrate material RT/Duroid6002 from Rogers has $\epsilon_r = 2.94\pm0.04$. The air gaps in both configurations have the same thickness as the Cu layer ($(17.5 \pm 3.5)\,\mu m$). To appraise the degradation from the ideal TEM mode, the propagation constant of the even and odd modes can be evaluated with CST MWS and compared with each other.

6.4 Extraction of the geometric parameters

With the 2D solver of CST MWS, it is easy to compute the even and odd mode impedance for a given structure, say a broadside coupled stripline pair like in the right side of Fig. 6.6 with stripline width w and the spacing between the lines s. However, in order to gain the geometrical parameters $w(Z_e)$ and $s(Z_e)$ in dependency of Z_e with the constraint

$$\sqrt{Z_e(w, s)Z_o(w, s)} = Z_0 = 50\,\Omega \tag{6.33}$$

some effort has to be made. (In this study $Z_0 = 50\,\Omega$ is used, but of cause, it is possible to design couplers with an other Z_0, e.g., to obtain an adequate match to a HEMT input stage.)

6.4.1 CST Microwave Studio optimizer

One possible option would be to use the build in optimizer of CST MWS and vary w for a given spacing s in order to find a $Z_e(w, s), Z_o(w, s)$ pair which meets the condition 6.33 as close as possible.

This possibility is not feasible because optimization can not easily be automated for a sequence of different s values. But it is possible to generate whole tables of samples $Z_e(w_i, s_j)$ and $Zo(w_i, s_j)$ for a set w_i and s_j with CST MWS in a short time. (A couple of hours in dependence of mesh density.) In Fig. 6.8 such datasets are shown as surface plots. The data are taken from a model of broadside coupled lines with a $12\,\mu m$ Mylar spacer in the parameter space $s = 0 \ldots 3\,mm$, $w = 0.03 \ldots 1.3\,mm$.

6.4.2 Polynomial approximation

A first attempt was to approximate the $Z_{e,o}(w, s)$ functions by least square fitting polynomials $Z_e(w, s, w^2, ws, s^2, w^3, w^2s \ldots)$ and
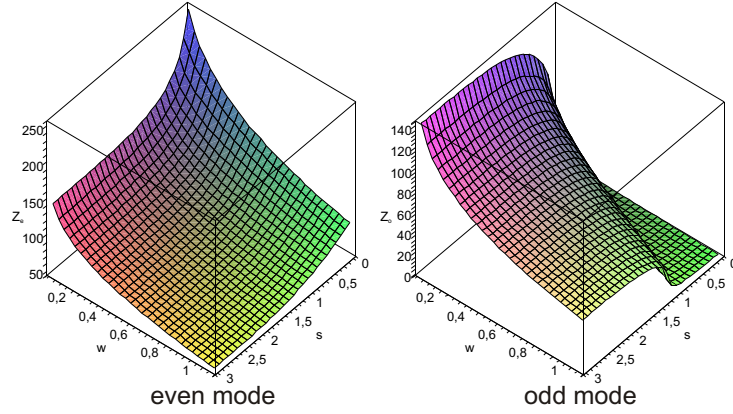
Fig. 6.8: *Surface plots of $Z_e(w,s)$ and $Z_o(w,s)$ in the range $s = 0\ldots3\,mm$, $w = 0.03\ldots1.3\,mm$. Even and odd mode impedance of broadside coupled lines with a $12\,\mu m$ Mylar spacer on RT/Duroid6002. $Z_o(w,s)$ changes rapidly in the vicinity of the line $w = s$ because the field changes from a broadside to a quasi edgecoupled configuration. (Compare also Fig. 6.6 for $w = s$.)*

$Z_o(w,s,w^2,ws,s^2,w^3,w^2s\ldots)$. The program "Maple" [80] has been used for these calculations. Unfortunately, the polynomial especially for $Z_o(w,s)$ does not converge fast enough within the parameter space and the $Z_o(w,s)$ function is approximated only inaccurately by this method. For polynomials with $O(w\,s) \geq 5$, the root finding of equation 6.33 with "Maple" becomes difficult and time consuming which limits the order of the polynomials to 5. While this method can be used for couplers with weak coupling, where the $Z_o(w,s)$ surface only varies slowly, the method fails at higher coupling factors with a more pronounced curvature.

6.4.3   Linear interpolation scheme

Instead, a much simpler linear interpolation scheme has been developed to obtain accurate parameters $w(Z_e)$ an $s(Z_e)$ with the constraint $Z_0(w,s) = \sqrt{Z_e(w,s)Z_o(w,s)} = 50\,\Omega$ even at high coupling levels. With this procedure, all structures developed within this work have been calculated. It is explained in Fig. 6.9.

Once a set $Z_e(w_i,s_j)$, $Z_o(w_i,s_j)$ has been calculated with CST, one may follow these steps to obtain values for w and s:

1. Calculate the new set $Z_0(w_i,s_j) = \sqrt{Z_e(w_i,s_j)Z_o(w_i,s_j)}$

2. Find for each s_j a w_k such that $Z_0(w_k,s_j) \leq 50\,\Omega$ and $Z_0(w_{k+1},s_j) > 50\,\Omega$
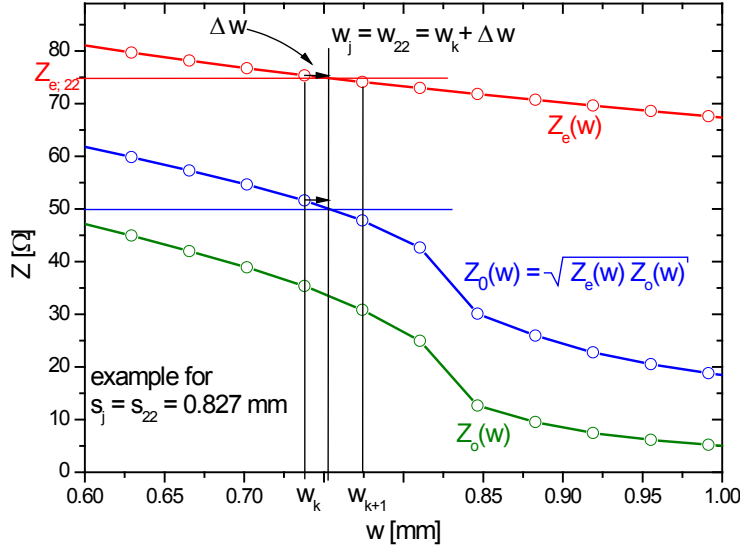
Fig. 6.9: *Interpolation scheme for the evaluation of $w(Z_e)$ an $s(Z_e)$ with the constraint $\sqrt{Z_e(w,s)Z_o(w,s)} = 50\,\Omega$. For a given s_j, the Z_0 values are plotted as a function of w and an intermediate w_j is found for which $Z_0 = 50\,\Omega$. For this w_j, the values $Z_e(w_j, s_j)$ and $Z_o(w_j, s_j)$ are calculated and used for interpolation of $w(Z_e)$ and $s(Z_e)$ for arbitrary values of Z_e.*

3. Find for each s_j a w_j which satisfies $Z_0(w_j, s_j) = 50\,\Omega$ by solving the linear interpolation for $Z_0(w, s_j)$ along the w-axis for Δw

$$50\,\Omega = Z_0(w_j, s_j) = Z_0(w_k + \Delta w, s_j) + \frac{Z_0(w_{k+1}, s_j - Z_0(w_k, s_j))}{w_{k+1} - w_k}\Delta w$$

(6.34)

and thus obtain $w_j = w_k + \Delta w$.

4. Find new values $Z_e(w_j, s_j)$ with

$$Z_e(w_j, s_j) = Z_e(w_k, s_j) + \frac{Z_e(w_{k+1}, s_j - Z_e(w_k, s_j))}{w_{k+1} - w_k}$$

(6.35)

These new values now satisfy $Z_0 = 50\,\Omega$. Fig. 6.10 shows a surface plot with the new $[w_j, s_j, Z_e(w_j, s_j)]$ points included. The same calculations can be done for $Z_o(w_j, s_j)$.

5. Create continuous second order spline interpolation functions $w(Z_e)$ and $s(Z_e)$ from the calculated $w_j(Z_e(w_j, s_j))$ and $s_j(Z_e(w_j, s_j))$ pairs. A plot of the data points and the corresponding spline interpolation is shown in Fig. 6.11.

Even at very high coupling levels of -3 dB, linear interpolation has proven to be accurate enough. In case even higher accuracy is needed, higher order interpolation can be implemented easily.
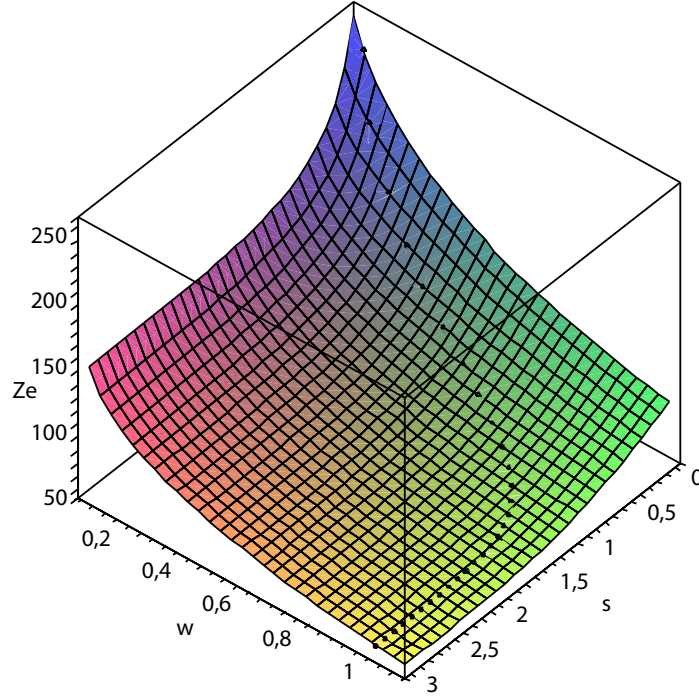
Fig. 6.10: $Z_e(w, s)$ surface plot with the new (black) points for which $Z_0(w, s) = 50\,\Omega$. Note that the black points lie on the $Z_e(w, s)$ surface calculated before in CST, but not on the grid points.
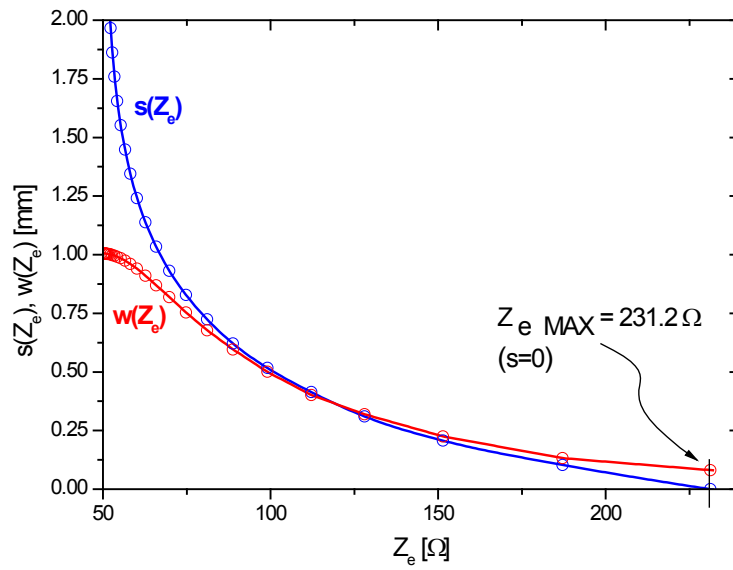

Fig. 6.11: $w(Z_e)$ and $s(Z_e)$ function created by spline interpolation of the $w_j(Z_{e;j})$ and $s_j(Z_{e;j})$ pairs for which $Z_0(w_j, s_j) = 50\,\Omega$.

6.5   Minimizing the passband ripple

The first step of a coupler design is to define the function of the coupling level over the passband of the coupler $C(\omega)$ and perform a Fourier transform in order to obtain a spatial function $P(x(z))$ which determines the impedance distribution over the coupled lines. The inverse Fourier transform of $P(x(z))$ again results in the coupling function $C(\omega)$ in the frequency domain. This process is illustrated in Fig. 6.12. $P(x(z))$ has usually not only compact support over a small z-range around zero, but is only slowly decaying towards infinite z. With the final coupler length over a few wavelengths, the Fourier integral is truncated at $z = \pm a/2$, which causes ripples of the coupling characteristics in the frequency domain. These so called Gibbs' oscillations are most pronounced near steep edges of $C(\omega)$ and are due to the slow convergence of the Fourier series. There are different possibilities to minimize the ripple in order to obtain a maximally flat passband:

6.5.1   Weighting factors

The first method discussed here was proposed in [81] and used for the design of the -17 dB coupler. A piecewise constant weighting function is applied to the time domain response $P(x(z))$. The weighting factors are originally derived in [82] for N-section stepped impedance couplers by a discrete Fourier series representation of constant coupling over the $0 \dots f_{MAX}$ frequency range. The step width $dz = v/f_C$ is calculated from the center frequency $f_C = f_{MAX}/2$ and from the propagation velocity v, which was calculated with the CST 2D eigenmode solver.

The Fourier series representation of constant coupling up to f_{MAX} can be written as follows:

$$C(\omega) = \begin{cases} C_0 & 0 \le \omega \le f_{MAX} \\ 0 & \text{else} \end{cases} \tag{6.36}$$
$$= C_0 \frac{4}{\pi}[\sin(\frac{\omega}{2f_{MAX}}) + \frac{1}{3}\sin(\frac{3\omega}{2f_{MAX}}) + \frac{1}{5}\sin(\frac{5\omega}{2f_{MAX}}) + \dots]$$

If only a finite number of summands is used, they have to be weighted in order to form a maximally flat representation of the coupling function $C(\omega)$:

$$C(\omega) \approx C_0 \frac{4}{\pi}[\quad w_1\sin(\tfrac{\omega}{2f_{MAX}}) + w_3\tfrac{1}{3}\sin(\tfrac{3\omega}{2f_{MAX}}) \tag{6.37}$$
$$+ w_5\tfrac{1}{5}\sin(\tfrac{5\omega}{2f_{MAX}}) + w_7\tfrac{1}{7}\sin(\tfrac{7\omega}{2f_{MAX}})]$$

These weighting factors w_i have been computed in [82] and are used here for weighting of the lobes of the continuous P(z) function. The weighting factor method is applicable only for a constant coupling function over the interval $0 \dots f_{MAX}$.
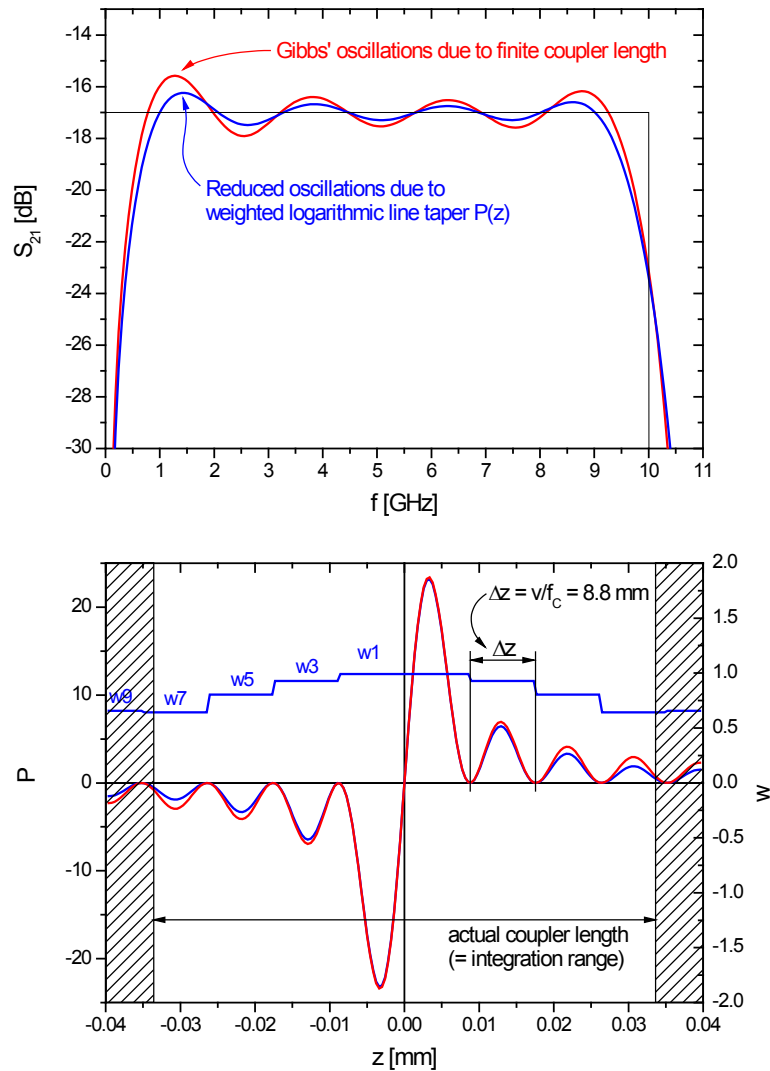
Fig. 6.12: *Above: The truncation of the Fourier transform by the final coupler length causes Gibbs' oscillations. (red curve.)*
Below: The P(z) function is weighted with weighting factors w$_i$ in order to reduce the Gibbs' oscillations (ripple).

6.5.2   Apodization

If another coupling distribution is desired, one may use apodization (greec, literally meaning "removing the foot") of $C_V(\omega)$ in order to reduce the passband ripple. Apodization is a widely used technique in Fourier transform spectrometry, ultrasonic imaging and other signal processing applications. A variety of window functions with different properties are in use for different applications. A concise review over many window functions is given in [83]. In the context of coupler design, apodization is the convolution of $C_V(\omega)$ with a window function in order to smooth $C_V(\omega)$ and reduce the high "frequency" components of $C_V(\omega)$ to obtain a time domain function $P(x)$ which is better localized in an interval around $x = 0$.
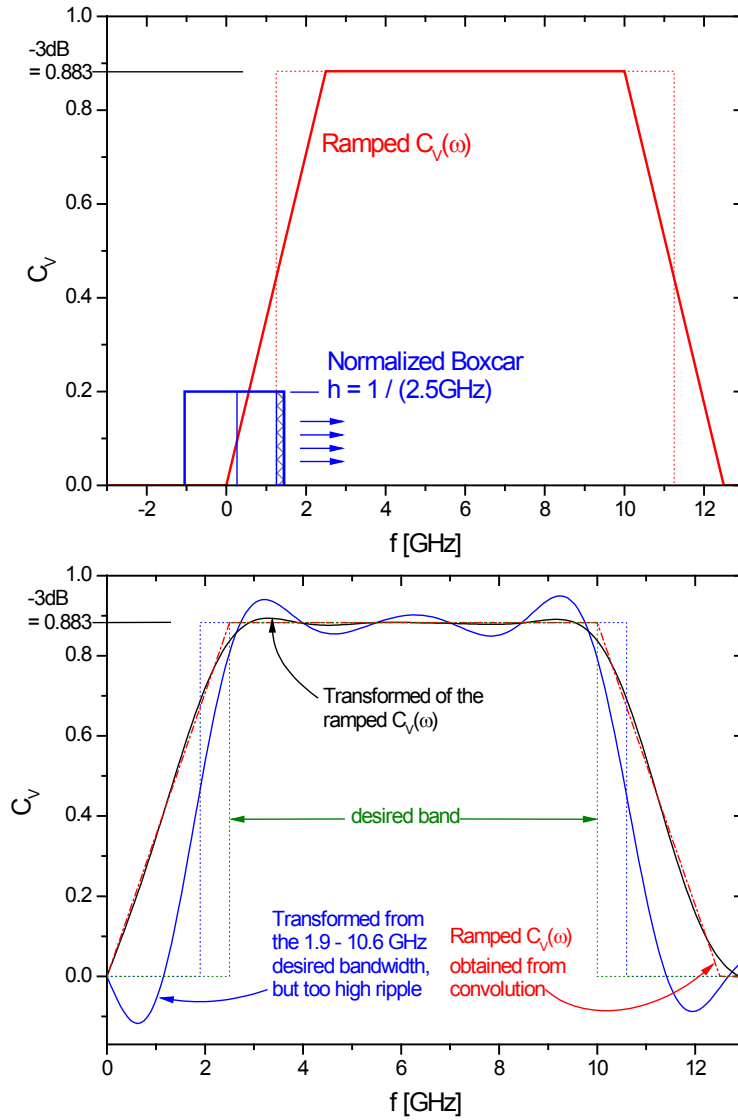
Fig. 6.13: *Above: A ramped $C_V(\omega)$ function (red solid line) is obtained by smoothing the original function (red dashed line) with a normalized boxcar function.*
Below: The Fourier transform of the truncated P(z) function (black line) of the smoothed $C_V(\omega)$ function (red line)is much more flat than the function obtained from the stepped original. This can be used to obtain a flat band within the desired bandshape.

In praxis, one likes to minimize the coupling to the actually needed bandwidth because $Z_{eMAX} = Z_e(z = 0)$ rises with growing bandwidth and large values of Z_e are difficult to implement because of fabrication tolerances. Furthermore, the TEM mode propagation tends to degrade for lines with high coupling levels. This may influence the overall performance of the coupler. Therefore, it may be desirable not to start at $f = 0$. For the -3 dB coupler, a bandwidth from 2.5-10 GHz was chosen.

For a given coupler length of approximately 70 mm, the initial band should be about 1.9-10.6 GHz to actually achieve the desired bandwidth. This is illustrated in Fig. 6.13 bellow. Unfortunately, the truncation at $\pm 35\,mm$ results in rather large Gibbs' oscillations. Hence another way to generate the passband is chosen: An original passband from $1.25 - 11.25\,GHz$ is smoothed with a normalized boxcar function with a bandwidth of 2.5 GHz as shown in Fig. 6.13 above. The boxcar window is chosen here because of mathematical simplicity, while resulting in tolerable ripple in $C_V(\omega)$. Other smoothing functions (i.e. Gaussian) may result in an even better theoretical performance. But the real coupling properties are dominated by fabrication inaccuracies and non TEM mode wave propagation rather then by small differences caused by different smoothing functions. The resulting ramps drastically reduce the high "frequency" components of $C_V(\omega)$. This has the desired effect to $P(z)$, which now may be truncated to the specified coupler length.

6.6   Fabrication of the couplers

From the reflection coefficient distribution $P(z)$, the distribution of the even mode impedance $Z_e(z)$ is obtained by evaluating the integral (6.29). From $Z_e(z)$ and the second order spline interpolation functions $w(Z_e)$ and $s(Z_e)$, the actual geometric parameters $w(z)$ and $s(z)$ are obtained. $Z_e(z)$, $w(z)$, and $s(z)$ are evaluated at 201 equidistant points along the z-axis in the interval $z = -35\,mm \ldots 35\,mm$. From there, the actual polygon points are generated with Maple. Algorithms for edgecoupled, broadside coupled and broadside tandem coupled geometries have been implemented. The program takes into account the different meanings of s for edgecoupled and broadside coupled structures and is able to add interface lines and 180° bends of a desired radius as interconnection for the tandem configuration. The data is exported to two different ASCI file types. The contents of the first format can be pasted into the AutoCAD command line in order to generate a "polyline", which has the shape of one branch of the coupler. The second format can be imported as polygon into CST MWS for the simulation of the whole structure. The results of this simulations are discussed in section 6.7.

The PCB board outline, holes for the SMA jack inner conductors, recess clearance for the bond wires, alignment marks and structures for the control of the etching accuracy are added in the AutoCAD drawing. A 3D view of the SMA to stripline transition is shown in 6.14.

The broadside PCB needs in addition a snap-in structure, which enables the alignment of the top and the bottom PCB. It consists of a complimentary arrangement of squares, whose sizes are growing with the distance to the center of the PCB. The larger the distance to the center, the tighter the fit. The squares are chamfered in order to avoid irregularities from the etching of sharp edges. This way, the alignment of the boards has a similar accuracy
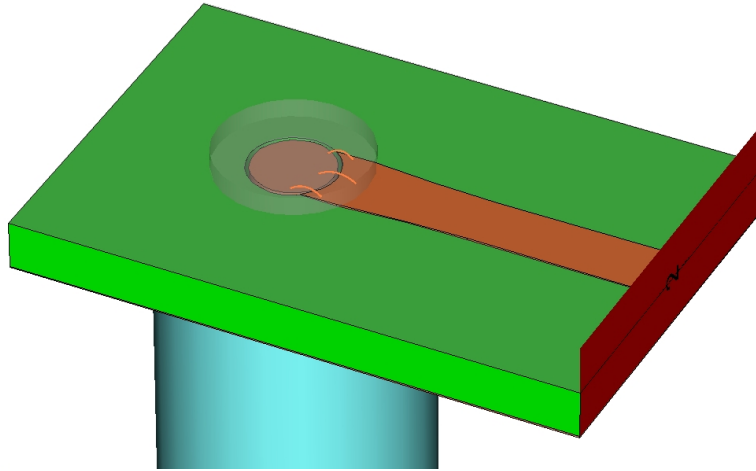
Fig. 6.14: *CST MWS model for the transition between SMA inner conductor to the stripline on the RT/Duroid6002 sandwich. The upper half of the sandwich is hidden in this view. Only the small recess which avoids the contact of the upper board with the bond wires is visible.*

as the mask and the etching process ($\approx 10 \ldots 20\,\mu m$). The complete PCB drawing and the corresponding board itself is shown in Fig. 6.15.
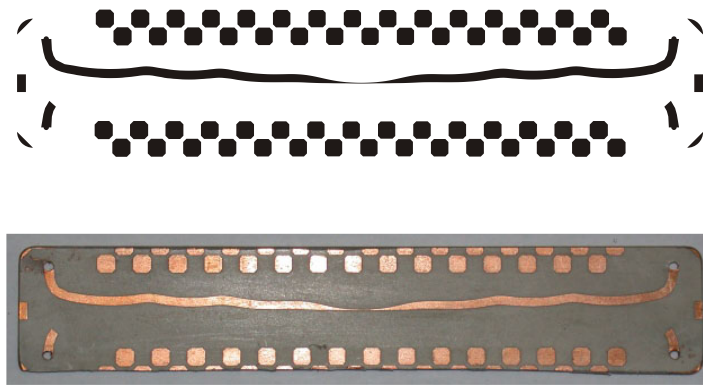

Fig. 6.15: *Above: CTF mask with snap-in structure, which enables the alignment of the top and the bottom PCB of the stripline sandwich.*
Below: A Rt/Duroid6002 board with the etched Cu metallization and four holes for the inner conductors of the SMA connectors.

The AutoCAD drawing is exported as pdf-file. From the pdf-file, a CTF mask is generated by Sutorius, Cologne. CTF masks are usually used for reprography. They provide accuracy of 2400 dpi ($\approx 10\,\mu m$) with high contrast. This is about the same accuracy which can be put into practice with an isotrope etching process used for the production as described below. This accuracy is marginal for the -3 dB coupler, which has a minimum stripline width of 84 μm. The masks are rather cheep and can be produced and delivered within 3-4 working days, which enables short design cycles.

6.6.1   Milling

The PCB outline, the data for the holes, for the SMA jacks and the recess for the bond wires is exported as a dxf-file. The data are preprocessed with the program CircuitCam 3.2 and exported as cam- and lmd-files, which are used to mill the PCB with all structure details on the LPKF circuit board milling machine (LPKF Protomat C100/HF). The milling process is described in more detail in appendix A.

6.6.2   Lithography

After the complete milling process, the RT/Duroid6002 board is coated with the photoresist AZ7212. Excess resist is removed with a centrifuge. After $90\,s$ exposure to UV-light, the resist is developed with a diluted sodium hydroxide ($NaOH$) solution. The $17.5\,\mu m$ Cu-laminate is etched with sodium peroxodisulfate ($Na_2S_2O_8$) solution with a concentration of about $250\,g/l$ ($1\,mol/l$) at a temperature around $45°C$. The solution is circulated by a steady air bubble flow. The PCB was removed from the bath immediately after the etching was complete to avoid undercutting. After cleaning and removing the photoresist, the PCB was checked under a microscope and build in the coupler housing.

6.6.3   Assembly

The SMA inner conductors stick out from the coupler housing ground plane $0.762\,mm$ (the thickness of the board). The bottom PCB is put over the inner conductors and glued into the housing. The stripline is then bonded with 3-5 wires to the SMA connector. Bonding to the soft RT/Duroid6002 board is not easy. To assure strong bond contacts, the first bond should always be placed to the face of the inner conductor, while the second bond with higher ultrasonic energy should be placed to the RT/Duroid6002. Before, both surfaces have to be polished and subsequently cleaned. A photo of the bond connection is shown in Fig. 6.16.

The Mylar foil is then fixed with Apiezon N vacuum grease to the board surface. Then, the top PCB is aligned with the help of the "LEGO" structure. Since the complimentary squares have only a hight of $17.5\,\mu m$, the snap-in is weak, but still sensible. When the boards are aligned, they are slightly pressed to each other by closing the box.

The contact of the top Cu structure to the bottom Cu layer is attained just by mechanical pressure or alternatively with a solder joint. Both methods seem to be stable under cryogenic cycling. (The boards have the same thermal expansion coefficient.) RF- and DC-conductivity have been checked at cryogenic temperatures for both methods.
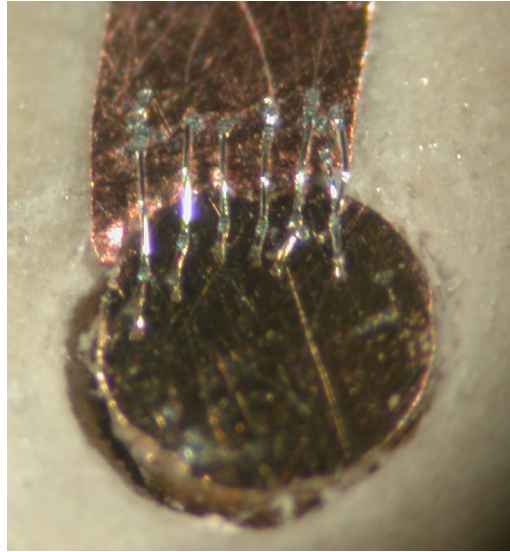
Fig. 6.16: *Photo through the microscope of the SMA to stripline transition. As many bonds as possible are placed between the stripline and the SMA inner conductor. The small slack due to the arched structure of the bond wires, makes the connection reliable at cryogenic temperatures.*

6.7   Measurements and simulation results
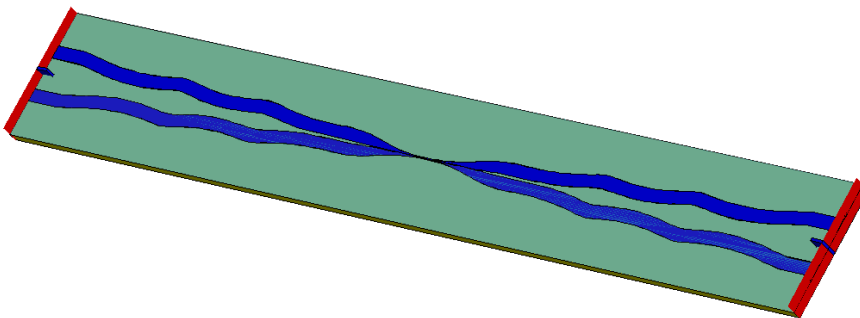
6.7.1   The -3 dB coupler

Fig. 6.17: *CST MWS model of the -3 dB coupler. For simplicity, this structure does not contain the SMA to stripline transition. The structure is fed by waveguide ports (red plaines), which launch a TEM mode on the stripline.*

Prior to ordering the CTF mask and building up the coupler, a simulation of the complete coupler has been carried out in order to check the correctness of the models. The CST MWS model is shown in Fig. 6.17. It is defined as a lossless structure and does not include the SMA to stripline transitions. The stimulation ports are implemented as stripline waveguide ports, which are excited by a nearly exact TEM mode.

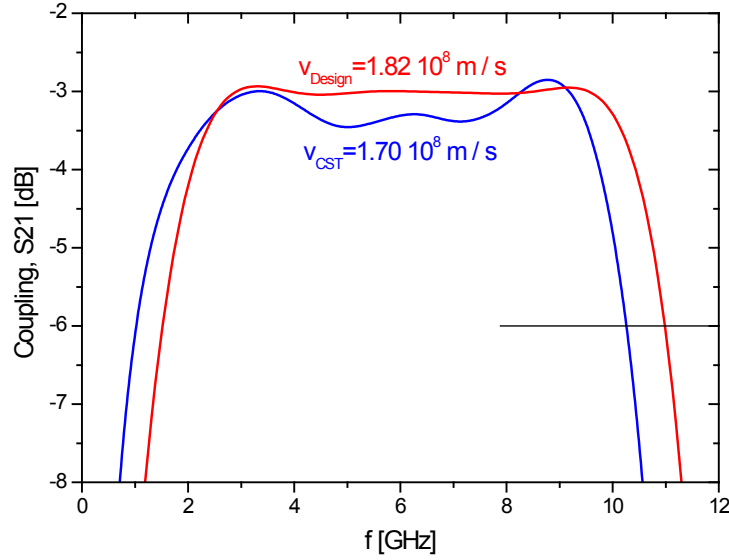Fig. 6.18 compares the simulation result to the design bandpass, which is

Fig. 6.18: *Comparison between the design bandpass calculated with Maple and the simulation result obtained with the CST MWS model depicted in Fig. 6.17. The main difference emerges from an overestimation of the wave velocity in the calculations with Maple.*

obtained by inverse Fourier transform of $P(x)$ with the design wave velocity of $v_{Design} = 1.82 \; 10^8 \; m/s$. The bandshape of the simulation is in good agreement with the design curve. Only the slight shift of the band towards lower frequencies indicates a wave velocity of $v_{CST} = 1.70 \; 10^8 \; m/s$.
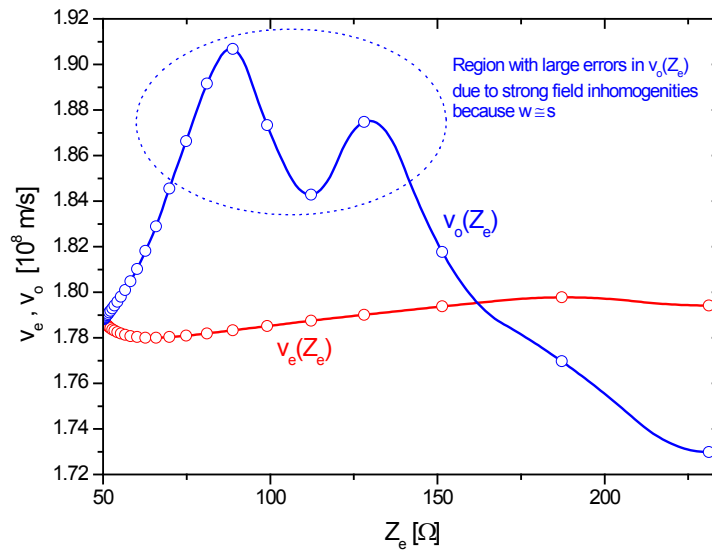

Fig. 6.19: *Even and odd mode wave velocity computed by interpolation of $v_e(s, w)$ and $v_o(s, w)$ values, obtained by the 2D solver of CST MWS. In the region where $w \approx s$, the results from the 2D solver are of low accuracy. Due to the field distribution, the slight inhomogeneity of the waveguide is most pronounced in this geometry.*

With a similar interpolation scheme as described in section 6.4.3, it is possible to compute the even and odd mode velocity in dependence of $Z_e(z)$. A plot is shown in Fig. 6.19. With this information, it is possible to obtain the velocity distribution over the coupler length $v_e(z)$ and $v_o(z)$, which is shown in Fig. 6.20. The average velocities can be computed the following way:

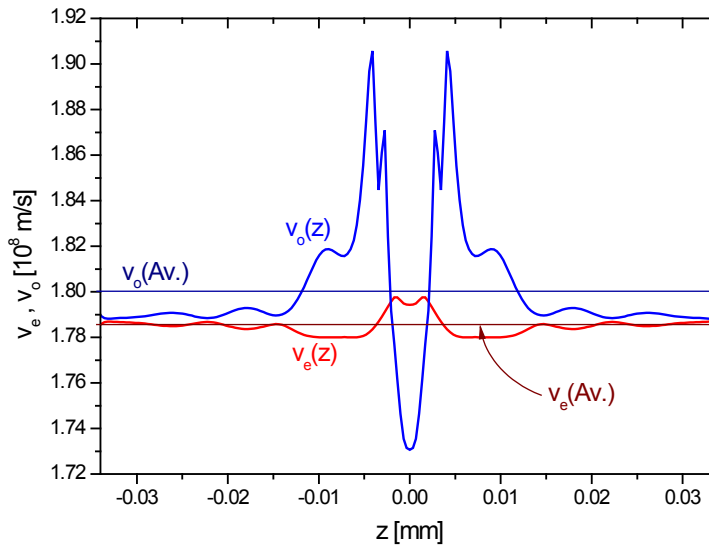$$\tau_{e,o} = \frac{a}{\langle v_{e,o} \rangle} = \int_{-a/2}^{a/2} \frac{dz}{v_{e,o}(z)} \tag{6.38}$$

Fig. 6.20: *Even and odd mode wave velocity distribution over the coupler length. $v_e(z)$ and $v_o(z)$ are plotted together with the mean values over the coupler length.*

While $\langle v_e \rangle$ and $\langle v_o \rangle$ are close to each other and to v_{Design} (because v_{Design} was a first estimate of the actual $\langle v_e \rangle$), they differ by about 7% from the simulation of the complete structure and about 11% from the measured value. The results are summarized in Tab. 6.7.1.

v_{Design}	$1.82\ 10^8\ m/s$
$\langle v_e \rangle$	$1.79\ 10^8\ m/s$
$\langle v_o \rangle$	$1.80\ 10^8\ m/s$
v_{CST}	$1.70\ 10^8\ m/s$
$v_{Measured}$	$1.62\ 10^8\ m/s$

Tab. 6.1: *Various mode propagation velocities compared with measurement and 3D simulation results.*

The differences are believed to originate from the coupler region were $w \approx s$. In this region, the strong inhomogeneities of the fields may lead to calculation

inaccuracies. The fields are determined with more accuracy in the complete model because the critical regions are resolved with much more mesh lines compared to the 2D eigenmode calculations.

Furthermore, the velocity values can be used to give an estimate for the maximum phase delay between even and odd mode waves over the whole coupler length. For instance, at the center frequency of the coupler

$$\Delta\phi = 2\pi f_C(\tau_e - \tau_o) \approx 7° \tag{6.39}$$

This is a rather low phase delay. Thus, only very weak degradation of the coupling capabilities may originate from there.
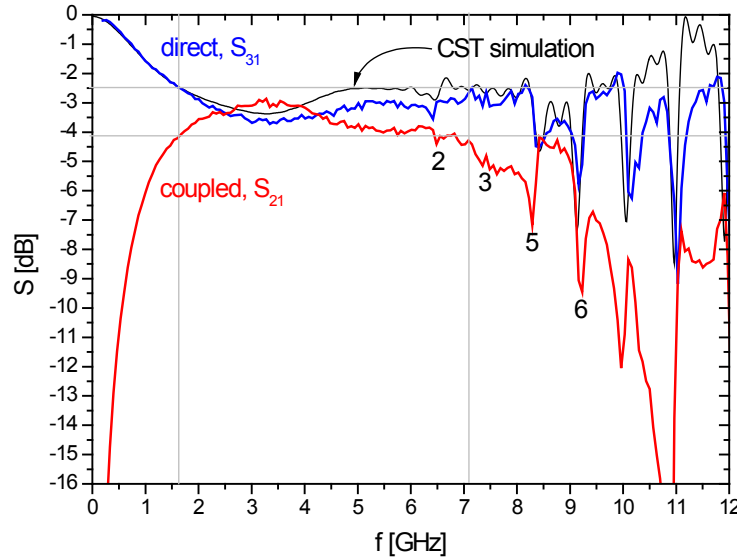

Fig. 6.21: *Network analyzer measurements of the S-parameters of the first model compared with a CST MWS simulation of a complete model including SMA jacks (black line). Above 7 GHz, the coupling is deteriorated by the box resonances shown in Fig. 6.22*

After the assembly, the coupler was tested with a network analyzer at room temperature and at 77 K (LN_2). Starting from the original design, the coupler was modified in two design steps in order to increase the performance. Fig. 6.21 shows the measured S-parameters of the original structure.

The coupler shows good performance from 1.7 GHz to 7.1 GHz. This corresponds to a 4.1 : 1 bandwidth.

To give an interpretation of the resonance spikes in the S-parameters above 6.3 Ghz, a CST MWS model was prepared for the whole structure including SMA jacks. Basically, the measured resonances are confirmed by the calculations with the model. In a second simulation, the field distribution for several resonance frequency points (marked with numbers in the S-parameter plot) has been investigated. Fig. 6.22 shows the second, third, fifth and sixth harmonic box resonance.
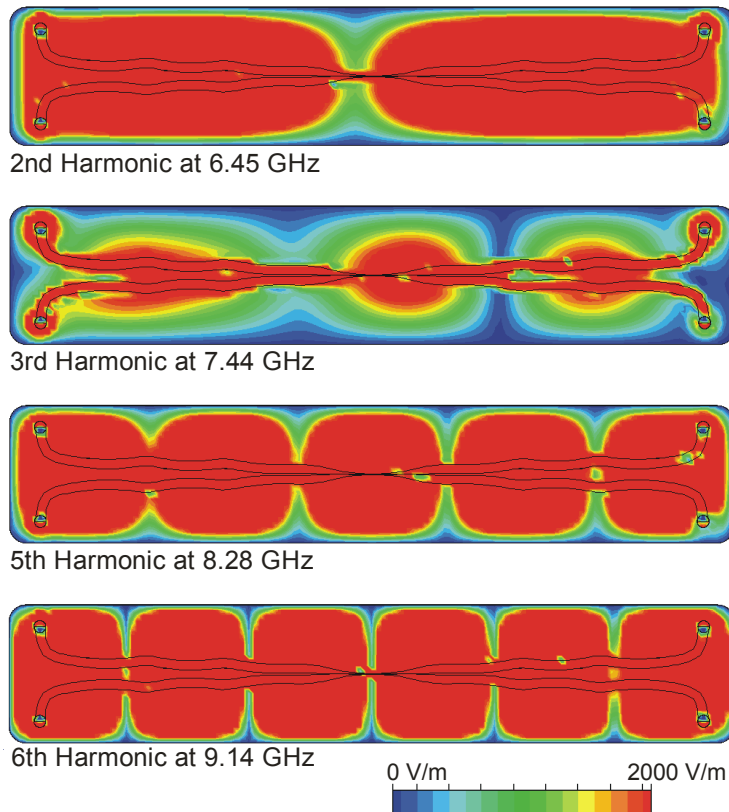
2nd Harmonic at 6.45 GHz

3rd Harmonic at 7.44 GHz

5th Harmonic at 8.28 GHz

6th Harmonic at 9.14 GHz

0 V/m   2000 V/m

Fig. 6.22: *Box modes. 2nd, r^{3d}, 5th and 6th harmonic (top down). The box modes are excited by the SMA to stripline transition (local non-TEM field distribution).*

Presumably, these box modes are excited by the field irregularities at the transitions from the SMA jack to the stripline. If one adds open-boundary conditions in the model at the end faces in z-direction, the box modes are absorbed and do not disturb the coupling any more. However, in praxis it is very difficult to achieve the absorption of the waves by placing an absorber at the endings of the structure. There will always be a small air gap between the absorber and the substrate material and the waves are reflected back into the coupler at this discontinuity of the dielectric constant instead of being absorbed. A possibility to avoid reflections would be to coat the substrate with an absorbing film in a triangular shape to achieve a smooth change in dielectric constant and conductivity.

Instead of absorbing the standing waves, the box was modified by placing screws at regular small distances through the box and the substrate, to prevent the box modes from propagating. (The corresponding CST MWS model and a photo of the modified housing are shown in Fig. 6.23). By these electrical connections, the effective volume of the cavity is reduced. The fields are short-circuited by currents through the screws and the first box mode, which fits to the new boundary conditions, has a eigenfrequency of about 8.8 GHz, which is equivalent to a 5.1 : 1 bandwidth for the coupler.
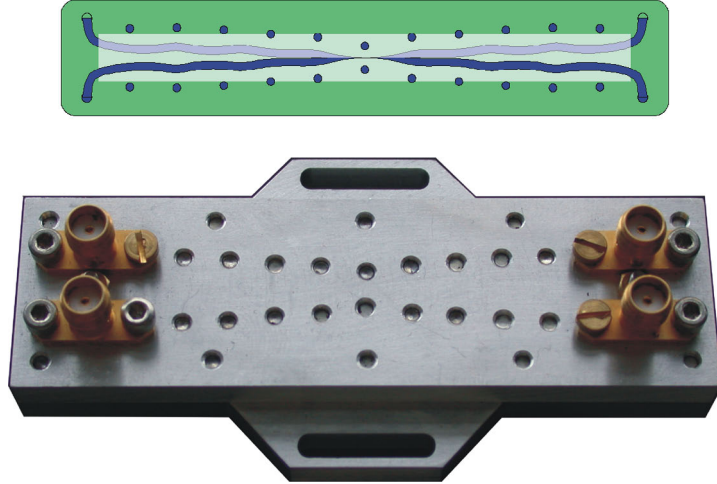
Fig. 6.23: *Suppressing box modes by changing the boundary conditions in the coupler housing. Screws are placed in short interspacing over the coupler housing, forcing $\mathbf{E}_z = 0$ at any screw location.*
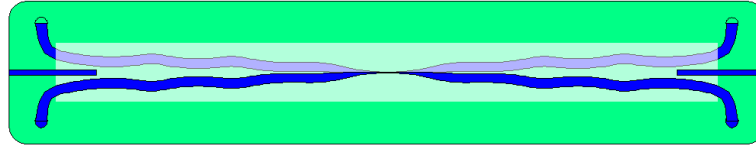

Fig. 6.24: *TEM mode launchers implemented by two conducting septa between the SMA jacks. The wave propagation is guided along the stripline until the TEM mode is formed.*

Another significant step towards better coupling and increased bandwidth was achieved by placing two septa in between adjacent ports. This construction was first verified by simulations and later tested at the coupler model. The idea behind this construction is to improve the purity of the TEM mode, which is launched at the SMA to stripline transition. All energy is guided along the line into the coupling structure and the fields are forced to shape perpendicular to the stripline. This configuration not only gives enhanced bandwidth of $5.5 : 1$, but also a flatter coupling distribution at higher frequencies. The model with the mode launchers (septa) is displayed in Fig. 6.24. In praxis, the metallic septa are provisorily implemented by cutting slits in the substrate, which are then filled with aluminum foil. If one uses substrates with higher ϵ_r, one may omit the metal because the high difference in the dielectric constants will cause a total reflection of the waves at the interface.

Fig. 6.25 summarizes S_{21} measurements of the hybrid in the different design stages and Fig. 6.26 shows magnitude and phase of the coupled and direct response of the final design. In the same figure, a plot of the signal suppression of the isolated port can be found. The phase difference $\phi(S_{21}) - \phi(S_{31})$ is $90° \pm 3°$ up to 9 GHz, which is within measurement accuracy exactly the desired phase shift.
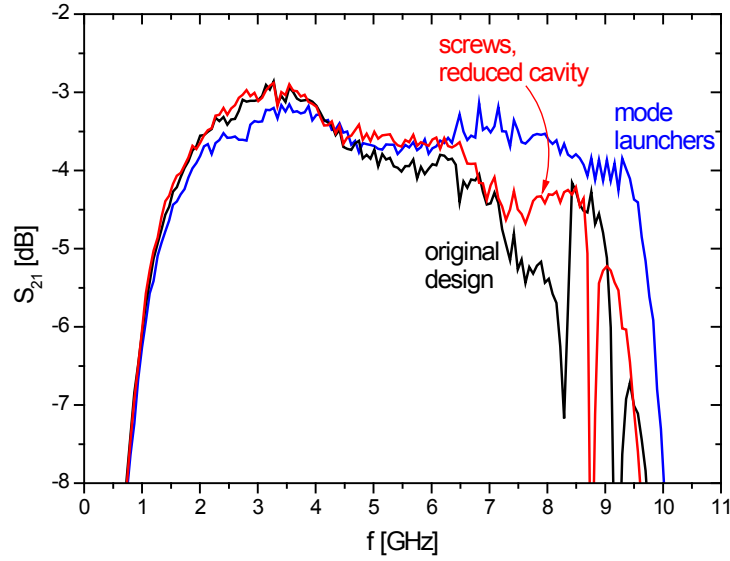
Fig. 6.25: *Coupler performance for three coupler models. The performance could be increased by using box mode suppression by screws. An even better result is obtained with the mode launcher design.*
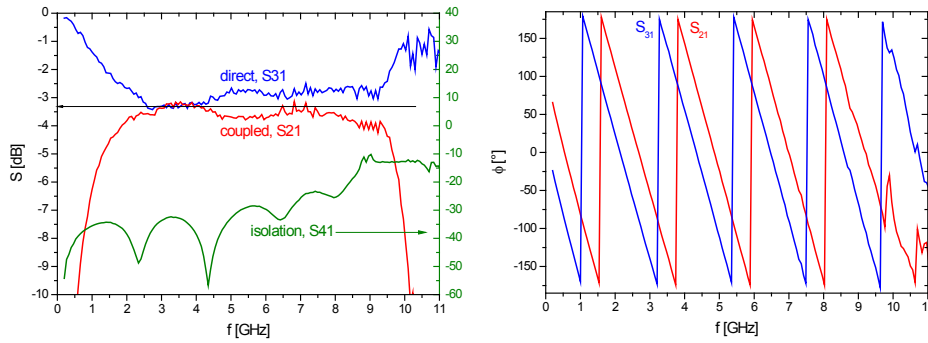
Fig. 6.26: *Left: Direct transmission (S_{31}), coupled signal, (S_{21}) and isolation (S_{41}, scale on the right) for the final coupler model with mode launchers. Right: The phase difference of coupled and direct signal is exactly 90° up to 9 GHz.*

This simplifies the calculations of the contribution to the sideband separation ratio $SSR(\omega)$ in case of the SSB mixer and the reflection coefficient reduction $C_{BA}(\omega)$ for the balanced amplifier. (Compare section 6.1.3 and 6.1.4.) Both values have, of course, similar shapes over ω. They are shown in Fig. 6.27.

6.7.2 The -17 dB coupler

The production of the -17 dB edgecoupled structure is less critical because the smallest dimension is the gap between the lines with $s = 130\,\mu m$ (compared to an etching accuracy of $\approx 10\ldots20\,\mu m$). The alignment accuracy of the top board with the bottom board is not critical, thus no "LEGO" structure is needed. The PCB boards of the edgecoupled design fit into the same housing
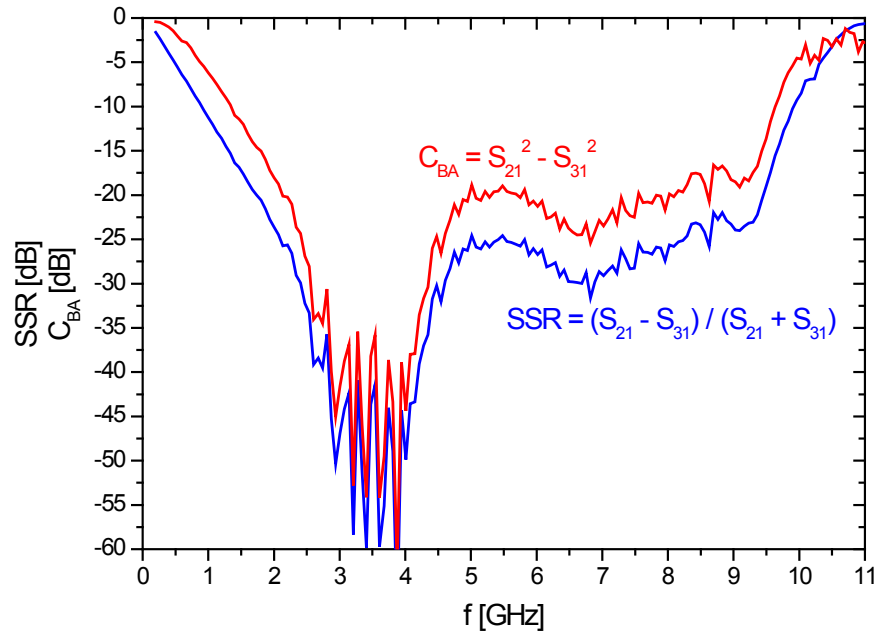
Fig. 6.27: *Red: Sideband separation ratio SSR in case of an ideal RF hybrid and equal mixers in both branches. (SSR=ratio between the power of the suppressed sideband to the power of the unsuppressed sideband. Compare section 6.1.3)*
Blue: Reflection coefficient reduction $C_{BA}(\omega)$ for the balanced amplifier. Compare section 6.1.4

.
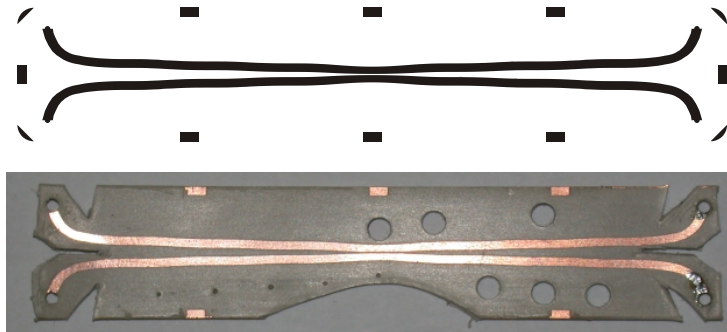
Fig. 6.28: *Above: CTF mask for the -17 dB edgecoupled design.*
Below: RT/Duroid6002 board with the edgecoupled striplines. The holes and insections come from different experiments with mode launchers and absorber material in the coupler housing.

as the PCBs for the -3 dB coupler and have been tested there. Fig. 6.28 shows a photo of the coupling structure. The mode launcher technique was tested with this design as well. The coupling with and without metallic mode launchers is shown in Fig. 6.29.
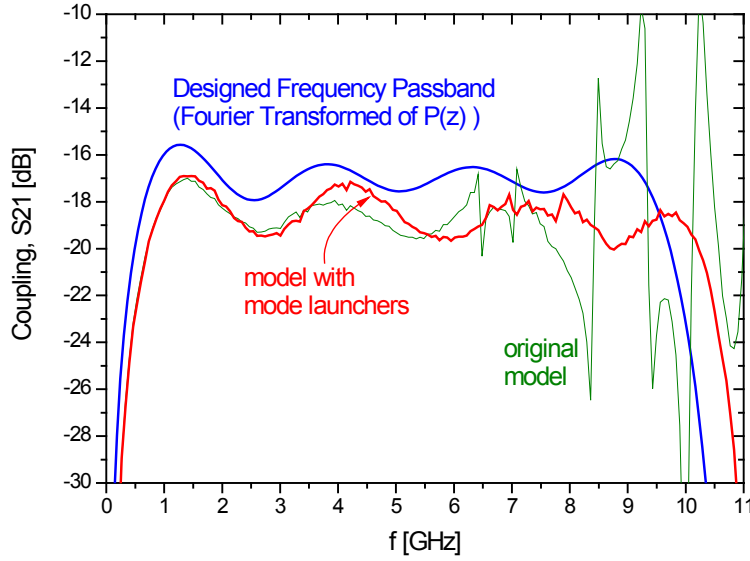
Fig. 6.29: *Network analyzer measurements of the original coupler model compared with the better performance of the model with mode launchers and a CST MWS simulation of the whole structure (including SMA jacks and mode launchers).*

6.7.3 Summary and outlook

The investigation and realization of two different coupler types resulted in two high performance hybrids, usable in cryogenic environments. They are ready to be used for first tests of the sideband separating mixer (-3 dB coupler) and conversion gain measurements of phonon cooled hot electron bolometer mixers (-17 dB coupler).

For the integration of the couplers in a focal plane array, a size reduction is desirable. This can be achieved by using substrates with higher ϵ_r (e.g., high resistivity Silicon with $\epsilon_r = 11.8$). Numerical computations for different configurations in Silicon have been carried out and show a promising size reduction of a factor of about two. In near future, these couplers may be fabricated in the cleanroom facility.

The determining factor for the coupler length is the lower edge of the coupler band (f_{MIN}). If f_{MIN} is increased, the coupler length can be reduced.

A further small size reduction is achieved by implementing the striplines in a superconducting material instead of using copper or gold. This is due to the kinetic inductance of the superconducting charge carriers. This will also slightly reduce the losses in the coupler, although most of the low losses of the coupler originate from energy dissipation in the dielectrics.

To achieve an even better implementation of the desired coupling within the passband, it is possible to correct the initial voltage coupling function $C(\omega)$ for the actual propagation velocity and for coupling degradation originating from the partial non-TEM mode propagation in the coupler.

Appendix A

Milling machine and milling processes

A.1 Milling tools

1.0 mm, contour

0.8 mm, contour

0.25 mm, surface

1.0 mm, surface

V-shape, surface

1.0 mm drill, reference holes in Al
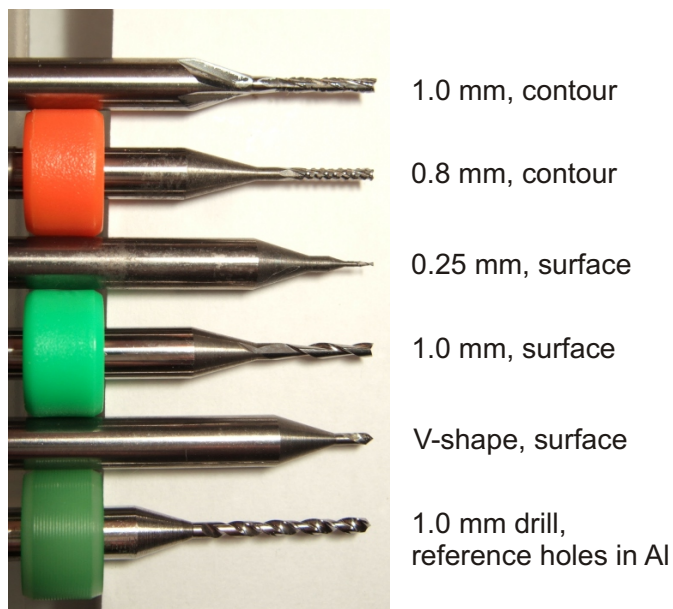
Fig. A.1: *Different milling tool blades for surface milling and cut out of the PCBs.*

Fig. A.1 and Tab. A.1 shortly describe the tools and the tooling parameters used for different functions for the manufacturing of test circuits and the final QM/FM boards. The milling parameters are adapted to the material properties in order to achieve a smooth cut or a smooth surface without burrs.

function	tool	$f_{ROT}[rpm]$	milling speed [mm/s]
contour cutting, RT/Duroid6002	contour cutter 0.8 mm	48000	3
contour cutting, TMM10	contour cutter 1.0 mm	42000	4
surface milling, isolate fine structures	90° V-shaped blade milling tool, var. trace width	50000	5
surface milling, isolate fine structures	surface milling tool 0.25 mm	50000	5
surface milling, rubout large areas	surface milling tool 1.0 mm	45000	4

Tab. A.1: *The milling parameters for different milling tools used for the fabrication of the IF boards.*
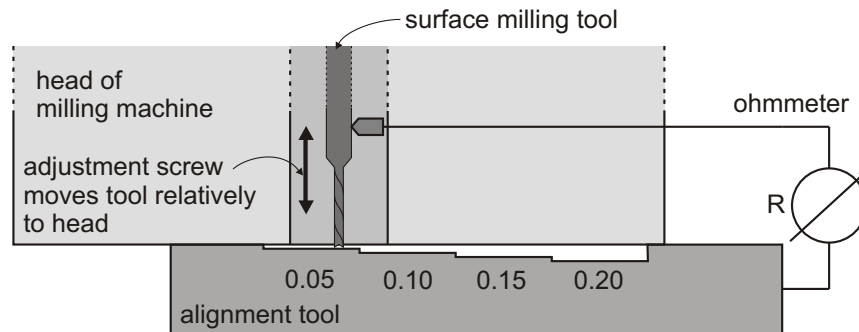
Fig. A.2: *Milling tool adjustment. The electric contact is used to determine the position where the surface milling tool touches the alignment tool. (Accuracy $\approx 10\,\mu m$)*

A.2 Adjustment of surface milling tools

The best way to obtain an even and small engraving depth was not to mill with a constant z-position of the machine head, but rather work with a head directly sliding over the substrate surface. By the small pressure of the pneumatically actuated head, the substrate is locally pushed down and the head always moves directly over the substrate surface. The only critical task left is the adjustment of the milling tool relative to the head base surface. This adjustment can be achieved with a small tool, which is explained in Fig. A.2. With this tool, a milling tool adjustment accuracy of $10\,\mu m$ can easily be obtained because the electrical contact between the milling tool and the adjustment tool is very sensitive.

A.3   Cutting procedure for the QM and FM boards

The following method was chosen to achieve both a good alignment and an entire cut out without the use of ligaments:

The substrate was first glued to a 2 mm epoxy carrier substrate with wax. The carrier substrate was heated up to the melting point of the wax ($T <$ $100°C$) and the substrate was then uniformly pressed to the carrier. In the workshop, 1 mm holes were drilled through both substrate layers at the drill mark locations. A microscope was used to achieve good alignment between drill marks and holes.

The Protomat C100/HF machine was prepared by covering the working area with an Aluminum board, which was aligned to the machine by dowel pins. 1 mm holes were drilled with the milling machine at positions corresponding to the drill marks on the substrate. Dowel pins were put in the holes and the substrate sandwich was placed on the Aluminum board. Usually three pins were used to align the substrate with the aluminum board and, thus, the milling machine. This slight over-determination was used to control the accuracy of the alignment.

Once the substrate sandwich was aligned with the machine, the machine head was adjusted to avoid conflicts with the pins slightly sticking out of the substrate. The cutting tool was adjusted to cut through the circuit substrate, only slightly touching the carrier substrate. Thus, the circuit board was fixed over the carrier during the entire process. The milling path was modified to begin and end not in the vicinity of the board outline. This avoids small cracks, which may occur when the cutting tool first penetrates the substrate from above (See Fig. 3.3).

After the cut out, the board is removed from the carrier substrate and cleaned from the remaining wax with Trichloroethylene. The residual roughness of the edges and small burrs of the copper ground (bottom) layer can be inspected under the microscope and have to be removed with fine sandpaper. After a second intensive clean, the boards are ready for assembly into the bias-T box.

List of Acronyms

2SB	**2 S**ide**B**and, sideband separating (mixer operation mode)
AGN	**A**ctive **G**alactic **N**ucleus
AGOR	**A**ccelerator **G**roningen **OR**say (superconducting cyclotron)
AWG	**A**merican **W**ire **G**auge (measure for wire diameter)
AWR MWO	**A**pplied **W**ave **R**esearch, **M**icro**W**ave **O**ffice
BA	**B**alanced **A**mplifier
CAD	**C**omputer **A**ided **D**esign
CAM	**C**omputer **A**ided **M**achining
CNC	**C**omputer **N**umerical **C**ontrol (computer aided machining)
COBE	**CO**smic **B**ackground **E**xplorer
CREME96	**C**osmic **R**ay **E**ffects on **M**icro**E**lectronics 1996
CST MWS	**C**omputer **S**imulation **T**echnology, **M**icro**W**ave **S**tudio
CTE	**C**oefficient of **T**hermal **E**xpansion
CTF	**C**omputer **T**o **F**ilm (mask generation technique)
CVV	**C**ryostat **V**acuum **V**essel (Herschel cryostat)
CW	**C**ontinues **W**ave
DM	**D**emonstration **M**odel
DSB	**D**ouble **S**ide**B**and (mixer operation mode)
DUT	**D**evice **U**nder **T**est
dxf	**D**rawing e**X**change **F**ormat (CAD file format)
ECSS	**E**uropean **C**oorperation on **S**pace **S**tandardization
EMC	**E**lectro**M**agnetic **C**onformance
EMI	**E**lectro**M**agnetic **I**nterference
ESA	**E**uropean **S**pace **A**gency
ESD	**E**lectro**S**tatic **D**ischarge
ESP	**E**mission of **S**olar **P**rotons (radiation model)
ESTEC	**E**uropean **S**pace **R**esearch and **T**echnology **C**enter
FIRST	**F**ar **I**nfra**R**ed **S**pace **T**elescope
FDTD	**F**inite **D**ifference **T**ime **D**omain
FIR	**F**ar **I**nfra**R**ed
FIT	**F**inite **I**ntegration **T**echnique
FM	**F**light **M**odel
FPU	**F**ocal **P**lane **U**nit (part of the HIFI instrument)
FS	**F**light **S**pare Model
FWHM	**F**ull **W**idth at **H**alf **M**aximum

GCR	**G**alactic **C**osmic **R**ays
GPIB	**G**eneral **P**urpose **I**ndustrial **B**us
HBM	**H**uman **B**ody **M**odel
HEB	**H**ot **E**lectron **B**olometer
HEMT	**H**igh **E**lectron **M**obility **T**ransistor
HIFI	**H**eterodyne **I**nstrument for the **F**ar **I**nfrared
HRS	**H**igh **R**esolution **S**pectrometer
IF	**I**ntermediate **F**requency
ISM	**I**nter **S**tellar **M**edium
JFET	**J**unction **F**ield **E**ffect **T**ransistor
JPL-91	**J**et **P**ropulsion **L**aboratories (radiation model from JPL in 1991)
KOSMA	**K**ölner **O**bservatorium für **S**ub-**m**m **A**stronomie
KVI	**K**ernfysisch **V**ersneller **I**nstituut (in Groningen, NL)
lmd	LPKF file format
LNA	**L**ow **N**oise **A**mplifier
LO	**L**ocal **O**scillator
LSB	**L**ower **S**ide**B**and
MGE	**M**axwell **G**rid **E**quations
MSA	**M**ixer **S**ub **A**ssembly (part of the FPU)
MU	**M**ixer **U**nit
NASA	**NA**tional **S**pace **A**gency
NGST	**N**ext **G**eneration **S**pace **T**elescope
NLR	**N**ationaal **L**ucht- en **R**uimtevaartlaboratorium
NTD	**N**eutron **T**ransmutation **D**oped
PACS	**P**hotodetector **A**rray **C**amera and **S**pectrometer
PAH	**P**olycyclic **A**romatic **H**ydrocarbon
PBA	**P**erfect **B**oundary **A**pproximation (propietary technology of CST)
PCB	**P**rinted **C**ircuit **B**oard
pdf	**P**ortable **D**ocument **F**ormat
PDR	**P**hoton-**D**ominated **R**egion
PEC	**P**erfectly **E**lectrically **C**onducting
PWV	**P**recipitable **W**ater **V**apor
QM	**Q**uality **M**odel
rad	**r**adiation **a**bsorbed **d**ose ($1\,rad = 0.01\,J/kg$)
RF	**R**adio **F**requency (=high frequency)
SIS	**S**uperconductor **I**nsulator **S**uperconductor tunnel junction
SMA	**S**ub **M**iniature version **A** connector
SPENVIS	**S**pace **E**nvironment **I**nformation **S**ystem
SPICE	**S**imulation **P**rogram with **I**ntegrated **C**ircuits **E**mphasis
SPIRE	**S**pectral and **P**hotometric **I**maging **RE**ceiver
SRON	**S**tichting voor **R**uimte**O**nderzoek **N**ederland
SSB	**S**ingle **S**ide**B**and (mixer operation mode)
TEM	**T**ransversal **E**lectro**M**agnetic
USB	**U**pper **S**ide**B**and
WBS	**W**ide **B**and **S**pectrometer
YIG	**Y**ttrium **I**ron **G**arnet (ferrimagnetic material for tunable filters)

Bibliography

[1] APEX web team (apex@apex telescope.org). Atacama Pathfinder EXperiment, APEX, Chajnantor atmospheric transmission. website: http://www.apex-telescope.org/scripts/transpwv/, Feb. 2006.

[2] Measurement of PWV and Saturation-point PWV (website). Technical report, Harvard-Smithsonian Center for Astrophysics, 60 Garden Street, Cambridge, MA 02138, USA, Nov. 1999.

[3] G. L. Pilbratt. The Herschel Mission, Scientific Objectives and This Meeting. In *Proc. Symp. The Promise of the Herschel Space Observatory*, pages 13–20, 2000.

[4] A. Poglitsch, C. Waelkens, and N. Geis. The Photodetector Array Camera & Spectrometer (PACS) for Herschel. In *Proc. Symp. The Promise of the Herschel Space Observatory*, 2001.

[5] M.J. Griffin, B.M. Swinyard, and L. Vigroux. The SPIRE instrument for Herschel. In *Proc. Symp. The Promise of the Herschel Space Observatory*, 2001.

[6] T. de Graauw and F.P. Helmich. Herschel-HIFI: The Heterodyne Instrument for the Far-Infrared. In *Proc. Symp. The Promise of the Herschel Space Observatory*, 2001.

[7] E. van Dishoeck. Molecular Line Surveys of Star-Forming Regions with Herschel (FIRST). In *Proc. Symp. The Promise of the Herschel Space Observatory*, 2001.

[8] A.G. Tielens, F.P. Helmich, and N. Whyborn. Science User Requirements Document. Technical Report SRON-G/HIFI/SP/2000-001, SRON, June 2000.

[9] S. Glenz, M. Justen, P. Pütz, R. Teipen, T. Tils, C.E. Honingh, and K. Jacobs. Broadband NbTiN based SIS mixers for HIFI band 2. In *Digest 27th Int. Conf. on Infrared and Millimeter Waves*, pages 257–258. IEEE, September 2002.

[10] M. Justen, T. Tils, S. Glenz, P. Pütz, M. Schultz, R. Teipen, C.E. Honingh, and K. Jacobs. Broadband NbTiN based SIS mixer for band 2 of the HIFI instrument for the Herschel spacecraft. In *Proc. of the 6th European Conference on Applied Superconductivity*, pages 2994–3001. Institute of Physics Publishing, 2003.

[11] M. Justen, M. Schultz, T. Tils, R. Teipen, S. Glenz, P. Pütz, C. E. Honingh, and K. Jacobs. SIS flight mixers for band 2 of the HIFI instrument of the herschel space telescope. In M. Thumm and W. Wiesbeck, editors, *Digest 29th Int. Conf. on Infrared and Millimeter Waves and 12th Int. Conf. on Terahertz Electronics*, pages 437–438, September 2004.

[12] T. Tils. *Design and 3-D Electromagnetic Modeling of Terahertz Waveguide Mixers and Components.* Dissertation (phd thesis), KOSMA, 1. Physikalisches Institut der Universität zu Köln, Zülpicher Str. 77, 50937 Köln, Germany, May 2005.

[13] R. Teipen. *Design and Analysis of a Broadband SIS-Mixer for the Heterodyne Instrument for the Far Infrared (HIFI) on the Herschel Space Observatory.* Phd thesis, 1. Physikalisches Institut der Universität zu Köln, Zülpicher Str. 77, 50937 Köln, Germany, Nov. 2006.

[14] Stefan Glenz. *Fabrication and Characterization of $Nb - Al/Al_2O_3 - Nb$ Superconductor-Insulator-Superconductor Devices with NbTiN Based Tuning Circuits for the Herschel Space Observatory.* PhD thesis, KOSMA, 1. Physikalisches Institut der Universität zu Köln, 2005.

[15] P.R. Jewell and J.G. Magnum. System Temperatures, Single Versus Double Sideband Operation, and Optimum Receiver Performance. MMA Memo 170, NRAO, May 1997.

[16] Brian Jackson and Jaap Evers. Environmental Test Levels for the HIFI Mixers. Technical Report FPSS-00276, SRON, RUG, Groningen, The Netherlands, Aug. 2003.

[17] N. D. Whyborn. SIS Mixer Bias Stability and Noise Requirements. Technical Report SRON-G/FCU/TN/2000-003, SRON, July 2000.

[18] Inc. Applied Wave Research. *Microwave Office User Guide.* 1960 E. Grand Avenue, Suite 430, El Segundo, CA 90245, USA, 2002. http://web.appwave.com/.

[19] V. Litovski and M. Zwolinski. *VLSI Circuit Simulation and Optimization.* Kluwer Academic Publishers, 1997.

[20] F.Giannini, R.Ruggieri, and J.Vrba. Shunt-connected microstrip radial stubs. *IEEE Transactions on Microwave Theory and Techniques*, 34:363–366, March 1986.

[21] S.L. March. Analyzing lossy radial-line stubs. *IEEE Transactions on Microwave Theory and Techniques*, 33:269–271, March 1985.

[22] B.C.Wadell. *Transmission Line Design Book*, pages 306–307. Artech House, Boston-London, 1991.

[23] T. Weiland. A discretization method for the solution of Maxwell's equations for six-component fields. *Electronics and Communications (AEU)*, 31(3):116–120, 1977.

[24] M. Clemens and T. Weiland. Discrete Electromagnetism with the Finite Integration Technique. *Progress In Electromagnetics Research*, 32:65–87, 2001.

[25] R. Schuhmann and T. Weiland. Conservation of discrete energy and related laws in the finite integration technique. *Progress In Electromagnetics Research*, 32:301–316, 2001.

[26] P. Thomas and T.Weiland. Numerical Stability of Finite Difference Time Domain Methods. *IEEE Transaction on Magnetics*, 34(5):2740–2743, May 1998.

[27] B. Krietenstein, R. Schuhmann, P. Thomas, and T. Weiland. The Perfect Boundary Approximation Technique Facing the Big Challenge of High Precision Field Computation. *LINAC98 Papers*, (TH4041), 1998.

[28] K. Kurokawa. Power Waves and the Scattering Matrix. *IEEE Transactions on Microwave Theory and Techniques*, 13(2):194– 202, March 1965. ISSN: 0018-9480.

[29] H.G. LeDuc, A. Judas, S.R. Cypher, B. Bumble, B.D. Hunt, and J.A. Stern. Submicron area NbN/MgO/NbN tunnel junctions for SIS mixer-applications. *IEEE Transactions on Magnetics*, 27(2):3192–3195, 1991.

[30] Rogers Corporation, Microwave Materials Division, 100 S. Roosevelt Avenue, Chandler, AZ 85226, USA. *TMM Temperature Stable Microwave Composite Circuit Board Materials*.

[31] Huber+Suhner AG, Interconnection division, CH-9100 Herisau, Switzerland. *Suhner Microwave cable datasheet type EZ 86-CU-TP/M17 (semi rigid, the form stable microwave cable)*, June 2002.

[32] K.C. Gupta, R. Gang, I. Bahl, and P. Bhartia. *Microstrip Lines and Slotlines*, chapter 3.4.5, pages 196–200. Artech House, 2nd edition, 1996.

[33] C. Diez, J.D. Gallego, I. López, and R. García. Electrical Characterisation of SMA Connectors for Cryogenic Amplifiers. Technical Report 6, Centro Astronómico de Yebes, Obs. Astronómico Nacional, Apdo 148, 19080 Guadalajara, Spain, Nov. 2000.

[34] American Technical Ceramics. ATC TechSelect. website. www.atceramics.com.

[35] K. Jacobs and G. Larson. Mixer Band 2 ESD Testing. Technical report, KOSMA, Zülpicher Str. 77, 50937 Köln, Germany, Sept. 2002.

[36] Electrostatic Discharge Assosiation. *ESDS Component Sensitivity Classification - Human Body Model*, volume ESD STM5.1. 1998.

[37] LPKF Laser & Electronics AG, Osteriede 7, D-30827 Garbsen, Germany. *LPKF ProtoMat C-series*.

[38] Emerson & Cuming, 46 Manning Road, Billerica, MA 01821, USA. *ABLEFILM 5025E, Electrically And Thermally Conductive Adhesive Film*, 2000.

[39] M. Justen. *H_P_BD_6, Preparation and Soldering of the SMA Plug, the Cu flange and the filament to the Semi Rigid SMA Cable for HIFI mixer band 2*. KOSMA, Zülpicher Str. 77, 50937 Köln, Germany, Aug. 2003.

[40] ESA/ECSS, ECSS Secretariat, ESA-ESTEC, Requirements & Standards Division, Noordwijk, The Netherlands. *Q-70-18A, Preparation, assembly and mounting of RF coaxial cables*, Aug. 2001.

[41] ESA/ECSS, ECSS Secretariat, ESA-ESTEC, Requirements & Standards Division, Noordwijk, The Netherlands. *Q-70-08A, Manual soldering of high-reliability electrical connections*, Aug. 1999. formerly PSS-01-708, Issue 1, March 1985.

[42] Epoxy Technology, Inc., 14 Fortune Drive, Billerica, MA 01821-3972, USA. *Epotek H20E, Electrically Conductive, Silver Epoxy, Datasheet, Rev. IV*, Oct. 2000.

[43] J.D. Gallego, I.L. Fernández, and C.D. González. *Measurement of Cryogenic Performance of 4-8 GHz Pamtech Isolators S/N 108-112*. Centro Astronómico de Yebes (CAY), Obs. Astronómico Nacional, Apdo 148, 19080 Guadalajara, Spain, May 2000.

[44] I.L. Fernández. *YCF 6012 1001 DM Amplifier Report*. Centro Astronómico de Yebes (CAY), Obs. Astronómico Nacional, Apdo 148, 19080 Guadalajara, Spain, May 2002.

[45] P.R. Wesselius, K.J. Wildeman, and R. de Lange. HIFI and its Focal Plane Subsystem. Technical report, SRON, Nov. 2000.

[46] N. Wadefalk, A. Mellberg, I. Angelov, M.E. Barsky, S. Bui, E. Choumas, R.W. Grundbacher, E.L. Kollberg, R. Lai, N. Rorsman, P. Starski, J. Stenarson, D.C. Streit, and H. Zirath. Cryogenic wide-band ultra-low-noise

IF amplifiers operating at ultra-low DC power. *IEEE Transactions on Microwave Theory and Techniques*, 51(6):1705–1711, June 2003. ISSN: 0018-9480.

[47] J.R. Tucker and M.J. Feldman. Quantum detection at millimeter wavelenghts. *Rev. Mod. Phys.*, 57(4):1055–1113, 1985.

[48] L. Callegaro. Unified derivation of Johnson and shot noise expressions. *Am. J. Phys.*, 74(5):438–439, May 2006.

[49] A.R. Kerr, M.J. Feldman, and S.K. Pan. Receiver Noise Temperature, the Quantum Noise Limit, and the Role of the Zero-Point Fluctuations. *MMA Memo*, (161), Sept. 1996.

[50] N.D. Whyborn. Report on HIFI EMC Status. Technical Report SRON-G/HIFI/RP/2001-001, SRON, 2001.

[51] B.J. van Leeuwen. Radiated E-field susceptibility of various FPU components. Technical Report SRON-U/FPU/RP/2002-001, SRON, NLR, Feb. 2002.

[52] M. Justen. EMC Test Evaluation for HIFI Mixer Band 2. Technical report, KOSMA, May 2003.

[53] Arianespace. Ariane 5 User's Manual, Issue 4, Revision 0. Technical report, Arianespace, Nov. 2004.

[54] M. Dikpati, G. de Toma, and P.A. Gilman. Predicting the strength of solar cycle 24 using a flux-transport dynamo-based tool. *Geophysical Research Letters*, 33(5):5102–5106, March 2006.

[55] H. Evans. FIRST L-2 Radiation Environment. Technical Report esa/estec/wma/he/FIRST/3, ESA/ESTEC (European Space and Technology Centre), March 1997.

[56] N. Reau. Radiation Shielding Analysis of Herschel and Planck Satellites. Technical Report H-P-1-ASPI-AN-0321, Alcatel Space, Cannes, France, June 2002.

[57] A.J. Tylka, J.H.J. Adams, P.R. Boberg, B. Brownstein, W.F. Dietrich, E.O. Flueckiger, E.L. Peterson, M.A. Shea, D.F. Smart, and E.C. Smith. CREME 96: A revision of the Cosmic Ray Effects on Micro-Electronics code. *IEEE Transactions on Nuclear Science*, 44:2150–2160, 1997.

[58] J. Feynman, G. Spitale, J. Wang, and S. Gabriel. Interplanetary Proton Fluence Model: JPL 1991. *J. Geophys. Res.*, 98(13), 1993.

[59] M.A. Xapsos, J.L. Barth, E.G. Stassinopoulos, E.A. Burke, and G.B. Gee. Space Environment Effects: Model for Emission of Solar Protons (ESP)ŮCumulative and Worst-Case Event Fluences. Technical Report

NASA/TP-1999-209763, Naval Research Laboratory, NASA, Washington, DC, USA, Dec. 1999.

[60] SPENVIS. *Help Page of SPENVIS.* ESA/ESTEC SPENVIS. www.spenvis.oma.be/spenvis/help/background/background.html.

[61] J.L. Barth, J.C. Isaacs, and C. Poivey. The Radiation Environment for the Next Generation Space Telescope. Technical report, NASA/Goddard Space Flight Center, Greenbelt, Maryland, USA, Sept. 2000.

[62] S.M. Seltzer. Updated calculations for routine space-shielding radiation dose estimates: SHIELDOSE-2. Technical Report NIST Publication NISTIR 5477, NIST, Gaithersburg, Maryland, USA, Dec. 1994.

[63] S.E. King, R. Magno, and W.G. Maisch. Radiation damage assessment of Nb tunnel junction devices. *IEEE Transactions on Nuclear Science*, 38(6):1359–1364, Dec. 1991.

[64] S. Pagano, R. Cristiano, L. Frunzio, V.G. Palmieri, G. Pepe, R. Gerbaldo, G. Ghigo, L. Gozzelino, E. Mezzetti, and R. Cherubini. Effect of intense proton irradiation on properties of josephson devices. *IEEE Transactions on Applied Superconductivity*, 7(2):2917 − 2920, June 1997.

[65] M.A. Cutter. Technical Note on Radiation Effects Analysis Methods. Technical Report Sira Reference: 245.TN.2/1, ESA ESTEC and Sira Electro-Optics Ltd., Chislehurst, Kent, BR7 5EH, England, April 2002.

[66] J.F. Ziegler. The Stopping of Energetic Light Ions in Elemental Matter. *J. Appl. Phys. / Rev. Appl. Phys.*, 85:1249–1272, 1999.

[67] C. Claeys and E. Simoen. Study of Radiation Effects in Cryogenic Electronics and Advanced Semiconductor Materials. Technical Report P35284-IM-RP-0023, Work Order 1938/96/NL/LB, ESTEC, Interuniversity Microelectronics Center (IMEC), Aug. 2000.

[68] R. Bieber, M. Justen, C.E. Honingh, S. Glenz, A.M. van den Berg, P. van Luik, H. Kiewit, and M. Schippers. Proton irradiation of superconducting-insulator superconducting (SIS)-detectors for space application. In *Proc. of 7th European Conference on Radiation and its Effects on Components and Systems (RADECS 2003)*, pages 55–57, 2003.

[69] A. R. Kerr, M. J. Feldman, and S.-K. Pan. Receiver noise temperature, the quantum noise limit, and the role of the zero-point fluctuations. In *Proc. Eighth Int. Symp. on Space Terahertz Technology*, pages 101–111, Boston, MA, March 1997. Harvard University.

[70] Radionetwiki. website. http://www.radionet-eu.org/rnwiki/.

[71] A.R. Kerr. On the Noise Properties of Balanced Amplifiers. MMA Memo 227, NRAO, Sept. 1998.

[72] G. Gonzalez. *Microwave Transistor Amplifiers, Analysis and Design*. Prentice-Hall Inc., 1984.

[73] C.B. Sharpe. An Equivalence Principle for Nonuniform Transmission-Line Directional Couplers. *IEEE Transactions on Microwave Theory and Techniques*, 15:398–405, July 1967.

[74] R.W. Klopfenstein. A Transmission Line Taper of Improved Design. *Proc. IRE, (London)*, 44(1):31–35, Jan. 1956.

[75] D. Youla. Analysis and Synthesis of Arbitrarily Terminated Lossless Nonuniform Lines. *IEEE Transactions on Circuits and Systems*, 11(1):363Ű371, Sept. 1964. ISSN: 0098-4094.

[76] A. Bergquist. Wave Propagation on Nonuniform Transmission Lines. *IEEE Transactions on Microwave Theory and Techniques*, 20(1):557–558, Aug. 1972.

[77] M.B. Bazdar, A.R. Djordjevic, R.F. Harrington, and T.K. Sarkar. Evaluation of Quasi-Static Matrix Parameters for Multiconductor Transmission Lines Using Galerkin's Method. *IEEE Transactions on Microwave Theory and Techniques*, 42:1223–1228, July 1994.

[78] M. Kirsching and R.H. Jansen. Accurate Wide-Range Design Equations for the Frequency-Depent Characteristic of Parallel Coupled Microstrip Lines. *IEEE Transactions on Microwave Theory and Techniques*, 32(1):83–90, Jan. 1984.

[79] CST GmbH. *CST Microwave Studio, Online Help*. Darmstadt, Germany, www.cst.com.

[80] Maplesoft, a division of Waterloo Maple Inc. *Maple 9.5, Online Help*. Ontario, Canada. www.maplesoft.com.

[81] C.P. Tresselt. Design and Computed Theoretical Performance of Three Classes of Equal-Ripple Nonuniform Line Couplers. *IEEE Transactions on Microwave Theory and Techniques*, 17(4):218–230, April 1969.

[82] E.G. Cristal and L. Young. Theory and Tables of Optimum Symmetrical TEM-Mode Coupled-Transmission-Line Directional Couplers. *IEEE Transactions on Microwave Theory and Techniques*, 13(1):544–558, Sept. 1965. ISSN: 0018-9480.

[83] F.J. Harris. On the Use of Windows for Harmonic Analysis with the Discrete Fourier Transform. *Proceedings of the IEEE*, 66(1):51–84, Jan. 1978.

Teilpublikationen

[1] M. Justen, M. Schultz, T. Tils, R. Teipen, S. Glenz, P. Pütz, C. E. Hon-ingh and K. Jacobs. SIS Flight Mixers for Band 2 of the HIFI Instrument of the Herschel Space Telescope. In *Digest 29th Int. Conf. on Infrared and Millimeter Waves and 12th Int. Conf. on Terahertz Electronics*, pages 437-438, 2004.

[2] R. Bieber, M. Justen, C.E. Honingh, S. Glenz, A.M. van den Berg, P. van Luik, H. Kiewit and M. Schippers. Proton irradiation of superconducting-insulator superconducting (SIS)-detectors for space application. In *Proc. of 7th European Conference on Radiation and its Effects on Components and Systems (RADECS 2003)*, pages 55-57, 2003.

[3] M. Justen, T. Tils, S. Glenz, P. Pütz, M. Schultz, R. Teipen, C.E. Hon-ingh and K. Jacobs. Broadband NbTiN Based SIS Mixer for Band 2 of the HIFI Instrument for the Herschel Spacecraft. In *Proc. of the 6th European Conference on Applied Superconductivity.*, pages 2994-3001, 2003.

[4] R. Teipen, M. Justen, T. Tils, S. Glenz, C. E. Honingh, K. Jacobs, B. D. Jackson, T. Zijlstra and M. Kroug. Influence of Junction-Qualtity and Current Density on HIFI Band 2 Mixer Performance. In *Proc. 14th Int. Symp. on Space Terahertz Technology*, pages 55-62, 2003.

[5] S. Glenz, M. Justen, P. Pütz, R. Teipen, T. Tils, C.E. Honingh and K. Jacobs. Broadband NbTiN based SIS Mixers for HIFI Band 2. In *Digest 27th Int. Conf. on Infrared and Millimeter Waves*, pages 257-258, 2002.

Danksagung

Acknowledgment

Förderung

Erklärung

Ich versichere, dass ich die von mir vorgelegte Dissertation selbständig angefertigt, die benutzten Quellen und Hilfsmittel vollständig angegeben und die Stellen der Arbeit – einschließlich Tabellen, Karten und Abbildungen –, die anderen Werken im Wortlaut oder dem Sinn nach entnommen sind, in jedem Einzelfall als Entlehnung kenntlich gemacht habe; dass diese Dissertation noch keiner anderen Fakultät oder Universität zur Prüfung vorgelegen hat; dass sie – abgesehen von unten angegebenen Teilpublikationen – noch nicht veröffentlicht worden ist sowie, dass ich eine solche Veröffentlichung vor Abschluss des Promotionsverfahrens nicht vornehmen werde. Die Bestimmungen dieser Promotionsordnung sind mir bekannt. Die von mir vorgelegte Dissertation ist von Prof. Dr. J. Stutzki betreut worden.

Kurzfassung

Diese Arbeit beschreibt die Entwicklung und die Fertigung von ZF-Schaltkreisen für zwei verschiedene Heterodynempfänger für sub-mm Radio-astronomie.

Das erste Projekt befasst sich mit den ZF-Schaltkreisen für die SIS-Mischer für Band 2 des "Heterodyne Instrument for the Far Infrared"(HIFI) für das Herschel Satellitenobservatorium der ESA. Diese hochempfindlichen Mischer mit einem kompakten, modularen Design wurden hier bei KOSMA entworfen und gefertigt.

Der ZF-Signalweg in diesen Mischern besteht aus dem Mischerblock (mit dem SIS-Mischelement) und einem Bias-T, welches für die Einspeisung einer Biasspannung und die Separierung des ZF-Signals notwendig ist.

In einer detaillierten Untersuchung der ZF-Eigenschaften des Mischerblocks wurden die geometrischen Kapazitäten des SIS-Kontaktes und der Tuning-Struktur sowie die Induktivität der Bonddrähte gesondert charakterisiert und dann insgesamt bewertet. Die hier dokumentierten Berechnungen zeigen, dass diese Mischerblöcke bis zu einer ZF von 12 GHz verwendet werden können.

Das Bias-T für HIFI ist eine Neuentwicklung mit exzellenten Eigenschaften und hoher Ausfallsicherheit, die den speziellen Anforderungen eines satelli-tengestützten Instruments entsprechen. Die härtesten Anforderungen an eine zuverlässige Funktion stellen die starken Vibrationen während des Starts und wiederholte Temperaturwechsel zu kryogenen Temperaturen (cryogenic thermal cycling) während der Mischertests und der Instrumenttests dar.

Eine sehr verlustarme ZF-Signalübertragung ($S_{21} > -0.25\,dB$) konnte mit speziellen, sehr zuverlässigen Verbindungen im Signalweg erreicht werden. Unterschiede in den thermischen Ausdehnungskoeffizienten wurden dabei durch eine mechanisch flexible Bauweise ausgeglichen. Diese speziellen Verbindungs-teile wurden im Rahmen dieser Arbeit entwickelt, gefertigt und nach dem Einbau in die Mischer ausgiebig getestet.

Neben der verlustarmen ZF-Signalübertragung gewährleisten die im Bias-T eingebauten Filter einen guten Schutz vor elektromagnetischen Störungen, die über die ungeschirmten Versorgungsleitungen eindringen können.

Nach erfolgreichen Qualitäts- und Zuverlässigkeitstests werden die Mischer zur Zeit in das HIFI-Instrument eingebaut.

Das zweite Projekt im Rahmen dieser Arbeit ist die Entwicklung und Fertigung von extrem breitbandigen Richtkopplern, die als -3 dB 90°-Hybride auf der ZF-Seite von Seitenband-Separierenden Mischern mit großer ZF-Bandbreite benutzt werden können.

Durch einen stetigen Verlauf der even- und odd-Mode Impedanzen können unkontrollierte Reflexionen der elektrischen Wellen verhindert werden. Durch Verwendung von Striplines in einem homogenen Dielektrikum, die über ihre breite Seite elektrisch gekoppelt werden, ist es möglich, hohe Kopplungskoeffizienten zu erreichen. Durch die Homogenität des Mediums kann sich eine TEM-Mode ausbilden, die zusammen mit dem stetigen Impedanzverlauf Voraussetzung für eine hohe Bandbreite ist. Der Impedanzverlauf kann über die Fourier-Transformation des Kopplungsbandes ($S_{21}(\omega)$) berechnet werden.

Um die tatsächliche Geometrie (d.h. Breite und Abstand der Striplines) aus dem Impedanzverlauf bestimmen zu können, wurde ein Interpolationsverfahren entwickelt, das Resultate eines kommerziellen 2D EM Simulationsprogramms verwendet. Dieses Verfahren wurde erfolgreich angewendet, um verschiedene Koppler zu entwerfen, die hergestellt und getestet wurden. Durch Einführung von Mode-Launchern an den Übergängen von Koaxialleitung zu Stripline konnte die TEM-Moden Qualität verbessert werden, und die Bandbreite der Koppler auf 1.9–9.3 GHz erhöht werden.

Lebenslauf

Matthias Justen

Geburtsdatum:	22. Nov. 1973
Geburtsort:	Trier
Familienstand:	ledig
Staatsangehörigkeit:	deutsch

Schulausbildung

1980 – 1984	Grund- und Hauptschule Waldrach
1984 – 1993	Hindenburg Gymnasium Trier
Juni 1993	Zeugnis der allgemeinen Hochschulreife

Studium

1993 – 1996,	Physikstudium an der Universität Würzburg
1996 – 1997	Einjähriges Studium in Russland an der Staatl. Universität St. Petersburg (Санкт-Петербургский Государственный Университет) Forschungstätigkeit am Institut für Polymerphysik: *Feldabhängige Phasenübergänge in Flüssigkristallen Elektrooptischer Kerreffekt bei sehr hohen Feldstärken*
1997 – 2000	Fortsetzung des Studiums in Würzburg
Mai 2000	Abschluss der Diplomarbeit, Thema: *Konstruktion und Charakterisierung eines $\lambda/4$-Plättchens zur Erzeugung von zirkular polarisierter Röntgenstrahlung und magnetische USAXS zur Vermessung von Domänenstrukturen*
Juni 2000	Diplom in Physik

Promotion

2000 – 2006	Promotionsstudium am I. Physikalischen Institut der Universität zu Köln

Berufliche Tätigkeit

seit 2000	Wissenschaftlicher Mitarbeiter am I. Physikalischen Institut der Universität zu Köln